Chem Soc Rev

REVIEW ARTICLE

View Article Online
View Journal | View Issue

Cite this: *Chem. Soc. Rev.*, 2020, **49**, 5772

Molecular catalysis of CO_2 reduction: recent advances and perspectives in electrochemical and light-driven processes with selected Fe, Ni and Co aza macrocyclic and polypyridine complexes

E. Boutin, [a] L. Merakeb, [a] B. Ma, [a] B. Boudy, [a] M. Wang, [a] J. Bonin, [a] E. Anxolabéhère-Mallart [a] and M. Robert *[ab]

Earth-abundant Fe, Ni, and Co aza macrocyclic and polypyridine complexes have been thoroughly investigated for CO_2 electrochemical and visible-light-driven reduction. Since the first reports in the 1970s, an enormous body of work has been accumulated regarding the two-electron two-proton reduction of the gas, along with mechanistic and spectroscopic efforts to rationalize the reactivity and establish guidelines for structure–reactivity relationships. The ability to fine tune the ligand structure and the almost unlimited possibilities of designing new complexes have led to highly selective and efficient catalysts. Recent efforts toward developing hybrid systems upon combining molecular catalysts with conductive or semi-conductive materials have converged to high catalytic performances in water solutions, to the inclusion of these catalysts into CO_2 electrolyzers and photo-electrochemical devices, and to the discovery of catalytic pathways beyond two electrons. Combined with the continuous mechanistic efforts and new developments for *in situ* and *in operando* spectroscopic studies, molecular catalysis of CO_2 reduction remains a highly creative approach.

Received 9th March 2020

DOI: 10.1039/d0cs00218f

rsc.li/chem-soc-rev

Introduction

CO_2 may become the renewable feedstock for making fuels and commodity and pharmaceutical chemicals we need to sustain our societies. If we manage to solve the challenges in reaching this goal, we would achieve a circular economy based on the use of renewable energies and CO_2. This goal remains elusive even in the most developed countries, and chemistry is poised to play a central role in addressing the key scientific challenges. A primary task is to develop selective, fast and efficient reduction processes of CO_2 into valuable products, such as carbon monoxide (CO), formic acid (HCOOH), methanol (CH_3OH), methane (CH_4), ethanol (CH_3CH_2OH) and ethylene (C_2H_4), in a sustainable manner. Catalyst development is of key importance for this purpose, and various approaches, both by homogeneous and heterogeneous chemistry, are widely pursued. Achieving electrochemically or photochemically driven conversion of CO_2 remains a grand challenge, especially if one considers that only abundant materials should be used in view of future large scale applications. Among various advantages, the use of molecular catalysts such as defined transition metal–ligand complexes allows for fine-tuning the chelating abilities and the steric, electronic and electrostatic effects of the ligands, thus opening a wide door towards thorough mechanistic and spectroscopic studies. Notably, abundant transition metals such as iron, manganese, cobalt, copper or nickel with activity for CO_2 catalytic reduction were already investigated in the early 1970s, starting with phthalocyanines and porphyrins.[1] The revival of these studies in the last 15 years has led to an enormous body of work and stimulating new results, even if molecular catalysts able to go beyond the 2-electron 2-proton traditional reduction products (CO and formic acid) remain scarce. Aza macrocycle ligands such as porphyrins and phthalocyanines, as well as polypyridine ligands are extensively investigated and show good results both under electrochemical conditions and light stimulation with appropriate sensitizers and sacrificial electron donors. A number of comprehensive and high level reviews have been published over the years notably concerning the use of abundant, cheap metals under electrochemical conditions.[2–6] Less emphasis has been put on photochemically induced reduction of CO_2 but related approaches are developing fast. Why publishing another review

[a] *Université de Paris, Laboratoire d'Electrochimie Moléculaire, CNRS, F-75006 Paris, France. E-mail: robert@u-paris.fr*
[b] *Institut Universitaire de France (IUF), F-75005 Paris, France*

on the topic? Not only because the field is rapidly evolving, with more efficient and selective systems, but also because new perspectives are emerging, at the interfaces of homogeneous and heterogeneous catalysis, or of electrochemistry and photochemistry (molecular photoelectrodes, self-standing hybrid materials, *etc.*), as well as regarding mechanistic studies with *in situ* and *in operando* analytical methods. Moreover, the recent implementation of molecular catalysts into electrolyzers operating at large current densities (>150 mA cm^{-2}) has opened new possibilities for the design of real devices that may be able to reach the market. Finally, first examples of molecular catalysts able to produce highly reduced products such as methanol and methane have recently been launched, opening also stimulating perspectives toward new chemistry. We have chosen to focus on compounds including mainly Co, Fe, and Ni porphyrin, phthalocyanine and polypyridine complexes so as to illustrate, discuss and highlight the above-mentioned electrochemical and light-driven processes for carbon dioxide catalytic reduction. Regarding electrochemical approaches, we have further focused the scope on typical examples rather than on an exhaustive description. In some cases, mechanistic studies have helped in designing the most efficient catalysts on a rational basis, and such examples will be described in more detail. Regarding visible-light-driven catalytic processes, mechanistic and spectroscopic in-depth studies are less numerous and we have rather chosen to give a more comprehensive overview of the field.

1. Electrochemical approaches

1.1 Introduction to the electrochemical reduction of CO_2.

One-electron reduction of CO_2 to form the $CO_2^{\bullet-}$ radical anion requires a large negative potential due to solvent and internal reorganization ($E^0 = -1.90$ V *vs.* NHE in aqueous media).[3] Catalysis is necessary to overcome kinetic barriers and to efficiently and selectively reduce CO_2.[4] Multi-proton coupled electron transfers may afford various products as illustrated below for C_1 products (eqn (1)–(6)), where the $E^{0\prime}$s are the apparent (pH dependent) standard redox potentials *vs.* NHE at pH 7.

$$CO_2 + e^- \rightarrow CO_2^{\bullet-}, \quad E^{0\prime} = -1.90\ \text{V} \tag{1}$$

$$CO_2 + 2H^+ + 2e^- \rightarrow HCOOH, \quad E^{0\prime} = -0.61\ \text{V} \tag{2}$$

$$CO_2 + 2H^+ + 2e^- \rightarrow CO + H_2O, \quad E^{0\prime} = -0.53\ \text{V} \tag{3}$$

$$CO_2 + 4H^+ + 4e^- \rightarrow HCHO + H_2O, \quad E^{0\prime} = -0.48\ \text{V} \tag{4}$$

$$CO_2 + 6H^+ + 6e^- \rightarrow CH_3OH + H_2O, \quad E^{0\prime} = -0.38\ \text{V} \tag{5}$$

$$CO_2 + 8H^+ + 8e^- \rightarrow CH_4 + 2H_2O, \quad E^{0\prime} = -0.24\ \text{V} \tag{6}$$

Ideally a proper understanding of the reaction pathways may lead to rational catalyst optimization. This is probably a definitive advantage of the above-mentioned catalysts, which are well-defined single metal catalytic sites, for which the tools of electrochemistry and spectroscopy, including *in situ* and *in operando*, are well established.

Top row, from the left: Etienne Boutin, Lydia Merakeb, Bing Ma and Benjamin Boudy, Bottom row, from the left: Min Wang, Julien Bonin, Elodie Anxolabéhère-Mallart and Marc Robert

Etienne Boutin and Ming Wang obtained their PhD from Université de Paris in 2019 working on the heterogenization of molecular catalysts onto carbon materials for the CO_2RR and the electrochemical conversion of CO_2 into methanol, respectively. Benjamin Boudy and Bing Ma are currently working on the insertion of molecular CO_2 reduction catalysts into flow cell electrolyzers and the design of hybrid systems for light-driven reduction of CO_2 respectively, while Lydia Merakeb is developing new molecular catalysts for the electrochemical reduction of N_2. All three are expected to defend their PhD by the end of the year 2020. Julien Bonin received his PhD in Physical Chemistry from the Université Paris-Sud XI in 2005. He then joined the Radiation Laboratory at the University of Notre Dame as a Postdoctoral Research Associate. Since fall 2006, he has been an Associate Professor of Chemistry at the Université Paris Diderot, now Université de Paris. His current research interests are related to CO_2 reduction and photocatalysis.

Elodie Anxolabéhère-Mallart received her PhD in Molecular Electrochemistry from the Université Paris Diderot in 1991. In 1992 she was appointed CNRS researcher at the Université Paris-Sud, where she first got interested in artificial photosynthesis. She was a visiting researcher at Stanford University (1998–1999) and Lawrence Berkeley National Laboratory (1997–1999) to study both natural and model systems using X-ray Absorption Spectroscopy. In 2008 she joined the Laboratoire d'Electrochimie Moléculaire (LEM), focusing her research on O_2 and CO_2 activation using transition metal complexes.

Marc Robert obtained his PhD in 1995 from the Université Paris Diderot under the guidance of Jean-Michel Savéant and Claude Andrieux. Following a postdoctoral stay at Ohio State University with Matthew Platz, he started his academic career at the Université Paris Diderot in 1997. He is currently a Professor of Chemistry at the Université de Paris and a Senior fellow at the Institut Universitaire de France (IUF). His interests include electrochemical and photochemical approaches of electron transfer processes and catalytic activation of small molecules, mainly CO_2 and N_2.

In most cases, the initially inactive form of the catalyst P is reduced to a low-valent oxidation state metal by outer sphere electron transfer at an electrode.[7] In homogeneous catalysis, both substrate and catalyst are dissolved in the electrolyte solution and the chemical reactions take place within the reaction layer, a small fraction of the diffusion layer within which the concentration of the active catalyst Q is significant. Catalysis may be limited by diffusion of the substrate, concentration of the catalyst, of the substrate, of the product (inhibition) or by the intrinsic properties of the catalyst such as slow electron transfer kinetics or a chemical step of the catalytic process.[8] The metrics for assessing catalyst performances include the selectivity for the target reaction (in electrochemistry, faradaic efficiency FE is also used to measure the fraction of electrons used for the target reaction), the rate or turnover frequency (TOF, s^{-1}) which is defined by the mole amount of product formed divided by the mole amount of active catalysts per unit of time. The durability of the catalyst is measured through the turnover number (TON) given by the final mole amount of product once the catalysis has stopped because of the degradation of the catalytic system, divided by the initial mole amount of catalyst. Finally the overpotential, the thermodynamic cost for catalysis, is given by $\eta = E^0_{tr} - E$, where E is the applied potential and E^0_{tr} the apparent standard potential of the target reaction.

The intrinsic activity of a given catalyst may be represented by plotting the TOF as a function of the applied overpotential η (catalytic Tafel plot), as sketched in Fig. 1. The TOF is indeed dependent on η since the amount of active catalysts in the reaction layer increases when η increases, reaching a plateau value equal to k_{cat}, the pseudo-first-order rate constant of the limiting step of the catalytic process (provided the experimental conditions allow reaching the pure kinetic regime; see the next section for details).

Great care should be taken when estimating the TON (electrolysis experiment). In several publications, values are overestimated by orders of magnitude since authors use the mole amount of catalyst confined in the reaction layer, forgetting that the catalyst degrades over time and is progressively replaced by molecules from the bulk. As a consequence, the mole amount of product should be divided by the total mole amount of catalysts in the electrochemical reactor, once the reaction has ceased. This is the proper way to evaluate the turnover number.

Under supported conditions, the catalyst is immobilized at the electrode surface by various means, such as covalent linkage, non-covalent interactions such as electrostatic or π–π interactions or simply adsorption, or within periodic structures such as porous coordination polymers and metal–organic frameworks.[9–12] The reaction then takes place within the electrode surface. The major benefits of heterogeneous catalysts are the low amount of catalyst needed and, the possibility of by-passing diffusion limitations when using micro-fluidic cells or gas diffusion electrodes[13] and natural separation of catalyst and products (liquid or gaseous).

1.2 Mechanistic studies and spectroscopic tools

1.2.1 Cyclic voltammetry. Cyclic voltammetry (CV) can be used for mechanistic studies of systems in which electron transfer processes are coupled to chemical reactions. Advances in the studies of mechanisms, including catalytic multi-electron-multi-step ones, involved in homogeneous molecular catalysis of electrochemical reactions have been recently reviewed.[14]

Homogeneous catalysis. In the absence of catalyst, a substrate A can be reduced directly at the surface of an electrode upon applying a sufficiently negative potential (blue line in Fig. 2). When a catalyst P/Q is present in the medium, the reduced form Q of the catalyst reacts with the substrate A, giving B and thus regenerating the P form of the catalyst, which results in an increase of the recorded P-to-Q reduction current in cyclic voltammetry (red line in Fig. 2) and a loss in reversibility that is observed in the absence of substrate (green line in Fig. 2). In this case, transformation of A into B can be achieved at a more positive potential. The shape of the voltammogram depends on two dimensionless factors, the excess factor between substrate and catalyst concentration $\gamma = C^0_A/C^0_P$, and the kinetic parameter $(\lambda = (RT/F) \times kC^0_P/v)$ which accounts for the competition between

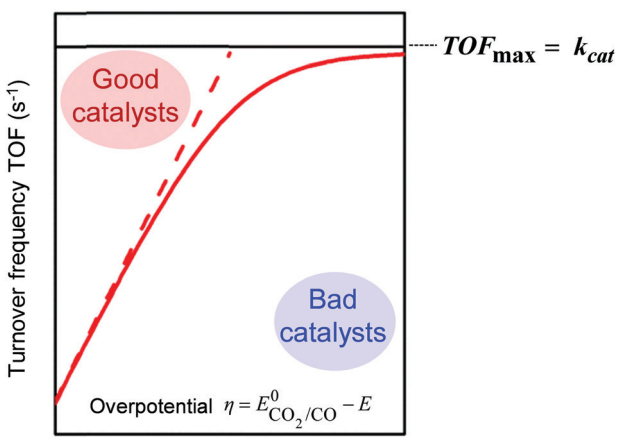

Fig. 1 Benchmarking of molecular catalyst intrinsic properties for the CO_2-to-CO reduction through the catalytic Tafel plot [TOF = $f(\eta)$].

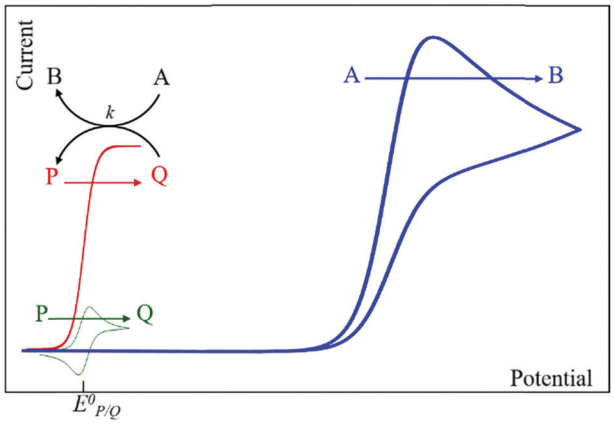

Fig. 2 Canonical cyclic voltammograms for the molecular catalysis of a one-electron catalytic electrochemical reaction (blue: direct reduction of A; green: reversible one-electron reduction of P in the absence of A; red: catalytic reduction of A triggered by the reduced form of the catalyst Q). Adapted from ref. 15 with permission from Wiley. Copyright 2006.

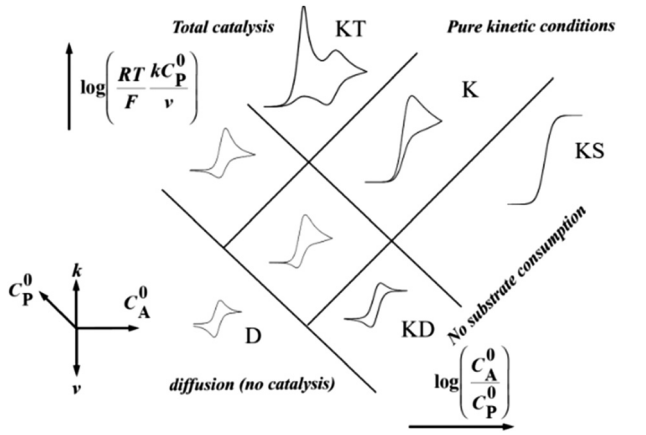

Fig. 3 Zone diagram for a one-electron catalytic reduction. Adapted from ref. 15 with permission from Wiley. Copyright 2006.

kinetics of the catalytic reaction (rate constant k) and the diffusion rates (scan rate v), as illustrated in the catalytic zone diagram (Fig. 3). Analysis applies in the case of fast electron transfer to the catalyst and selective catalytic reaction.

When the homogeneous catalytic reaction (rate constant k) is fast as compared to diffusion and concentration of the substrate is large enough to be constant (pure kinetic regime), a classical S-shaped CV is obtained as can be seen in the upper right part of Fig. 3. In this case, the rate constant k can be derived from the plateau current $i_{plateau}$, which is independent of scan rate v (eqn (7)):

$$i = \frac{i_{plateau}}{1+\exp\left[\frac{F}{RT}\left(E-E^0_{P/Q}\right)\right]} \quad \text{and} \quad i_{plateau} = FSC^0_P\sqrt{D_P}\sqrt{kC^0_A} \tag{7}$$

By dividing the current by the peak current i_0 obtained in the absence of a substrate (eqn (8)), the diffusion constant D_P and the electrode surface area S cancel (eqn (9)).

$$i_0 = 0.446FSC^0_P\sqrt{D_P}\sqrt{\frac{Fv}{RT}} \tag{8}$$

$$\frac{i}{i_0} = \frac{2.24\sqrt{kC^0_A}\sqrt{\frac{RT}{Fv}}}{1+\exp\left[\frac{F}{RT}\left(E-E^0_{P/Q}\right)\right]} \tag{9}$$

Special care should be taken when using these equations that are developed for the simple case of a one-electron reduction process. The number of exchanged electrons should be taken into account for more complex processes and different mechanisms will lead to different i/i_0 values.[16]

Since depletion of the substrate in the reaction layer may occur for fast reactions and low substrate concentrations (*e.g.* in the case of efficient catalysis for CO_2 reduction in water), the reduction current may be limited by substrate diffusion itself. Then the CV shape changes from a plateau one to a peak one (such as "total" catalysis (KT zone, Fig. 3) regime, obtained when the reaction layer is depleted from the substrate, while the remaining oxidized catalyst P is reduced at a more negative potential than the catalytic wave). Other phenomena can lead to a peak shaped CV, such as deactivation of the catalyst or inhibition by a product. In these latter cases, the above mentioned equations (7)–(9) do not apply anymore, but other strategies may be used in order to extract kinetic information from the voltammograms.

The first and most efficient strategy is to increase the scan rate (as long as the reaction rate allows it) so as to obtain the putative plateau-shaped CV. This strategy was followed by Azcarate *et al.* in the case of CO_2-to-CO conversion using Fe porphyrins.[17] Upon increasing the acid concentration, catalysis becomes stronger and the CV response changes from an S-shape to a peak-shape due to the interference of secondary phenomena (substrate consumption and/or partial inhibition of the electrode surface by gas bubbles). Increasing the scan rate (smaller charge transferred at the electrode surface) led back to plateau-shaped CVs and the rate constant for catalysis could be derived from the plateau current. It allowed studying the effect of successive phenyl perfluorination and of *o*,*o*′-methoxy substitution of Fe tetraphenylporphyrin (**Fe1**, **Fe6–Fe9**, Chart 3).

Another example is provided by Co quaterpyridine (**Co20**, Chart 1). The 2-electron reduction of the Co^{II} complex in CH_3CN generates a radical anion (ligand centered reduction). The reduced complex is then adsorbed onto the electrode surface, rendering the CV analysis and quantitative data collection difficult. However, by increasing the scan rate (Fig. 4), the amount of charge passed being smaller, this phenomenon was minimized and proper diffusion-controlled waves were obtained. This further allowed identification and characterization (from plateau current values) of two catalytic pathways for the electrochemical reduction of CO_2 to CO mediated by cobalt quaterpyridine.[18,19] The first one originates from the 2-electron reduction of the catalyst (at 3 M phenol concentration) while at lower acid concentration (1 M phenol) catalysis is triggered after 3-electron reduction of the catalyst, as illustrated in Fig. 4.

The impact of side phenomena on CVs increases as the passed charge increases. Analyzing the foot of the wave (FOWA), where the current is small (small charge), is another strategy minimizing these effects with i/i_0 values being then again proportional to $\left(1+\exp\left[\frac{F}{RT}\left(E-E^0_{P/Q}\right)\right]\right)^{-1}$ as shown from eqn (9).[8] As an example, FOWA has allowed for the derivation of reaction orders toward various acid co-substrates in the reduction of CO_2 to CO mediated by the electrogenerated Fe^0 tetraphenylporphyrin in the presence of phenol as a co-substrate.[20] It was further revealed that after the binding of CO_2 to Fe^0, catalysis involves an electron transfer from the Fe center concerted with proton transfer and C–O bond cleavage. In another example, using FOWA analysis, various Co terpyridine based complexes featuring different substituents on the ancillary ligand (**Co21** and derivatives, Chart 1), were prepared, and studied as catalysts for CO_2 reduction. It was shown that ligand modifications have a small effect on the kinetics of CO_2 reduction while stronger

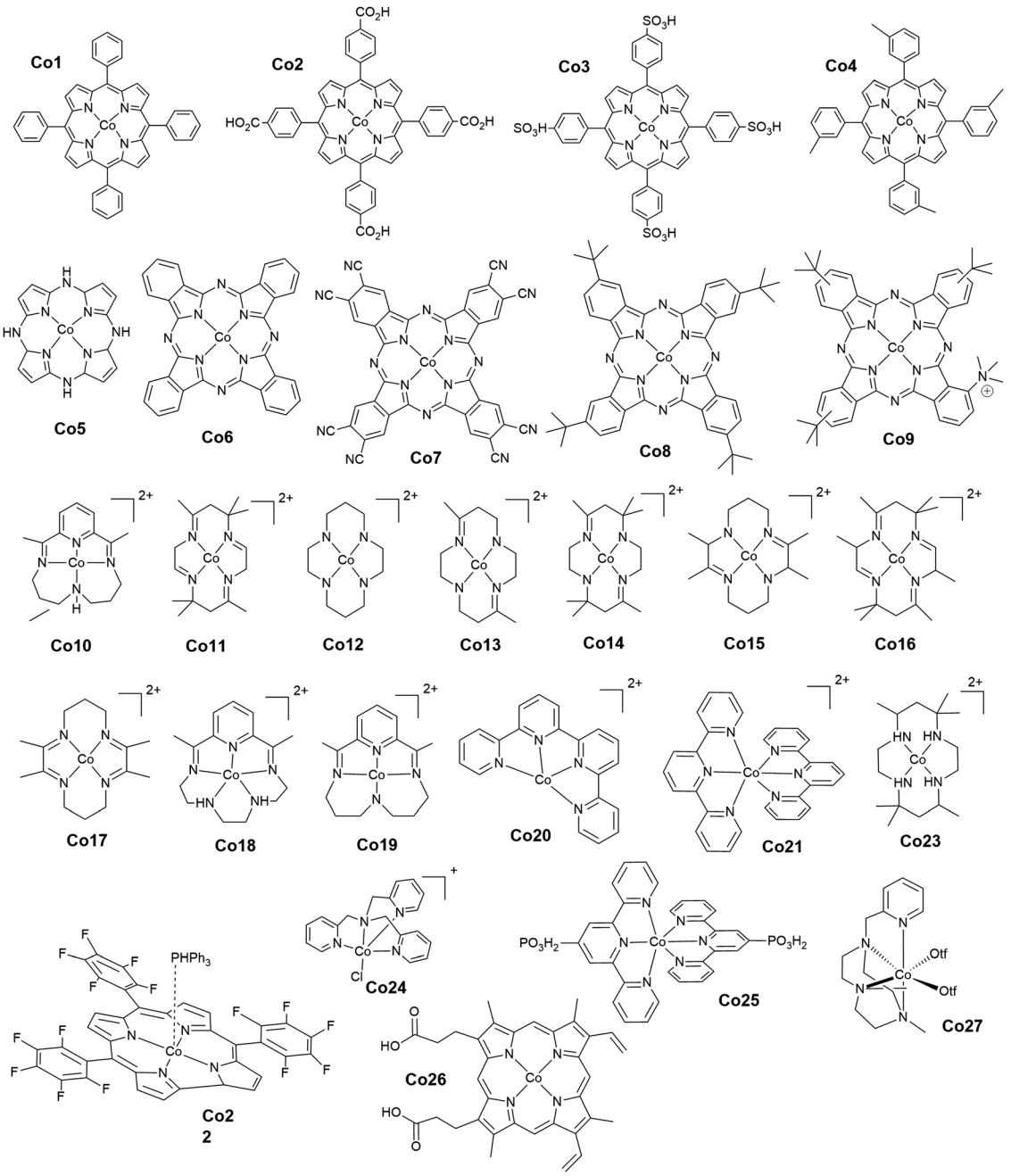

Chart 1 Cobalt complexes.

effects were observed for the competitive proton reduction (HER). Higher rate constants for HER were measured with more electron rich ancillary ligand fields. Thus, slowing down the HER by carefully choosing the catalyst electronic properties resulted in improved selectivity for CO_2 reduction.[21]

The above cases assume a fast electron transfer from the electrode to the oxidized form P of the catalyst. When electron transfer is in contrast slow (or if the follow up reaction is so fast that the initial electron transfer should be viewed as slow), foot of the wave analysis (FOWA) still applies but one should plot $FIT(E - E^0_{P/Q})$ *vs.* $\left(1 + \exp\left[\frac{F}{RT}\left(E - E^0_{P/Q}\right)\right]\right)^{-1}$ as (eqn (10)):[22]

$$FIT\left(E - E^0_{P/Q}\right) = \frac{\frac{i}{i_0}}{1 - 0.446\frac{i}{i_0}\frac{\sqrt{D_P}}{k_s}\sqrt{\frac{Fv}{RT}}\exp\left[\frac{F}{RT}\left(E - E^0_{P/Q}\right)\right]} = \frac{2.24\sqrt{k_e C^0_A}\sqrt{\frac{Fv}{RT}}}{1 + \exp\left[\frac{F}{RT}\left(E - E^0_{P/Q}\right)\right]} \quad (10)$$

In the case of **Fe2**, a complete strategy combining analysis of all segments of the CVs has led to the full characterization of

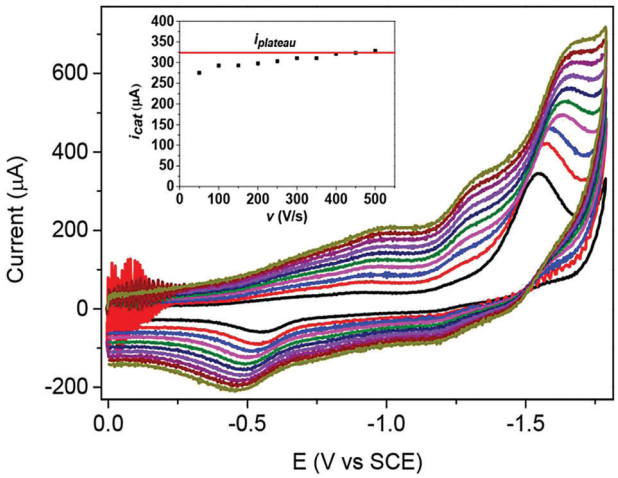

Fig. 4 Plateau-shaped CV (most negative wave) establishment upon increasing the scan rate during CO_2 electrochemical reduction with **Co20** (0.5 mM) in CH_3CN containing phenol (1 M) as a proton source and 0.1 M $(^tBu)_4NPF_6$ as a supporting electrolyte. Scan rate v = 50 (black), 100 (red), 150 (blue), 200 (magenta), 250 (olive), 300 (navy), 350 (violet), 400 (purple), 450 (wine) and 500 V s^{-1} (dark yellow). Inset: Variation of the catalytic current obtained at the third reduction wave (calculated from subtraction of the background current value) as a function of the scan rate. Reprinted with permission from ref. 19. Copyright 2019 American Chemical Society.

the catalytic cycle for CO_2 reduction[8] as shown in Fig. 5 (see Section 1.3 for a complete mechanistic discussion).

Regarding the total catalysis regime (KT zone, Fig. 3), a formal kinetic analysis has been developed in the case of 2-electron/2-step processes, allowing extraction of kinetic parameters and distinguishing between different mechanisms.[23]

Supported molecular catalysts. As convenient as homogeneous molecular catalysts are for mechanistic studies, it is difficult to conceive their implementation in devices since only a small fraction of catalyst close to the electrode surface is active. Attaching these molecular catalysts to an electrode may be a good strategy for efficient use while still benefiting from their good selectivity.[24,25] While rotating disk electrode voltammetry (RDEV) has been widely used for the study of catalyst-containing films, CV is a good alternative when RDEV is hardly applicable (for example when using porous conductive materials as supporting electrodes). With an electrode surface coated with a porous film containing attached molecular catalysts (Fig. 6, top scheme), maximum current density for a fast catalytic reaction will be $I = nFk_{cat}\Gamma_{cat}$ where n is the number of electrons involved (n = 2 for CO or formate production), k_{cat} the catalytic rate constant (assumed to be first order toward CO_2 $k_{cat} = \kappa_A k[CO_2]$) and Γ_{cat} the surface concentration of the catalyst ($\Gamma_{cat} = C_p^0 d_f$). Knowledge of the film thickness d_f and catalyst concentration can then lead to the value of k_{cat}. Such a determination may be hampered by slow charge transport through the film (either in the context of a non-conductive support with charge hopping between catalytic redox sites, or of an electronically conductive support connecting the molecular catalysts).[26,27]

In the framework of fast charge transport and assuming that the molecular catalysts behave as molecular sites (*i.e.* with no

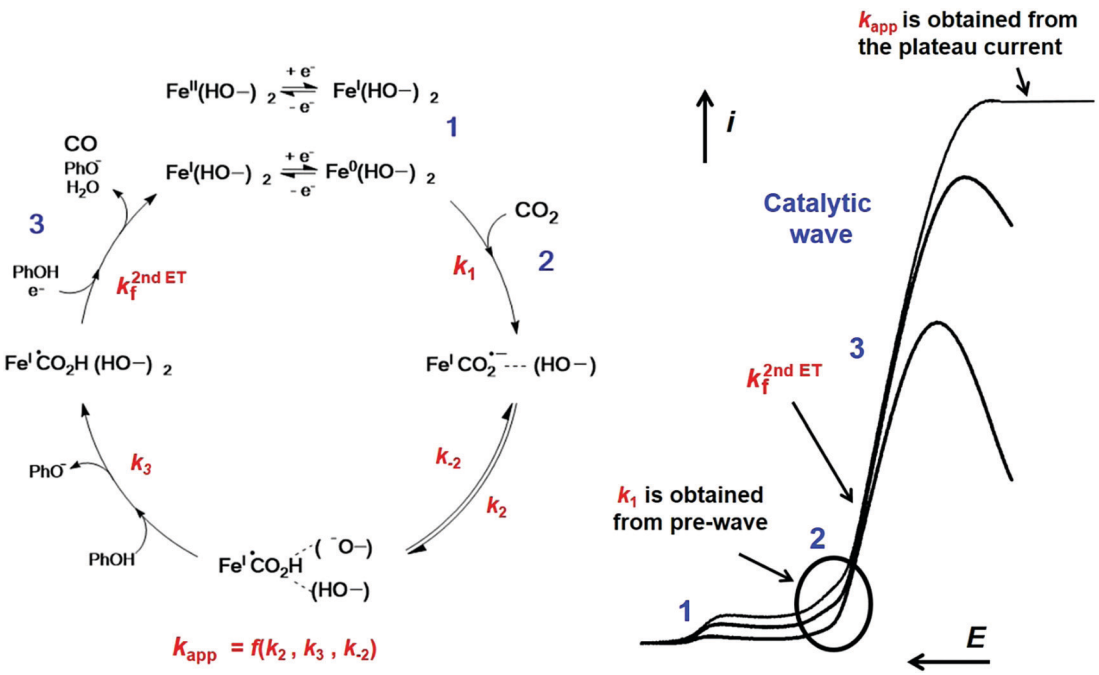

Fig. 5 Molecular catalysis mechanism of CO_2 reduction into CO with **Fe2** in the presence of phenol (PhOH) as a co-substrate. Left: Mechanism for the catalysis obtained from CVs analysis. Right: Catalytic CVs as a function of increasing scan rate, with plateau current at high scan rate. Main kinetic parameters were obtained from the one-electron pre-catalytic wave peak position (k_1), the rise of the current function ($k_f^{2nd,ET}$) and from the plateau current value (k_{app}), respectively. Adapted with permission from ref. 14. Copyright 2017, Elsevier.

strong conjugation of the catalyst molecular orbitals with the conductive support), the current density response for a fast one-electron catalytic reaction will depend on three parameters: the value of k (limiting current density $I_k = Fk\kappa_A C_A^0 \Gamma_{cat} = FkC_p^0 \kappa_A C_A^0 d_f$), the diffusion rate of the substrate in the film (limiting current density $I_S = F\kappa_A C_A^0 \frac{D_S}{d_f}$) and the diffusion rate of the substrate outside the film (current density $I_A = FC_A^0 \sqrt{D_A \frac{Fv}{RT}}$), as illustrated in Fig. 6. This kinetic zone diagram may be extended to multielectron/multistep processes. An appropriate stoichiometric factor should then be introduced.[28,29] The rapid development of hybrid materials with immobilization of molecular catalysts into thin films at electrode surfaces calls for performing thorough mechanistic studies with the above tools. Such studies are currently missing.

1.2.2 Spectroelectrochemistry. Spectroscopic techniques can be used as non-invasive (non-destructive) complementary tools to identify reaction intermediates and/or products. In this regard, the combination of "reaction oriented electrochemistry" and "species-focused spectroscopy" gives rise to spectroelectrochemistry (SEC), a technique aiming at the spectroscopic (UV-vis, IR, X-ray, *etc.*) detection of reaction intermediates generated *in situ* by application of a controlled potential at an electrode.[30] While UV-vis, EPR and XAS spectroscopies can probe the redox state of catalysts, IR and Raman spectroscopies can monitor evolution of carbonyl groups involved in CO_2 reduction. Additionally, labelled experiments are potentially fruitful since bond stretching and vibration are atom weight dependent. Although no standard setup exists, a suitable thin layer cell design is required for SEC experiments. Fig. 9 shows examples of UV-vis and IR-SEC cells.

One of the very first studies regarding SEC studies in the context of CO_2 reduction identified the free anion radical $CO_2^{\bullet -}$ to be the intermediate of CO_2 reduction on lead in water and in some aprotic solvent using UV-vis reflectance spectroscopy.[31] It was also shown that oxalate was produced through the coupling of $CO_2^{\bullet -}$ with CO_2 rather than through dimerization of the radical anion.[31] Later, CO_2 and CO_2–adsorbates on platinum and in acetonitrile were identified using polarization modulation Fourier transform infrared reflection absorption spectroscopy.[32] Reduction of CO_2 under these conditions was shown to yield oxalate.[33]

Focusing on Fe porphyrins, Fe^0 species was detected using *in situ* UV-vis and Raman SEC characterization.[34] It was shown that the two-electron reduction of iron^{II} tetraphenylporphyrin

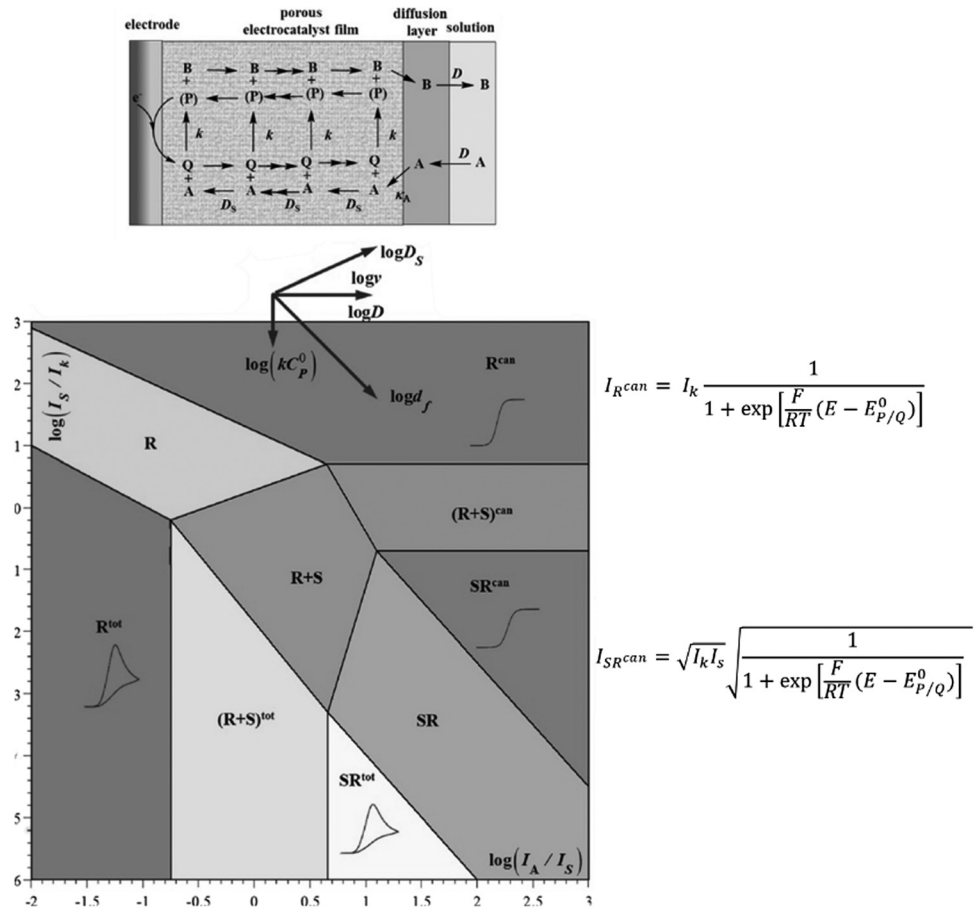

Fig. 6 Kinetic zone diagram for fast conducting catalytic films in the case of a one-electron reaction. Top scheme illustrates a porous film in which the catalyst is attached and is in contact with a conductive support. Adapted from ref. 29 with permission from Elsevier. Copyright 2017.

occurs on the metal center rather than on the porphyrin ring by comparison with data obtained for zinc tetraphenylporphyrin, which is known to yield a diradical anion porphyrin ring (ligand centered reduction). Such a description is still subject to extensive discussion as recent work suggests that reduction of iron tetraphenylporphyrin is not metal- but ligand-centered. Such a conclusion was supported by Mössbauer and X-ray absorption spectroscopy, with additional insight from computational methods.[35] It was also supported by a resonance Raman spectroscopy study of reduced teraphenylporphyrin coupled with quantum chemistry calculations.[36] However, these results do not account for the reactivity of the reduced porphyrin with CO_2 at Fe and for the absence of ligand carboxylation. Additionally, stabilization of the reduced form of the ligand (diradical anion) is not comparable under the conditions usually reported in CO_2 reduction studies (in DMF) and in spectroscopic studies, where much less polar solvents than DMF are used (ethers).[37] Results obtained under these conditions are thus not directly comparable. This underlines the importance of performing *in situ* and *in operando* studies.

Illustrative examples include an iron porphyrin containing triazole substituents (**Fe20**, Chart 3) that facilitate H-bonding. Chemical reduction of the iron porphyrin in the presence of CO_2 and various proton sources was performed at low temperature and some reaction intermediates were trapped and probed by Raman spectroscopy, as illustrated in Fig. 7.[38] It was shown that the chemically generated Fe^0 porphyrin gets oxidized by CO_2, forming a $Fe^{II}CO_2^{2-}$ adduct, which is rapidly protonated to form a Fe–COOH species. At this point, introduction of a relatively strong acid (p-$CH_3C_6H_4SO_3H$) resulted in the cleavage of a C–OH bond and another intermediate was detected, which was shown to be Fe^{II}–CO. In the absence of acid, formate was produced by hydrolysis of the protonated intermediate. These results were qualitatively supported by density functional theory modelling of the Fe–C adducts.[38]

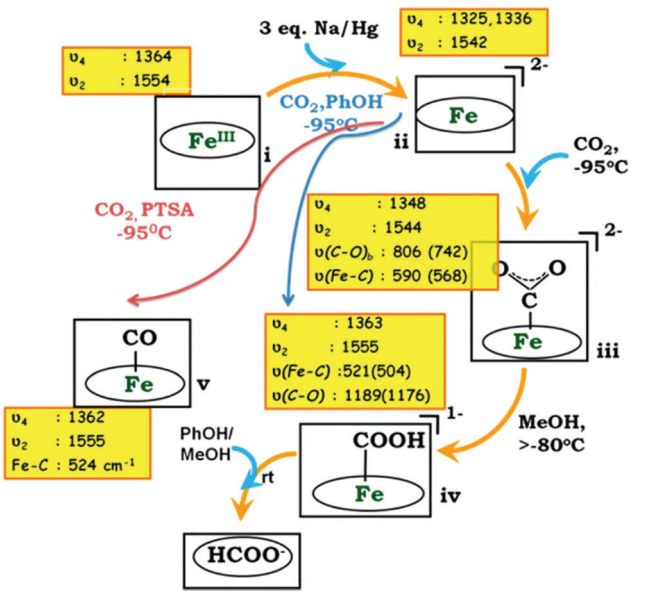

Fig. 7 Proposed mechanism for CO_2 reduction with **Fe20**, from Raman spectroscopic detection of intermediates. Reprinted with permission from ref. 38. Copyright (2015) American Chemical Society.

Keeping with iron catalysts, IR-SEC was performed on an iron Schiff base complex (**Fe21**). It was shown that the formation of stable Fe–CO species with one or two CO molecules coordinated to the Fe center limits the activity of the complex under both protic and aprotic conditions and led to decomposition of the catalyst.[39] This was also the case when **Fe13** was used as a catalyst. In this case, the formation of the Fe^0–CO adduct has been identified as a deactivation pathway, again using IR-SEC.[18]

The IR-SEC has been proven to be beneficial in the study of a binuclear Co complex bearing a bi-quaterpyridine (**$Co_2$3**, Chart 6) photo- and electrocatalyst for the reduction of CO_2 to formate or CO selectively depending on the composition of the reaction medium (see Section 4, Fig. 14).[40] A stable adduct between CO_2 and the four-electron-reduced complex was evidenced by a band at 1635 cm^{-1} upon scanning the potential applied to the Pt grid working electrode from −0.35 to −0.85 V *vs.* Ag pseudo-reference. The configuration of this adduct was shown to involve C atom binding (of CO_2) to one of the Co centers and one of the O atoms binding to the other Co center. Such a configuration with the CO_2 molecule in between the 2 metal centers was supported by computational results. Upon setting the potential at the value of the catalytic wave, a signature related to the formation of a formato-complex or free formate was observed, in agreement with the fact that this complex's selectivity towards formate can be obtained with an appropriate reaction medium composition.

In the case of a cobalt aminopyridine catalyst (**Co27**, Chart 1), a new pathway for the CO_2-to-CO conversion was identified, involving the non-catalytic Co^{II}/Co^{I} redox wave.[41] Upon electrochemical generation of the Co^{I} species in the presence of CO_2, *in situ* IR-SEC shows a signal characteristic of a Co^{I}–CO adduct. Labelled experiment as well as theoretical modelling confirmed the formation of the Co^{I}–CO species. It was postulated that CO release is a key limiting step which prevents fast recovery of the catalytically relevant Co^{I} species. Overall, this study has shown that Co^{I} is nucleophilic enough to bind CO_2 and that C–O cleavage occurs subsequently with no added protons, as represented in Fig. 8. This is not the case with Co porphyrins, for which it has been shown that the Co^{I} complex is unreactive with CO_2 and that the active species towards CO_2 reduction is instead the formal Co^0.[42]

An *in operando* fast-scan FT-IR study of a cobalt catalyst reducing CO_2 to CO under photochemical conditions (**Co10**, Chart 1) has shown that the ability of the one-electron reduced Co^{I} complex to bind with CO_2 plays a critical role. After injection of a second electron to the adduct, a new intermediate (Co^{I}–CO_2^{-}) is formed, as evidenced by the fact that the IR signature of the macrocyclic ligand does not change, meaning that the second electron mainly resides on the bound CO_2. The adduct then cleaves (rate-limiting step) to form CO and the Co^{II} catalyst.[43] Spectro-electrochemistry has also been used with supported catalysts, *e.g.* with cobalt porphyrin-based metal–organic frameworks (MOFs).[44] In this case, UV-visible spectroscopy was used

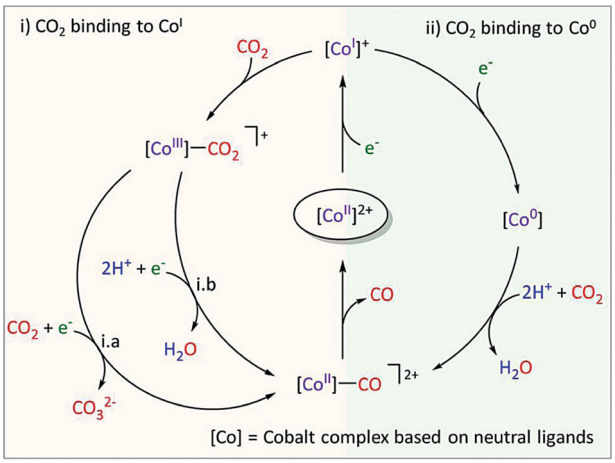

Fig. 8 Proposed mechanism of CO_2 reduction with **Co27**. During CPE at the $Co^{II/I}$ wave, trace amounts of CO were released. A formal oxidation state is given for the different Co species. Reprinted with permission from ref. 41. Copyright (2020) American Chemical Society.

to probe the Co redox state during catalysis of CO_2 reduction. The MOF was directly grown on a transparent electrode and it was shown that the majority of the Co centers were electrically addressed as the Co^I active catalytic species was observed.

With Ni complexes (Chart 2), IR-SEC played a key role in the identification of nickel carbonyl species during CO_2 reduction mediated by Ni(cyclam) (**Ni1**) at a glassy carbon electrode.[50] The detection of species such as $[Ni(cyclam)(CO)]^+$ and $Ni(CO)_4$ helped confirming that catalyst deactivation is caused by carbon monoxide. This was further confirmed by *in situ* observation of $[Ni(TMC)(CO)]^+$ (**Ni6**) (TMC = 1,4,8,11-tetramethyl-1,4,8,11-tetraazacyclotetradecane) when $[Ni(TMC)]^{2+}$ (**Ni6**) was used as a CO scavenger, allowing the catalyst to remain active. The same conclusions were driven when a $[Ni(TPEN)]^{2+}$ (**Ni13**) was studied.[51] Furthermore, the use of optical resonance Raman and electron paramagnetic resonance spectroscopies under catalytic conditions has led to the identification of different pathways for CO_2 and proton reduction with **Ni1**, suggesting that a careful catalyst design can suppress the competing hydrogen evolution reaction and may thus lead to more selective catalysts.[52]

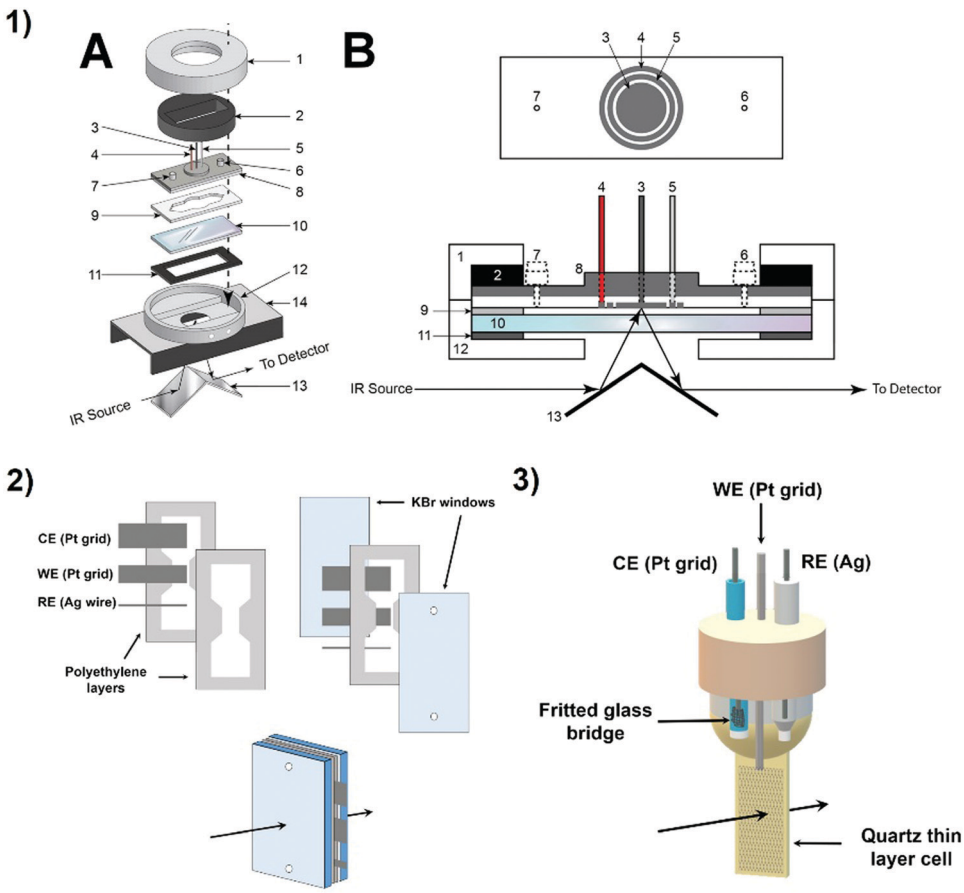

Fig. 9 Examples of spectro-electrochemical cells. (1) IR specular reflectance – SEC cell: 1. tightening brass cap (threaded inside); 2. brass ring required to tighten the cell; 3. WE; 4. CE; 5. pseudo-RE; 6 and 7. injection ports; 8. cell body, top part aluminum, lower part Teflon; 9. Teflon spacer; 10. CaF_2 window; 11. rubber gasket; 12. hollow brass cell body with threaded inlet and outlet ports (Swagelock) for connecting to the circulating bath; 13. mirrors; 14. two-mirror reflectance accessory; A: disassembled view, B: cross-sectional drawing of the cell;[45] reproduced with permission from ref. 49. Copyright (2014) American Chemical Society. (2) IR transmission – SEC cell;[46,47] (3) UV-Vis-SEC quartz cell.[48]

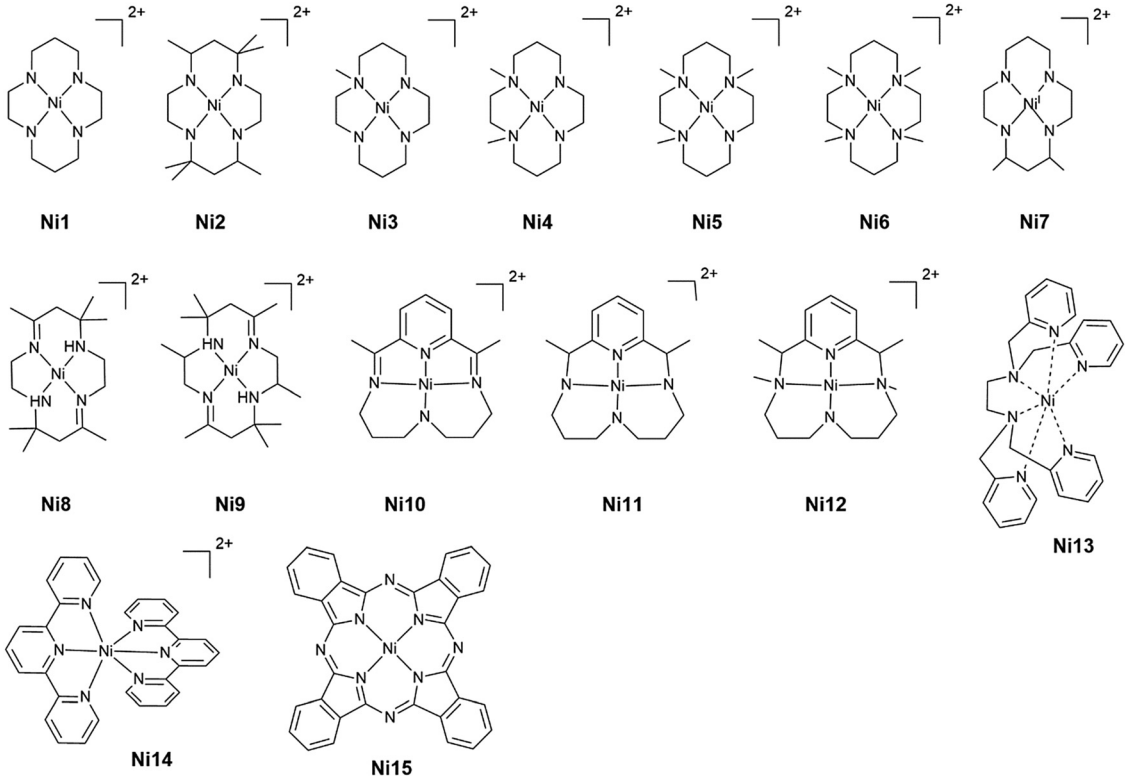

Chart 2 Nickel complexes.

1.2.3 X-ray absorption spectroscopy. X-ray absorption spectroscopy methods have recently emerged as a powerful source of information for investigating the redox state of the metal center as well as its coordination environment and geometry.[53] For example, X-ray absorption near-edge spectroscopy (XANES) has shown that $[Co^{I}HMD]^{+}$ and $[Co^{II}HMD]^{2+}$ (**Co14**, Chart 1) have a square planar geometry. It changes to a square pyramidal geometry upon axial coordination of CO_2 to $[Co^{I}HMD]^{+}$. The resulting Co^{III}–carboxylate species was identified and indicated charge transfer from the Co center to CO_2. Binding of a solvent molecule to the metal center was also evidenced.[54] Binding of CO to an iron porphyrin (**Fe10**, Chart 3) has also been studied by XANES. The porphyrin was immobilized on a carbon material and analyzed *in situ*. Introduction of CO to the electrolyte solution resulted in binding to electrogenerated Fe^{II} porphyrin and formation of an L–Fe–CO adduct, L most probably being a water molecule. Charge transfer from iron to CO was further postulated to explain the shift of the Fe K-edge to higher energy values.[55]

Similar information has been obtained with Ni containing tetraazamacrocycles.[56] The one-electron reduction/oxidation of the Ni^{II} starting complexes resulted in an energy shift of the absorption edge in XANES spectra. Moreover, the intensity of the pre-edge peak yielded information on the coordination environment. It was found that the starting Ni^{II} species is hexa-coordinated to the macrocycle and two solvent molecules that are lost upon reduction to Ni^{I}. After binding of CO as an axial ligand to Ni^{I}, the absorption edge is shifted to higher energy, showing that some charge transfer occurs from the metal center to the CO ligand.

Regarding catalytic studies, these techniques were used for the study of oxygen reduction catalysts.[57–61] CO_2 reduction studies with *in situ* XAS are now developing rapidly.[41,62,63] *Ex situ* XAS is a valuable complementary tool for analyzing immobilized molecular catalysts and their stability after performing CO_2 reduction.[64,65] Recently, catalysis with a cobalt aminopyridine (**Co27**) was investigated by combination of XAS, IR and UV-vis SEC experiments. Formation of a Co^{I} species (from one-electron reduction of the starting complex) under an inert atmosphere was first evidenced, upon performing an electrolysis at a potential slightly more negative than the $Co^{II/I}$ redox wave in anhydrous deuterated acetonitrile at −40 °C. The frozen sample was then analyzed by XANES and EXAFS. Under a CO_2 atmosphere, formation of a Co^{II}–carbonate complex was evidenced by both XANES and EXAFS, upon comparing spectra with those of the chemically produced species upon mixing the starting Co^{II} complex with tetrabutylammonium hydrogenocarbonate. However, the key Co^{I}–CO species was not observed under these conditions. Nevertheless, these experiments helped identifying one of the key bottleneck intermediates for CO_2 reduction. It was indeed confirmed by cyclic voltammetry that the Co^{II}–carbonate species disfavors the catalytic reduction of CO_2 at the $Co^{II/I}$ wave.[41]

It should also be emphasized that XAS experiments remain tedious and include selecting suitable synchrotron/beamline for a given experiment.[66] As for the more practical side, and similarly to UV-vis and IR SEC, no standard setup exists. Using a thin layer cell comprising windows transparent to the incident light is mandatory, and experiments can be performed either in

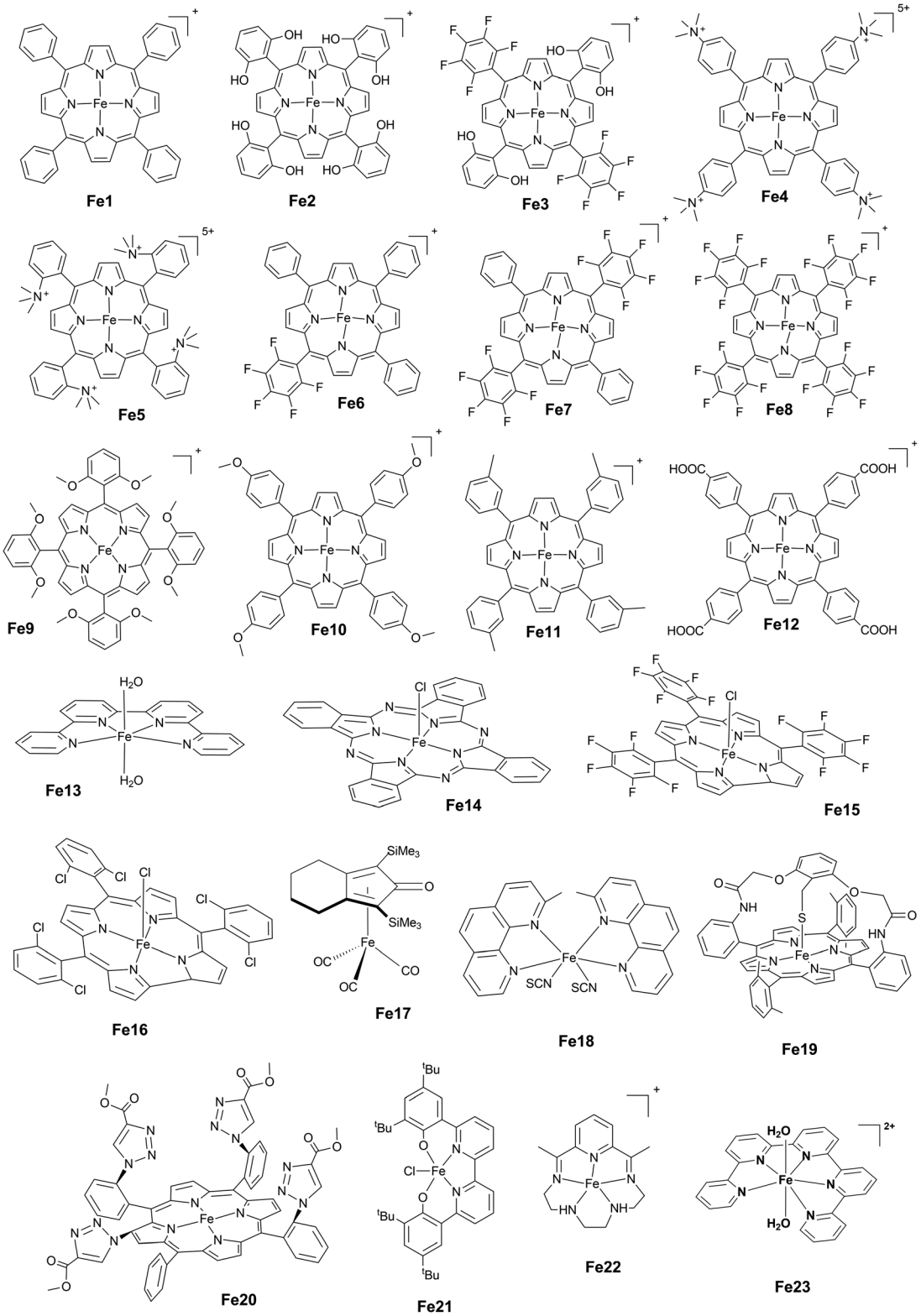

Chart 3 Iron complexes.

transmittance or fluorescence mode, although the latter is usually preferred.[67] Fig. 10 shows examples of typical XAS-SEC cells. Although X-ray absorption spectroscopy is not a routine technique, the field of electrocatalytic transformations using molecular complexes under homogeneous conditions and supported catalysts might strongly benefit from information it can provide. *In operando* studies with time-resolved techniques would be a valuable asset in the deciphering of reaction mechanisms.

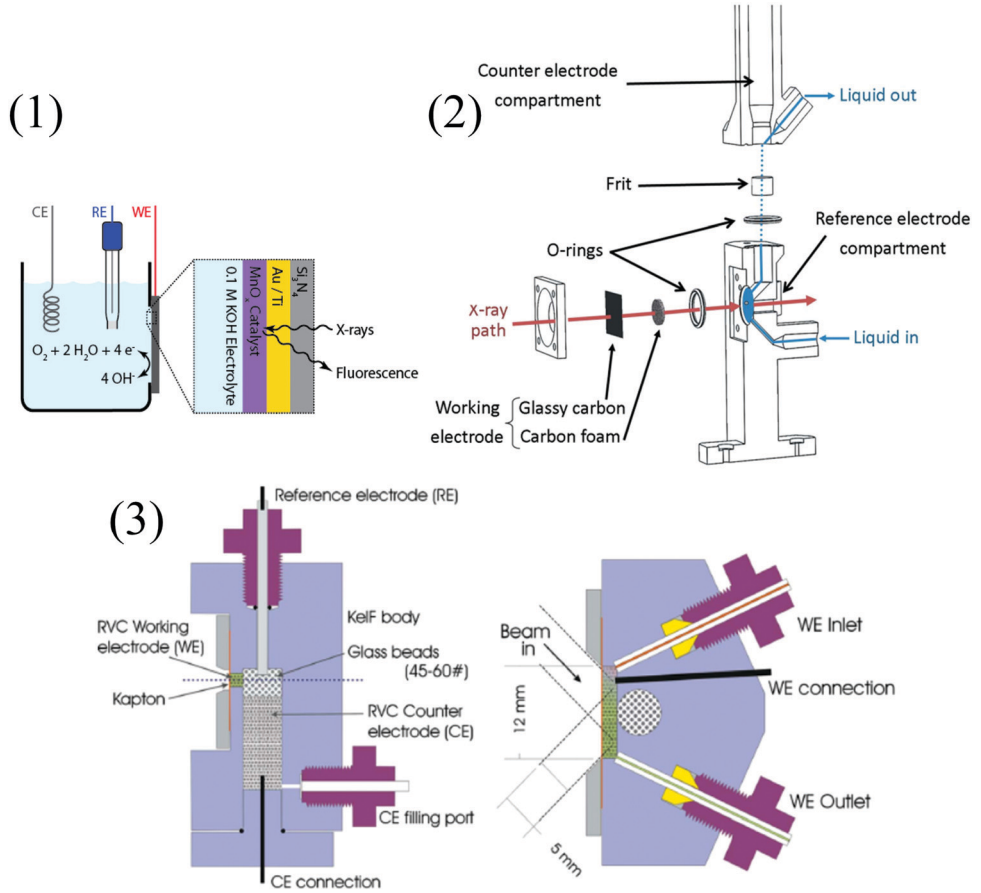

Fig. 10 Examples of XAS-SEC cells. (1) *In situ* XAS setup, with the back side of the Si_3N_4 window facing the X-rays and the front side of the window covered with electrodeposited MnOx on a layer of Au/Ti facing the electrolyte. CE, RE, and WE stand for counter, reference, and working electrodes, respectively; reprinted with permission from ref. 69, copyright (2013) American Chemical Society. (2) Detailed view of a spectroelectrochemical cell developed for time-resolved data collection in transmission mode;[70] and (3) vertical (left) and horizontal (right) sections through the working electrode chamber of a fluorescence X-ray absorption spectroscopy spectroelectrochemical (XAS-SEC) cell (RVC = reticulated vitrous carbon). Solution flow control is achieved using syringe pumps and Teflon tubing. The inlet and outlet tubes of the WE are sealed with the aid of Teflon ferrules; a flanged seal was used for the CE tubing.[71]

It may lead to a better understanding of catalytic systems and to their improvement.[68]

1.2.4 Differential electrochemical mass spectrometry. Differential electrochemical mass spectroscopy (DEMS) is an analytical technique combining *in situ* coupling of mass spectrometry to electrode processes. Gaseous and volatile compounds produced at an electrode by application of a controlled potential can be sampled through a microporous (mostly PTFE) membrane to a mass detection chamber upon application of high vacuum (Fig. 11). This technique allows for the fast characterization of reaction products as a function of the applied potential and it may be an interesting alternative to the tedious job of performing electrolysis at various potentials.[72] Two cell setups have been mainly used in the context of CO_2 electrochemical reduction: thin layer flow cells[73–76] and cells using a capillary inlet, usually referred to as on line electrochemical mass spectrometry (OLEMS).[77–82] The DEMS cell architecture has evolved over time. The technique was first demonstrated using a design where the electrode material was directly deposited onto a PTFE membrane that was supported on a stainless steel grid connected to vacuum for MS analysis. The rest of the electrochemical cell was rather conventional and was assembled by pressing the body of the cell on the working electrode.[72] Although this design shows good collection efficiency and a fast spectrometer response, the choice of electrode materials that can be used is rather limited, and the study of bulk materials such as Cu electrodes is not allowed. Additionally, the electrode surface is positioned very close to the membrane (hence to the vacuum system). As a consequence, the concentration of volatile species at the electrode surface decreases, leading to depletion of CO_2.[83]

The thin layer design was first introduced in 1990, allowing processes occurring on smooth electrodes to be studied.[84] In this design, the working electrode is separated from the PTFE membrane by a thin solvent layer. As a result, species produced at the electrode have to diffuse to the membrane. Consequently, slower spectrometry responses were observed. When the cell is under continuous flow, it results in low collection efficiency as diffusion of analytes to the membrane competes with the solvent flow.

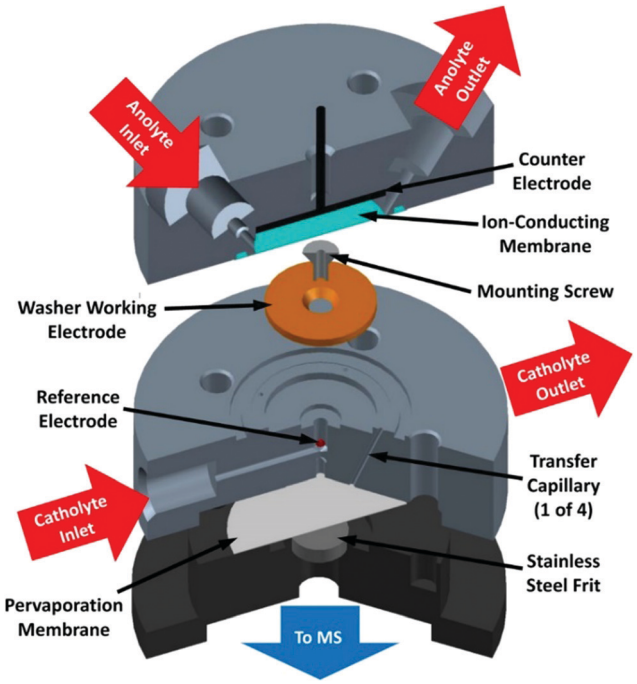

Fig. 11 DEMS cell. Reprinted with permission from ref. 74. Copyright (2015) American Chemical Society.

A number of these flaws were addressed more recently with the design of a new DEMS cell.[74] This design features parallel working and counter electrodes to ensure uniform potential distribution across the surface of the electrodes and a reference electrode located outside the working electrode chamber to prevent the formation of gaseous product bubbles that may affect potential referencing. Again, the working electrode is separated from the pervaporation membrane to prevent CO_2 depletion, but the electrolyte volume between the working electrode and the pervaporation membrane is minimized to allow a short delay time between product generation and detection.[78,85]

In the OLEMS design, a classical 3 electrode cell configuration is adopted and a PTFE microporous membrane terminated capillary (pinhole inlet) is placed close to the working electrode (10–20 μm) in a hanging meniscus configuration. This particular configuration allows the study of CO_2 reduction over single-crystal electrocatalysts. The capillary inlet can be attached to a 3D piezoelectric-driven positioning system (scanning DEMS) allowing the mapping of large electrodes and screening of multiple electrodes within a single experiment.[86] However the OLEMS configuration has a number of flaws, notably a low collection efficiency.

Despite the possibilities offered by DEMS not only to study catalysts on a short time scale but also to follow both activity and selectivity in real time, the technique has not yet been widely used with molecular catalysts. Only one study performed on Ni(cyclam) (**Ni1**) was reported.[87] CO (m/z = 28) production in the course of cyclic voltammogram recorded at a slow scan rate was evidenced, along with depletion in the signal corresponding to CO_2 (m/z = 44). Hydrogen evolution at potentials more negative than the catalytic wave was also identified. More recently, the OLEMS configuration has been adopted for the study of Co protoporphyrin (**Co26**, Chart 1) immobilized on pyrolytic graphite (see Section 5).[82] Special attention should be paid to the analysis of CO_2 reduction products. It is usually admitted that CO is undetectable by DEMS because its ionization produces the same mass fragments as CO_2 while this latter can be orders of magnitude more concentrated in the electrolyte. Moreover, under experimental conditions where formic acid is fully dissociated, it cannot pervaporate to the mass spectrometer, thus preventing its detection.[74] In other words, DEMS should be used as a complementary experimental method.

1.3 Homogeneous molecular catalysts. Molecular metal-based electrocatalysts including Fe, Ni or Co have been extensively studied and reviews may be consulted.[2–6] Although general structure–reactivity relationships are difficult to establish (even for the reduction of CO_2 to CO and formate), rational functionalization of the ligands in order to modulate electron density at the metal and to provide a favorable environment for proton relay and proton transfer has progressively led to excellent performances. Such guided design is a cornerstone for getting even better performances and triggering new reactivity. Illustrative and historical examples are detailed below and most efficient catalysts are summarized in Table 1. Scheme 3 at the end of the section summarizes the 2-electron reduction mechanisms.

1.3.1 Cobalt complexes. The use of earth abundant metal complexes for the electrochemical reduction of CO_2 under homogeneous conditions was reported as early as 1974, when cobalt and nickel phthalocyanine catalytic activity was reported by cyclic voltammetry.[1] They were shown to be active for the CO_2-to-CO conversion.[88] Co porphyrins were identified as effective catalysts in 1979 but no catalytic activity was noticed at that time for Fe and Cu porphyrins.[89] In aqueous buffered solutions catalytic reduction of CO_2 with **Co2** (Chart 1) at a potential E = −1.3 V *vs.* NHE leads to formic acid. Catalytic activity was also observed with **Co3** (Chart 1) but the products were not identified. It was suggested that both metal center and ligand structure played an important role in the catalytic process.

Cyclam **Co14** (Chart 1) was also identified very early[90] as a good CO_2 catalyst with a faradaic efficiency of 46.5% for CO production in a mixture of water and acetonitrile (2 : 1, v : v) at a potential E = −1.60 V *vs.* SCE (mercury pool electrode). Related complex **Co18** (Chart 1) shows good catalytic activity with 82% FE for CO production at −1.5 V *vs.* SCE in DMF (Table 1).[91] **Co19** (Chart 1) is less selective with 30% FE for CO at a potential of −1.4 *vs.* SCE in acetonitrile (pyrolytic graphite electrode, 0.5 h).[92] A methylated analog of **Co19** was also reported to reduce CO_2 to CO (45% FE) in wet CH_3CN,[93] as well as under photochemical conditions when associated with $Ru(bpy)_3$ as a sensitizer.[94]

Aminopyridyl macrocycle **Co5** (Chart 1) is in contrast highly selective, with 98% of FE for CO production at E = −2.46 V *vs.* Fc^+/Fc and a TOF of 16 900 s^{-1}.[95,96] The catalyst was suggested to undergo a two-electron metal-based reduction, Co^0 being the catalytically active species. The N–H groups on the ring structure of the ligand were shown to provide assistance for creating

Table 1 Performances of typical Fe, Ni and Co molecular catalysts under homogeneous conditions for the 2-electron reduction of CO_2

Catalyst	Concentration (mM)	Conditions	Duration (h)	Potential (V)	TOF or TOF_{max} (overpotential, method)	Product	FE (%)	Ref.
Fe1	1	DMF, 0.1 M PhOH, Hg pool	1	−1.46 *vs.* NHE	$TOF_{max} = 10^{4.2}$ s^{-1} (η = 800 mV; CV)	CO	100	20
Fe1	1	DMF, 40 mM PrOH, 40 mM NEt_3[a]	4	−2.4 *vs.* Fc^+/Fc	—	Formate	72	112
Fe2	1	DMF, 2 M PhOH, Hg pool	4	−1.16 *vs.* NHE	$TOF_{max} = 10^{3.8}$ s^{-1} (η = 800 mV; CV)	CO	95	22 and 109
Fe3	1	DMF, 3 M PhOH	3	−1.28 *vs.* NHE	$TOF_{max} = 10^{4}$ s^{-1} (η = 800 mV; CV)	CO	95	109 and 110
Fe4	0.5	H_2O, pH 6.7	72	−0.86 *vs.* NHE	$TOF_{max} = 10^{4.2}$ s^{-1} (η = 500 mV; CV)	CO	98	109
Fe5	0.5	DMF, 0.1 M H_2O, 3 M PhOH	84	−1.2 *vs.* SCE	$TOF_{max} = 10^{6}$ s^{-1} (η = 220 mV; CV)	CO	100	111
Ni1	0.17	H_2O, pH 4.1, Hg pool	4	−1.05 *vs.* NHE	TOF = 32 h^{-1} (η = 700 mV; CPE)	CO	96	100
Ni1	0.4	DMF, 0.1 M $NaClO_4$, Hg pool	5	−1.4 *vs.* SCE	TOF = 0.64 h^{-1} (η = 360 mV; CPE)	Formate	75	26
Ni2	1.2	H_2O/CH_3CN 2 : 1 (v : v), 0.1 M $LiClO_4$	1	−1.6 *vs.* SCE	TOF = 6 h^{-1} (η = 640 mV; CPE)	CO	65.3	90
Ni14	Nr	DMF/H_2O 95 : 5 (v : v)	3	−1.71 to −2.14 *vs.* Fc^+/Fc	—	CO	18	22
Co20	0.5	CH_3CN, 3 M PhOH, GC	3	−1.1 *vs.* SCE	TOF = 533 s^{-1} (η = 140 mV; CPE) $TOF_{max} = 3.3 \times 10^4$ s^{-1} (η = 300 mV; CV)	CO	90	18
Co13	1.2	H_2O/CH_3CN 2 : 1 (v : v), 0.1 M KNO_3, Hg pool	1	−1.6 *vs.* SCE	TOF = 7.8 h^{-1} (η = 640 mV; CPE)	CO	46.5	90
Co18	1	DMF	1	−1.5 *vs.* SCE	TOF = nr (η = 566 mV; CPE)	CO	82	91
Co19	1	CH_3CN, pyrolytic graphite	0.5	−1.4 *vs.* SCE	TOF = nr (η = 440 mV; CPE)	CO	30	92
Co5	0.5	DMF,1.2 M TFE, 0.1 M $(tBu)_4NPF_6$	2	−2.8 *vs.* Fc^+/Fc	TOF = 170 s^{-1} (η = 850 mV; CPE) $TOF_{max} = 1.7 \times 10^4$ s^{-1} (η = 510 mV; CV)	CO	98	93 and 95
Co21	2	DMF/H_2O 95 : 5 (v : v)	3	−1.93 *vs.* Fc^+/Fc	—	CO	20	97

[a] Triethylamine.

an efficient H-bond network with the acid co-substrate, further accelerating the rate-determining C–O bond cleavage. Cobalt polypyridines are also highly active catalysts. Quarterpyridine **Co20** (Chart 1) proved to be a very active catalyst for CO_2 to CO reduction in acetonitrile solution, once doubly reduced at an electrode. In the presence of 3 M phenol as a weak acid co-substrate, high product selectivity (96%) and FE (90%) for CO were obtained at a very low overpotential of 140 mV.[18] Moreover, **Co20** proved to be among the most active molecular catalysts for CO_2 reduction with a maximum TOF of 3.3×10^4 s^{-1}, obtained at only 300 mV overpotential. **Co21** (Chart 1) was reported to yield CO with 20% FE ($E = -1.93$ V *vs.* Fc^+/Fc) in a DMF/H_2O mixture (95/5, v : v) at a glassy carbon electrode.[97] Catalytic reaction mechanism for **Co21** was suggested to proceed through a metal centered reduction followed by a one electron ligand centered reduction, triggering loss of a neutral terpyridine ligand. It opens a coordination site for the low valent Co^I species to coordinate CO_2 and reduce it into CO in the presence of protons. The ligand centered reduction was in addition proposed to promote side reactions such as carboxylation or hydrogenation, giving a rational to the low FE. These contrasting results obtained with **Co20** and **Co21** illustrate how a simple change in the coordination environment can drastically affect both efficiency of the catalyst and its stability.

1.3.2 Nickel complexes. Ni cyclams such as **Ni1–9** (Chart 2) were demonstrated to be catalytically active for CO_2 reduction very early and were extensively studied since then.[90,98] Initially, methylated Ni cyclam **Ni2** was shown to yield CO and H_2 in a 2/1 ratio (with a total FE of 98%) with a TOF of 6 h^{-1}, at a potential of −1.6 V *vs.* SCE (mercury pool) in a CH_3CN/H_2O mixture (2 : 1). A few years later, the simplest Ni cyclam **Ni1** was shown to be a highly efficient catalyst.[99–101] The ability of the cyclam ring to stabilize the Ni complexation and the acidic character of the N–H proton of the ligand were recognized as key factors to explain the remarkable reactivity. In acidic water (pH 4–5), high TON (116) and FE were obtained at an Hg electrode, with a TOF of 32 h^{-1} and a selective conversion of CO_2 to CO with only 0.03% of H_2 at the relatively negative potential of −1.05 V *vs.* NHE, corresponding to 700 mV overpotential.

A mechanism was proposed from these studies for the CO_2 conversion to CO in water (Scheme 1), which accounts for the adsorption of the catalyst at the electrode surface and for the formation of a Ni^I–CO adduct. Further reduction of this adduct may lead to Ni^0 species and deactivation of the catalyst.

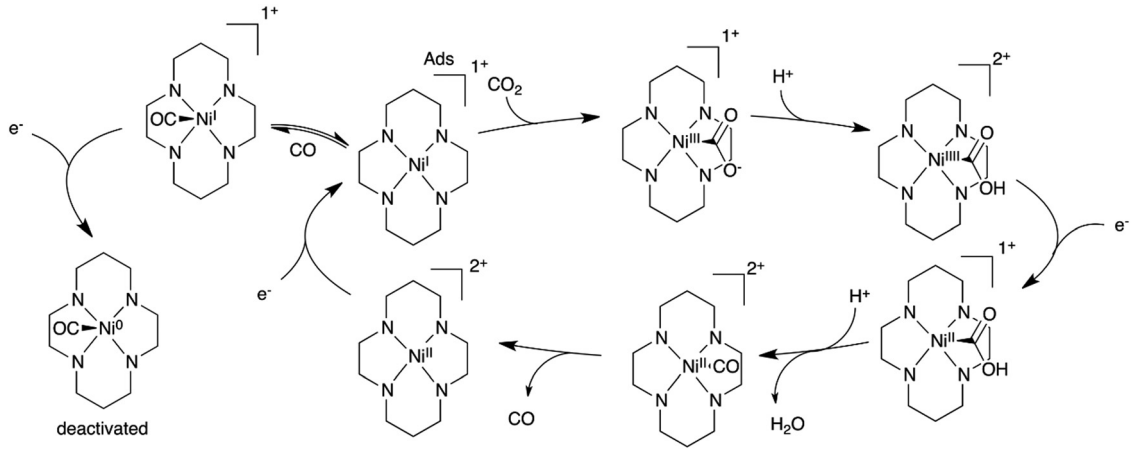

Scheme 1 Proposed electrochemical reduction mechanism of CO_2 to CO in water with the **Ni1** catalyst adsorbed at a Hg electrode.

Following investigations confirmed that the negatively charged mercury surface can adsorb the Ni^I complex and may favor a *trans*-I structure (with N–H groups being all oriented toward the same axial coordination site) which can then effectively bind CO_2 and catalyze its reduction at the electrode surface.[102–104] Further DFT calculations suggested that the *trans*-III isomer, which possesses a chair like conformation (it accounts for 85% of **Ni1**), is in fact more strongly adsorbed at mercury. It leads to a Ni^I–CO adduct which is higher in energy, accelerating the CO loss and thus the catalysis.[105,106] Recent studies at an inert glassy carbon electrode confirmed the formation of the Ni^I–CO species, as well as the CO loss as the rate limiting step.[50,105] Remarkably, **Ni6** could be used as a CO scavenger (stronger affinity for CO than **Ni1**) while having at the same time a lower reactivity towards CO_2 reduction. In a CH_3CN/water mixture (1/4, v : v), CO was then produced with 90% FE at −1.21 V *vs.* NHE (470 mV overpotential, 1 h electrolysis).

CO_2 reduction with **Ni1** in DMF solution leads to the formation of formate with high selectivity. A typical electrolysis experiment showed 75% FE at $E = -1.4$ V *vs.* SCE, CO being the by-product.[101] This change of product selectivity as compared to aqueous solutions was ascribed to preferred protonation on the carbon atom of CO_2 and formation of a nickel-formato intermediate Ni^{II}–OCHO, and it was suggested that no hydride was formed. A related uncommon mechanism for formate production has been recently evidenced with Fe porphyrin (see below and Scheme 3). In contrast, nickel tetraaza macrocycles bearing pyridine functional groups (**Ni10–12**) were also carefully investigated but such systems have weak activity toward CO_2 reduction.[92]

Finally Ni bis-terpyridine **Ni14** was also investigated in a range of potentials (from −1.71 to −2.14 V *vs.* Fc^+/Fc) in a DMF/H_2O mixture (95/5, v : v) and led to only CO.[97] Nevertheless, the FE for CO does not exceed 18% with most of the charge passed during electrolysis not related to CO_2 reduction products. As in the case of the related cobalt compound **Co21**, the doubly reduced catalyst led to the loss of one tpy ligand, promoting side reactions and leading to limited efficiency.

1.3.3 Iron complexes. Variously substituted Fe tetraphenyl porphyrins (Chart 3) have shown to be among the most active molecular catalysts for the CO_2-to-CO conversion. Under some experimental conditions, they have also been able to produce formate.[2,112] Reactivity is triggered by electrogeneration of the Fe(0) active species, which can bind to CO_2 efficiently, leading to an intermediate $^-Fe^I$–$CO_2^{\bullet -}$ ↔ Fe^{II}–CO_2^{2-} adduct which upon protonation will lead to C–O bond cleavage and formation of an Fe^{II}–CO adduct that releases CO upon a one-electron reduction.

Weak Brønsted acids accelerate the catalysis[107] and it was first observed that addition of CF_3CH_2OH to a solution of **Fe1** led to 94% FE and a TOF of 40 h^{-1} in electrolysis experiments in DMF at a mercury pool ($E = -1.70$ V *vs.* SCE). The role of these weak acid co-substrates is to stabilize the Fe–CO_2 adduct and promote bond cleavage. The use of a slightly more acidic acid such as Et_3NH^+ ($pK_a = 9.2$ in DMF) promotes the formation of H_2, demonstrating the importance of pK_a control for such assisted catalysis. Lewis acids such as Ca^{2+} or Mg^{2+} also accelerate the CO_2-to-CO conversion, again upon stabilization of the adduct Fe–CO_2. CO cleavage is then fostered by a second CO_2 molecule leading to CO_3^{2-} and CO as reaction products.[108] Installing the acid function directly on the phenyl ring of the porphyrin with phenol groups in ortho positions (**Fe2**) ensured proton availability (both for H-bonding stabilization properties of the Fe–CO adduct and proton relay assistance for protonation steps) and fast kinetics, with a TOF of $10^{3.8}$ s^{-1} at an overpotential of 0.56 V in DMF solution as determined by cyclic voltammetry.[22]

The crucial role of the OH groups was further demonstrated upon comparison with **Fe9** (substituted with methoxy groups in all ortho positions), which led to a TOF of only $10^{1.3}$ s^{-1} at 1.04 V overpotential. Conversely, introduction of electron withdrawing fluorine moieties on the phenyl rings of the ligand (**Fe6**, **Fe7** and **Fe8**) allowed decreasing the overpotential, but at the expense of a lower activity. This lower activity is the effect of a smaller electron density on the Fe(0) center produced by the fluorine withdrawing group and hence a less stabilized metal–CO_2 adduct. Such an through-structure effect reflects a trade-off between activity and overpotential, and it has been the object of a thorough investigation.[39] When the through-structure effect (electronic withdrawing groups on the ligand) was combined

with the through-space effect of OH groups in the ortho position of the phenyl (**Fe3**), the catalytically active Fe^0 species was generated at 200 mV less cathodic potential than **Fe2**, keeping the high activity and high selectivity of the **Fe2** catalyst (maximum TOF at large overpotential in the range of 10^4 s^{-1}, see Table 1, entries 3 and 4).[109,110] With both **Fe2** and **Fe3**, a mono-electronic pre-wave was observed at the foot of the catalytic wave and it was ascribed to the signature of an Fe^0–CO_2 adduct, which after protonation, requires a second electron reduction for the C–O bond cleavage to occur (concerted dissociative electron and proton transfer). It stands in contrast to the mechanism followed by **Fe1**, for which the second electron transfer occurs after bond breaking, and leads to CO release from the Fe^{II}–CO adduct.

Water soluble porphyrins[109] **Fe4** and **Fe5** bearing four positive charges (trimethylammonium groups) at the *para*- and *ortho*-positions of the phenyl rings respectively show high activity at very low overpotential. Both **Fe4** and **Fe5** show FE close to 100% for CO during electrolysis performed in DMF (0.1 M NBu_4PF_6, 0.1 M H_2O) under 1 atm CO_2 in the presence of 3 M PhOH.[111] Mechanistic studies by cyclic voltammetry in DMF have shown a $TOF_{max} = 10^{4.2}$ s^{-1} at 500 mV overpotential for **Fe4** and $TOF_{max} = 10^6$ s^{-1} at 220 mV overpotential for **Fe5**. A comparison with a series of porphyrins variously substituted at the phenyl rings showed positive effects on both thermodynamics (smaller overpotential) and simultaneously on kinetics (large rate constant) of the positive charges borne by **Fe4** and **Fe5**, which was assigned to through-space stabilization of the Fe^0–CO_2 adduct (Scheme 2).[17,111] This effect brought by positive charges allowed overcoming the intrinsic trade-off of the through structure effect. However, a full mechanistic picture is still missing in both aprotic and protic solvents.

It was recently discovered that product selectivity for CO_2 reduction with **Fe1** as a catalyst could be tuned and changed to formate in DMF, upon addition of a tertiary amine such as triethylamine, with up to 72% FE. Upon careful mechanistic investigation by cyclic voltammetry, formation of an iron hydride intermediate could be ruled out and the proposed mechanism instead suggests that the amine acts as an axial *trans* ligand that enhances the basicity of the carbon atom of the Fe–CO_2, directing the reaction toward formate (Scheme 3b).[112] This new mechanism shed light on the under-investigated role of *trans* ligand in CO_2 reduction with nitrogen containing macrocyclic complexes and will certainly lead to further developments.

1.4 Supported molecular catalysts. Various supports such as metal oxides and carbon materials have been used. Porous

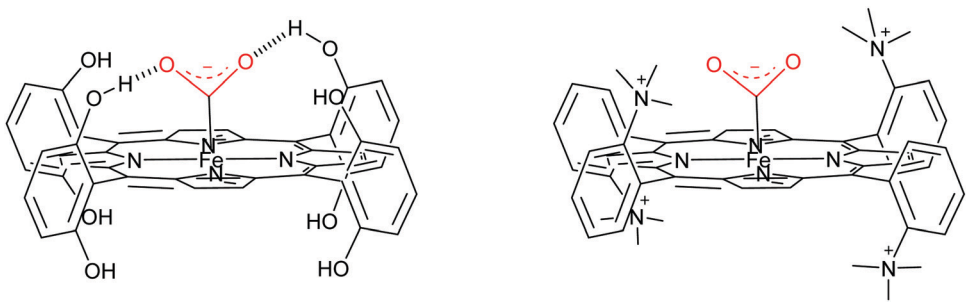

Scheme 2 Contrasting H-bond (left, **Fe2**) and through space electrostatic effect (right, **Fe5**) stabilization in Fe(0) porphyrin–CO_2 adducts.

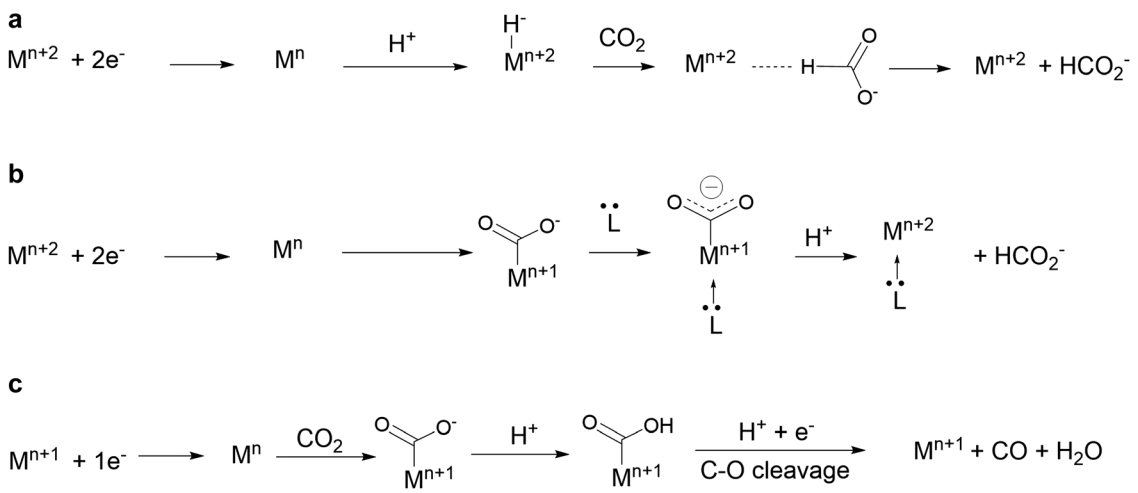

Scheme 3 (a and b) Pathways for the two-electron CO_2 reduction to formate involving a metal-hydride (a) or a metal carboxylate (b) as an intermediate. Pathway (b) has been shown to be followed with **Fe1** in the presence of tertiary amines in DMF solutions.[40] (c) Pathway for the two-electron CO_2 reduction to CO. M^n is the active form of the catalyst.

Table 2 Recent performances for some Co and Fe aza macrocycles and polypyridine catalysts supported at carbon electrodes

Catalyst	Surface concentration (nmol cm^{-2})	E (V *vs.* RHE)	Electrolyte	j_{CO} (mA cm^{-2})	TOF (s^{-1})	Selectivity (%)	Cell type	Ref.
Co9	14.4	−0.676	$NaHCO_3$ 0.5 M	18.1	6.8	93	H cell	115
Co6	23.3	−0.676	$NaHCO_3$ 0.5 M	13.1	4.1	92	H cell	115
Co7	590	−0.63	$KHCO_3$ 0.1 M	14.7	4.1	98	H cell	116
Co6[a]	440	−0.61	$NaHCO_3$ 0.5 M	18	1.4	90	H cell	64
Co20	8.5	−0.58	$NaHCO_3$ 0.5 M	19.9	12	99	H cell	24
Co26	—	−0.60	$NaHCO_3$ 0.5 M	24.7	1.9	98	H cell	121
Co9	1.5	−0.92	KOH 1 M	165	1.67	94	Flow cell	115
Co6	7	2.52 V (cell voltage)	KOH 1 M	176	0.24	88	Gas diffusion cell	118
Fe4	1.3	−0.6	KOH 1 M	152	0.57	98.1	Flow cell	119

[a] Polymerized at carbon nanotubes.

carbon supports are well adapted since they combine good mass transport properties and electronic conduction. They are often used in combination with a binder such as Nafion. Catalysts loading are typically in the range of a few to hundreds of nmol cm^{-2}. However, large loadings may lead to stacking or aggregation which would hinder mass transport of the reactant and product and electron transfer processes. Assessing the catalytically active surface concentration is difficult since only a fraction of the immobilized molecules usually performs catalysis. This has led to underestimation of TON and TOF values. In favorable cases, a non-catalytic reversible redox wave allows quantifying the electrochemically active catalyst concentration. Attachment strategies at carbon materials (carbon particles, nanotubes, graphene derived materials) typically include non-covalent interactions (π–π, electrostatic), covalent bonding or periodic immobilization (metal–organic frameworks, porous organic polymers). Due to their high activity and ease to be immobilized at various electrode surfaces, porphyrins and phthalocyanines, notably Co and Fe ones, have been used as supported molecular catalysts to catalyze CO_2 reduction in water. An early report was related to **Co6** phthalocyanine.[113] Results show near perfect selectivity for CO production in a gas diffusion set-up, with the molecular catalyst being immobilized on a porous electrode and current density of 22 mA cm^{-2} at −1.5 *vs.* SCE. Soon after, it was shown that Ni phthalocyanine **Ni15** may be as efficient as the cobalt one with 100% selectivity for CO production in a potential range of −1.0 V to −1.75 V *vs.* SCE.[114] Interest in supported molecular systems re-emerged recently with Co,[82] Ni[117] and Fe[120] porphyrin systems. **Fe5** mixed with carbon powder and immobilized at a carbon electrode showed stable activity for up to 30 h under neutral aqueous conditions at 1 mA cm^{-2} with a selectivity of up to 98% for CO at a potential of −0.96 V *vs.* SCE, working at an energy efficiency of 50%. The same catalyst was then used in a flow-cell under neutral conditions,[119] and a current density of up to 50 mA cm^{-2} was obtained with a near 100% CO selectivity. A protoporphyrin (**Co26**) covalently attached to carbon nanotubes by a reaction at the cobalt center has led to a high current density for CO (j = 24.7 mA cm^{-2}) at a low overpotential of 490 mV and a TOF of 1.9 s^{-1} (pH 7.3, FE 98.3%).[121]

Co phthalocyanines have also been the focus of a lot of interest recently under supported conditions.[12,64,116] Those systems may reach partial current density for CO up to 18 mA cm^{-2} in a H-cell, with faradaic efficiency in the range of 90–98% and potentials between −0.61 and −0.68 *vs.* RHE, which corresponds to overpotentials of 475 and 540 mV respectively (Table 2).[116] Quaterpyridine **Co20** was immobilized at the surface of multi-walled carbon nanotubes and proved to be an excellent CO_2-to-CO catalyst in water at pH 7.3, with 100% FE and a partial current density of 19.9 mA cm^{-2} at an overpotential of 440 mV (E = −0.58 V *vs.* RHE).[24] The performances of some supported catalysts are summarized in Table 2, although comparisons remain difficult due to the variety of set-ups and differences in catalytic film manufacture. Thorough mechanistic studies are necessary for these supported molecular catalysts as well as rigorous benchmark studies. As briefly alluded to in this section, these highly active Co and Fe catalysts for CO production in water have now been included into flow cells and assembled at gas diffusion electrodes (Table 2, entries 7–9). Full details and description of these systems are provided in the next section.

2. Molecular catalysts in electrochemical reactors

Electrochemical reactors employing gas diffusing electrodes have been developed to improve CO_2 electrocatalytic reduction with the goal of reaching high efficiency and high durability at current densities in the range of several hundreds of mA cm^{-2} (geometric surface electrode area) which is not possible in typical H-cells due to mass transport limitations.[122–126] Until recently, such performances were deemed to be only possible with solid state materials, precious metals such as Au and Ag being the two most investigated metals.[125,127–129] For example, silver sputtered at PTFE or an anion exchange membrane onto a GDE can provide CO with about 90% FE and at a current density of about 200 mA cm^{-2}. Using non-precious Ni single atoms at porous carbon membranes recently led to an impressive partial current density of 308 mA cm^{-2} for CO production.[130] The progress achieved for the electrochemical catalytic reduction of CO_2 with molecular catalysts have stimulated the insertion of these catalysts into lab-scale cell devices, in particular flow cells. Some examples for CO_2-to-CO conversion have shown promising results, especially in terms of current densities and selectivity, opening new perspectives toward up-scaling and development of industrial devices. It is to be noted that pioneering studies have been done in the late 1980s and 1990s, in particular with the use of phthalocyanines and porphyrins (M = Co, Fe, Ni, Mn, Cu)

deposited on a GDE.[113,131,132] It led to partial current densities for CO production in water solutions in the range of a few tens of mA cm^{-2}, with values up to 55 mA cm^{-2} for Fe tetraphenyl porphyrin in 0.5 M $KHCO_3$ solution[132] and 53 mA cm^{-2} with Co phthalocyanine.[131] Another interesting facet of using a GDE is the possibility of performing mechanistic studies with molecular catalysts at surfaces, without being limited by mass transport of the reactant. Such studies, which are extremely tedious as with solid state catalysts, are still in their infancy but they are a key to improve performances.

Recently, a micro-flow electrochemical cell including a GDE at which a modified phthalocyanine (**Co7**) mixed with multi-walled carbon nanotubes was deposited led to a maximum CO current density of 82 mA cm^{-2} (with *ca.* 60% FE for CO, full cell voltage 2.3 V) in 1 M KOH flowing electrolyte.[133] Long term electrolysis (10 h) at 40 mA cm^{-2} could be sustained at about 90% CO selectivity. CO_2 reduction selectivity and activity for CO production can be further improved even with commercially available compounds such as cobalt phthalocyanine **Co6**.

This catalyst, when mixed with porous carbon black and deposited at an electrode surface can mediate CO_2-to-CO conversion in a zero-gap membrane flow reactor with selectivities >95% at 150 mA cm^{-2}.[118] As shown in Fig. 12, comparison with other molecular catalyst based systems (in H-cell or flow cell) illustrates the high performances of **Co6** in terms of FE_{CO} and current density. It closely matches performances obtained with the most active noble metal-based, such as Au[129] and Ag[127] nanocatalysts both for cell voltage, energy efficiency and current density.

Tuning the ligand structure is a powerful approach to improve the activity of molecular catalysts, through electronic, steric and second sphere substituent effects, as already described in this review. Following this strategy, introducing a trimethylammonium group and three *tert*-butyl groups onto cobalt phthalocyanine (**Co9**) led to high activity toward CO_2-to-CO conversion in water over a broad pH range (from 4 to 14).[115] In that case, a flow cell electrolyzer operating under basic conditions was developed. Typical CO production with *ca.* 95% selectivity and good stability was obtained, with a maximum partial current density of 165 mA cm^{-2} (at an overpotential of 810 mV). Following a similar strategy for catalyst optimization, modified tetraphenyl iron porphyrin **Fe4** was shown to achieve fast and selective electrocatalytic CO_2 conversion to CO in a flow cell.[119] The catalyst was mixed with carbon black and deposited at a carbon paper electrode (GDE). A current density for CO production as high as 152 mA cm^{-2} (>98% selectivity) was obtained at 470 mV overpotential in a basic solution (pH 14). Under the same conditions, j_{CO} = 27 mA cm^{-2} was maintained for 24 h at only 50 mV overpotential and with close to perfect 99.7% selectivity. A maximum current density of 83.7 mA cm^{-2} was obtained at pH 7.3, with selectivity close to 98%. Very recently, a nickel catalyst (**Ni1**) was inserted in a continuous non-aqueous flow cell, giving CO with a selectivity close to 80% and a maximum current density of 50 mA cm^{-2} in CH_3CN with NH_4^+ as a co-substrate.[134] Examples described above illustrate the rich potentiality of using highly active catalysts into an electrolyzer comprising a GDE. As already mentioned, various set-ups may be used. In flow cells, a liquid electrolyte circulates on both sides of the membrane separator, which is usually a polymer electrolyte membrane type such as a cation-exchange membrane (CEM), anion-exchange membrane (AEM) and bipolar membrane (BPM). The designed cell architecture used for catalysts **Co9** and **Fe4** consists of a sandwich of flow frames, electrodes, gaskets and an AEM membrane as illustrated in Fig. 13a and b. The anode and cathode are assembled on both sides of the membrane. The CO_2 gas flow is delivered from the back side of the cathodic compartment and flows through the GDE, while the catholyte solution is circulated in between the GDE and the anion exchange membrane (AEM). On the other side of the AEM, an anolyte electrolyte circulates between the AEM and the anode. Fig. 13c schematically illustrates the zero-gap membrane reactor (no electrolyte is flowing in the cathodic compartment) where the catalyst is directly sandwiched between the GDE and the membrane (MEA assembly type).

There is still a lot of work to be conducted before molecular catalysts may be used in flow cell CO_2 electrolyzers at an industrial scale. Long term stability remains an issue (as it is currently the case with solid catalysts too), which calls for vigorous efforts to decipher the catalytic mechanisms involving molecular catalysts inserted into thin films deposited at electrode surfaces, and to better identify possible degradation

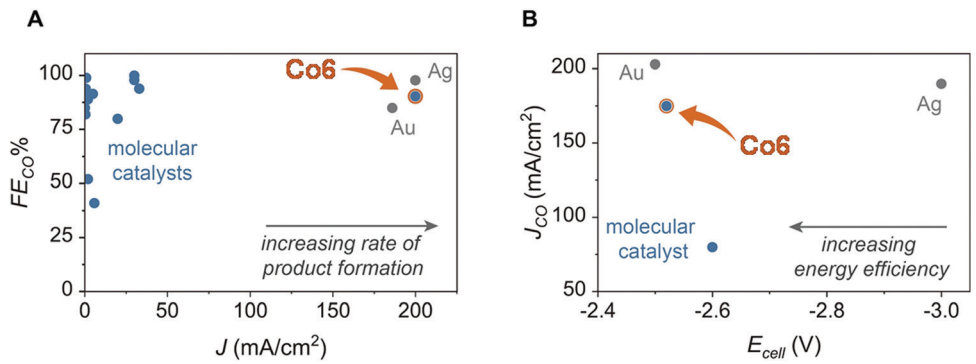

Fig. 12 Comparison of selectivity (A) and activity (B, partial current density) for CO production with **Co6** inserted in a zero-gap membrane flow reactor and previous molecular and heterogeneous CO_2 reduction electrocatalysts (adapted from ref. 118 with permission from AAAS, copyright 2019).

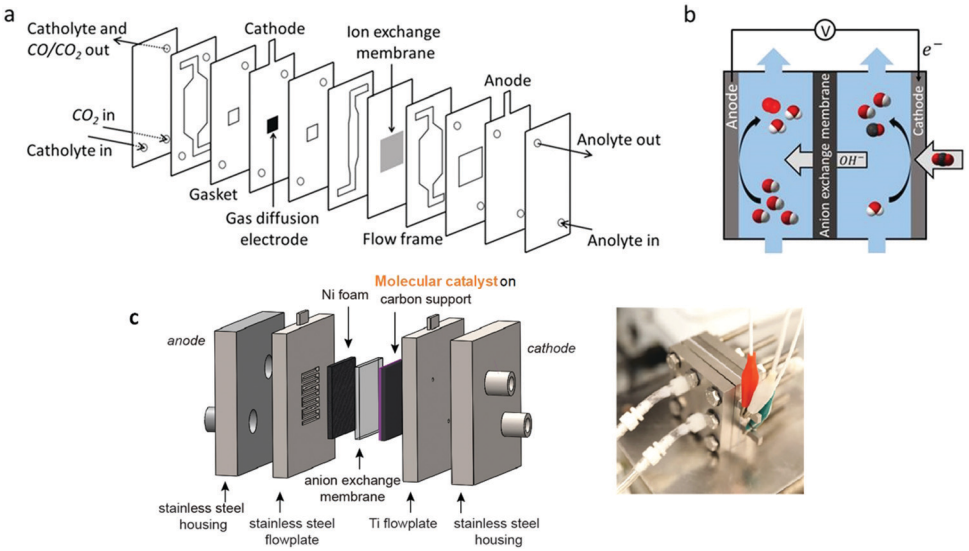

Fig. 13 (a) Scheme of the CO_2 flow cell electrolyzer: cross-sectional view of the cell elements (adapted from ref. 115), (b) scheme of the experimental setup operating under alkaline conditions with catalysts **Co8** and **Fe4** (adapted from ref. 119 with permission from Wiley, copyright 2020). (c) Scheme of the zero-gap membrane reactor used for CO_2 electroreduction of **Co6** (left; the MEA is made up of the cathode and anode GDEs on either side of the AEM); image of the cell (right). Adapted from ref. 118, with permission from AAAS, Copyright 2019.

pathways for the catalysts. Theoretical tools have been recently devised and should be used.[26,28] The understanding of local environment effects is also of prime importance. Such effects may manifest for example by high local pH due to fast proton consumption and may result in crystal growth at the GDE[118] and/or membrane cross-over of ionic species during long term operation. Beneficial effects such as temperature and electrolyte cation optimization have also been identified. For example, it was observed for iron catalyst **Fe4** that reaction kinetics could be boosted upon changing the temperature.[119] Raising the temperature from 24 °C to 40 °C led to a 300 mV overpotential decrease at 50 mA cm^{-2} current density (pH ~ 7, 0.5 M $NaHCO_3$). Remarkably, it was also shown with the same iron molecular catalyst, as previously observed with solid electrocatalysts,[135] that larger size cations could lead to better performance. At a fixed current density of 50 mA cm^{-2}, a significant lowering of the overpotential (390 mV) was observed upon increasing cation size going from Na^+ to K^+ and finally Cs^+. Such an effect may be ascribed to higher surface charge density and consequently increased affinity between CO_2 and the cathode surface.[135] Finally, optimization of the cell architecture (optimization of the membrane, of the catalytic film formulation, decrease of the cell resistance, *etc.*) is an additional challenge toward real devices. Further studies will certainly soon burgeon using related catalysts and approaches.

3. Light-driven and assisted approaches

3.1 Introduction to light-driven reduction of CO_2. Inspired by natural photosynthesis which achieves conversion of solar energy into chemical energy (chemical bonds in carbohydrates), many studies have been and are currently devoted to the direct conversion of solar energy into chemical fuels *via* photo- or photoelectro-catalysis, giving birth to artificial photosynthesis and solar fuels fields. Current works are focused on water splitting, CO_2 reduction, nitrogen fixation and oxygen reduction to produce hydrogen peroxide or water. An artificial photosynthesis system requires the combination and synchronization in time and space of four steps: photon absorption (through semi-conductors or photosensitizers), charge separation, transfer of electrons from the photo-absorber to the catalytic center and catalytic reaction transforming the substrate (possibly associated with a co-substrate such as a protonating agent) into the product or a mix of products.

Photocatalytic molecular systems for CO_2 reduction comprise three components, *i.e.* a catalyst (CAT), a redox photosensitizer (PS) and a sacrificial electron donor (SD). The metal complex serves as a catalyst capable of accumulating multiple electrons needed to reduce CO_2. Light-driven electron transfers can be classified as oxidative (Scheme 4a) or reductive quenching (Scheme 4b) according to the quenching reaction of the photosensitizer. In the first case, after excitation (Scheme 4a, step (1)), the lowest excited state of the PS (PS*) is a strong reductant and gives an electron to the electron acceptor (EA, being the CAT or an electron mediator). Emission of PS* (Scheme 4a, step (2)) is

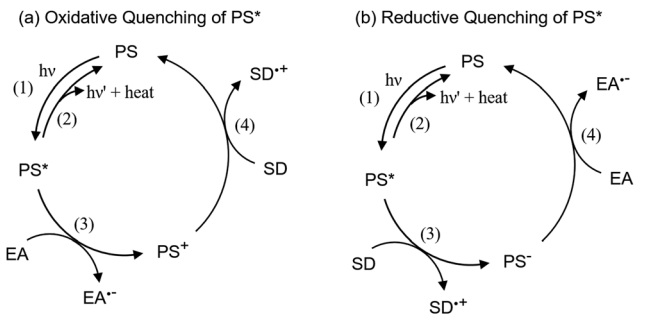

Scheme 4 Photosensitizer (PS) emission quenching pathways. EA: electron acceptor (catalyst or electron mediator), SD: sacrificial electron donor.

oxidatively quenched to give rise to the corresponding one electron-oxidized form PS^+ (Scheme 4a, step (3)). When the standard redox potential of $SD^{\bullet+}/SD$ is more negative than that of PS^+/PS, one electron can be donated to PS^+ (Scheme 4a, step (4)) to recover PS. Alternative possibility involves the reductive quenching of PS* (Scheme 4b). In this case, PS* accepts an electron directly from SD (Scheme 4b, step (3)). The one-electron-reduced form PS^- is thus produced. PS is regenerated through electron transfer from PS^- to EA (Scheme 4b, step (4)). Favorable conditions for oxidative quenching include long lifetime and high reducing power of PS* as well as high concentration of EA because electron transfer between PS* (PS^-) and EA is a bimolecular reaction.

Back electron transfer (BET) is a drawback that may lower, sometimes dramatically, the reaction quantum yield. For example, in the case of oxidative quenching of PS* (Scheme 4a), the reduced acceptor $EA^{\bullet-}$ may quickly transfer back an electron to the oxidized sensitizer (PS^+) since the reaction is endowed with a large driving force. Large concentration of donor (SD) may help in fighting BET.

Besides back electron transfer, many factors can affect the product yield, including light intensity, irradiation volume, concentration of CO_2, photocatalysts and SD, as well as standard redox potential values of the photosensitizer and the sacrificial donor. Quantum yield (QY) and turnover number (TON) are typically employed to evaluate CO_2 reduction efficiency. Quantum yield is a crucial parameter for assessing the performance of a photocatalyst or photocatalytic system. The internal quantum yield (IQY) and apparent quantum yield (AQY) are defined by eqn (11) and (12), respectively. IQY is calculated as the ratio of the mole amount of product multiplied by the number of electrons necessary for the product formation over the mole amount of absorbed photons, as shown in eqn (11), while AQY is calculated relatively to the number of incident protons (eqn 12).[136] TON is defined, as under electrochemical conditions, by the ratio between the mole amount of product and the mole amount of catalyst once the reaction has stopped. Care should be taken when comparing data between studies since catalyst concentrations may vary in between a few tens of nM and a few hundreds of μM. In some cases, very high turnover numbers have been obtained but at very low concentration of catalyst (nM range), leading to small absolute quantities of CO_2 reduction products and overstatement regarding the catalytic performances.

$$\text{IQY}\ (\%) = \frac{\text{mol number of product} \times \text{number of electrons per product}}{\text{mol number of absorbed photons}} \times 100 \quad (11)$$

$$\text{AQY}\ (\%) = \frac{\text{mol number of product} \times \text{number of electrons per product}}{\text{mol number of incident photons}} \times 100 \quad (12)$$

When evaluating the catalytic efficiency, the number of active catalytic sites is thus a crucial parameter but is difficult to evaluate in the case of supported systems. It indeed depends on the catalyst loading but also on active site accessibility. A determination of the catalyst content in supported systems can be made by calculating the amount of catalyst used in the synthesis process. Control of the remaining catalyst left in solution after preparation (through UV-Vis spectroscopy for example) can help in refining the previous estimation. More precise quantification can be obtained by using inductively coupled plasma atomic emission spectroscopy (ICP-AES, after treatment of the material with a strong acid solution) and X-ray photoelectron spectroscopy (XPS). Possibly, if the material is conductive and can be deposited at an electrode, electrochemical methods can also be employed to quantify the number of electrochemically active sites.

3.2 Photoelectrochemical processes. A first approach consists in combining light excitation of a semi-conductive electrode to an electric bias to activate molecular catalysts. One drawback is that metal complexes may absorb light and decompose upon long time irradiation. UV-light should be filtered to avoid such photodegradation. And if a fraction of visible light is absorbed, even weakly, it will also lead to a significant decrease of the light to chemical energy conversion. Some molecular catalysts are also prone to photodecomposition under visible light which adds another hurdle when selecting a suitable catalyst. Despite these adverse drawbacks, strategies to overcome these issues, such as UV-light absorption by a photoanode positioned upstream or irradiation of the photocathode from the back of the device, have been explored.

Molecular catalysts may be implemented at photoelectrodes following three strategies as depicted in Scheme 5. Each one can be deployed in various configurations (with a grafted or freely diffusing catalyst, irradiation from the front or from the back of the electrode, addition of protective layers on the semiconductive material, *etc.*) and combination of several strategies in series can also be envisioned. For example, the p–n junction pictured in configuration b is usually protected from electrolyte corrosion by several layers with various doping and thickness that would in principle allow for optimizing the stability and the efficiency (*e.g.* charge transfer to the catalytic sites) of the device.[137] This buried junction could eventually be doubled or tripled.[138] In the following, we will not detail photoelectrode underlayer preparation.

Regarding CO_2 photoelectrochemical reduction with molecular catalysts, the three strategies a–c (Scheme 5) have been reported. Examples employing b–c type strategies are restricted to the last 10 years and early examples exclusively involved strategy a. The latter a was first reported in 1983, with the use of Ni and Co tetra-azamacrocyclic complexes (**Co23**, **Ni2**, **Ni8** and **Ni9**) in a CH_3CN/water (1 : 1, v : v) electrolyte at a p-Si electrode.[139] Upon photo-electrolysis at −1.00 V *vs.* SCE, which corresponds to a negative overpotential of 50 mV estimated from $E^0_{CO_2/CO}$ in acetonitrile/water (1 : 1, v : v) solvent,[140] catalyst **Ni2** showed a 64% FE for CO with H_2 as the only by-product for more than 24 h. However, the absence of reported current density does not allow assessing the rate and efficiency of

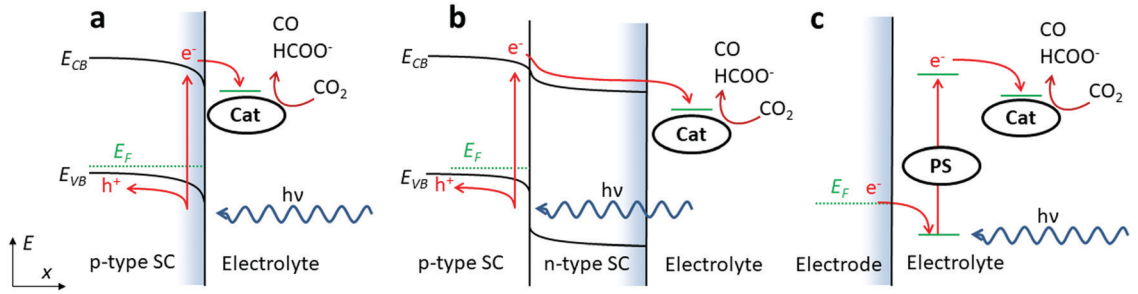

Scheme 5 Possible photoelectrode configurations including molecular catalysts. (a) Catalyst at a p-type photocathode, (b) catalyst at a p–n photocathode, and (c) association between a catalyst and a sensitizer (PS) at a dark electrode surface.

this process. The other three catalysts (**Co23**, **Ni8** and **Ni9**) were mentioned to be less selective and required more negative potentials.

Several reports followed in the subsequent years where p-Si but also p-GaP, p-GaAs,[141–143] p-CdTe[144] p-WSe_2[145] were used as semi-conductive electrodes associated with nickel cyclam (**Ni1**)[141–143] or phthalocyanines (MPc, with M being Co, Ni and Fe but also Zn, Mn, Cu and V)[144] as molecular catalysts. Interestingly, upon associating **Ni1** with p-GaAs, photoelectrolysis was performed in aqueous media (pH 4.5, 0.1 M $KClO_4$) for more than 15 hours with FE for CO slightly below 50% at a quite negative potential $E = -0.95$ *vs.* NHE and gave 4 TON for CO.[141] This low selectivity was attributed to catalysis of water reduction by p-GaAs itself. Replacement of this semiconductor by p-GaP enabled enhancement of CO faradaic efficiency up to 85% in a 0.1 M $NaClO_4$ aqueous solution and at a potential between −0.75 V and −0.2 V *vs.* NHE, although no turnover number was given and the photo-electrolysis duration time was also not specified.[143,146] Interestingly nickel cyclam **Ni1** could be employed without filtering the UV-light and catalytic activity was maintained for several hours. In terms of selectivity and activity, p-CdTe based electrodes coated with MPc were able to reach current density as high as 10 mA cm^{-2} in DMF (5% H_2O) although such a current density does not match with the reported transient data.[144] Selectivity for CO was high, close to 100% for CoPc, 92% for FePc and 77% for NiPc. Formate was systematically obtained with FE between 2 to 6%. At that time, only one other publication was using a precious complex, with $Re(CO)_3(bpy)Cl$ at p-Si and $pWSe_2$ electrodes, also showing good selectivity.[145]

The field remained almost unattended for about 20 years until Kubiak *et al.* published a $Re(CO)_3(bpy)Cl$ catalyst at a p-Si electrode,[147] attaining high selectivity for CO (up to 97%) at −1.35 V *vs.* Ag/AgCl (which corresponds to 500 mV overpotential relatively to $E^0_{CO_2/CO}$ in CH_3CN).[22] Large current density, up to 31 mA cm^{-2}, was reported under transient conditions (at a scan rate of 100 mV s^{-1}), but the steady-state current density over photo-electrolysis was not specified. Estimation of the latter from the mole amount of electrons (7×10^{-5}) passed for 3 hours at a 0.27 cm^2 electrode yields a current density close to 2.3 mA cm^{-2}. A few weeks later, Arai, Sato *et al.* published a study in which a ruthenium complex was used as a CO_2 reduction catalyst at a InP photoelectrode.[148] Contributions from various groups were then focused on precious metal complexes[149–152] or other transition metals such as manganese.[153] Concerning Fe and Co aza macrocycles, Fe porphyrins (**Fe1** and **Fe19**) have been associated with p-Si in acetonitrile, with 650 mV photovoltage that allowed catalytic activity at only −1.1 V *vs.* SCE bias (210 mV overpotential).[154] Under these conditions, 90% FE for CO was obtained, with a current density of 3 mA cm^{-2}. Cobalt tris[((2-pyridylmethyl)amine)Cl]Cl (**Co24**) was also used at a p-Si nanowire electrode in CH_3CN solution, but with a lower current density of 1 mA cm^{-2} and 69% FE for CO at −1.57 V *vs.* Fc^+/Fc, corresponding to a large 520 mV overpotential.[155] Recently, strategy a has been much less investigated, likely because of the instability of narrow bandgap semiconductors under irradiation and the fast conversion of the p-Si interface with electrolyte into SiO_2 with only traces of oxygen.[147,154,156,157] Such instability has also been noticed as a limiting factor for p-GaAs materials.[158] These drawbacks lead to a tedious experimental methodology for electrode preparation that is not compatible with technological upscale.[141,147]

Strategy b offers an answer to the instability of narrow bandgap semiconductors, by adding protective layers on top of the semi-conductive surface and forming at the same time a complete p–n junction. The first report for such an approach for CO_2 reduction with molecular catalyst is recent[137] and involved the use of copper oxide Cu_2O, known for its instability under irradiation,[156] as a light harvesting material with protective layers made of AZO (aluminum doped zinc oxide) and TiO_2. In this, the classical $Re(CO)_3(bpy)Cl$ catalyst was used, first in solution and then attached through phosphonate groups to the top TiO_2 oxide layer.[159] A current density as high as 2.5 mA cm^{-2} was obtained in chopped light experiments (light being turned on and off at short regular intervals in order to distinguish photocurrent from background dark current). Photoelectrolysis was performed for 1.5 h with FE for CO decreasing from 95% to 80%, at a very large overpotential (1000 mV, $E = -2.05$ V *vs.* Fc^+/Fc). This publication was followed by reports using precious metal complexes such as Ru complex grafted at a Fe_2O_3 cathode.[160] The first studies using Co, Ni and Fe aza macrocycles only appeared in 2019, with a phosphonated Co bis(terpyridine) catalyst (**Co25**) grafted onto a TiO_2 layer covering a p-Si cathode. At a bias potential of −1.0 V *vs.* Fc^+/Fc (negative overpotential of −200 mV),[140] CO_2 was catalytically reduced into CO in CH_3CN:water mixtures, with a low current

density of *ca.* 100 μA cm^{-2} and an optimal FE for CO of 48%.[161] The photocathode was also operated in water (pH 6.7, 0.1 M $KHCO_3$), producing a small amount of CO (9.5% FE, partial current density of *ca.* 29 μA cm^{-2}) but also $HCOO^-$ (13% FE, partial current density of *ca.* 40 μA cm^{-2}) at E = 0 V *vs.* RHE (−115 and +110 mV overpotential for CO and $HCOO^-$, respectively).

Strategy c was first reported in 2013 with a molecular Re catalyst[162] and was followed by several studies involving noble metal based catalysts and sensitizers.[163–167] This strategy has also been associated in series with strategy b. For example, a Ru–Re molecular dyad anchored at a $CuGaO_2$ photocathode through a phosphonate linkage allowed reaching 72 and 81% FE for CO at −0.3 and −0.1 V *vs.* Ag/AgCl respectively (overpotential of −400 to −600 mV respectively) under illumination with visible light (λ > 460 nm).[166] However current densities remained low, typically in the range of a few tens of μA cm^{-2}. More recently higher current densities were obtained for CO_2 conversion to formate (0.7 mA cm^{-2} at E = −0.25 V *vs.* RHE, pH 6.8), using a Ru sensitizer and a Ru catalyst assembled at a Si|GaN|NiO photocathode.[167] This approach is certainly worth being further investigated upon employing earth abundant metal complexes and cheap sensitizers, such as organic dyes (see Chart 4 for examples).

Considerations on relative energy levels between the semiconductor, photosensitizer, electron relays and catalyst are of major importance to better understand the different approaches. In strategy a, and for an ideal case, the energy at which the catalyst is reduced to the catalytically active species has to lie below the conduction band (CB) of the illuminated semiconductor.[157] Nevertheless, due to surface states that pin the Fermi level at the interface, the semi-conductor/electrolyte interface may rather be considered as a semi-conductor/metal/electrolyte interface so that the photovoltage is determined by the difference in work function between the semi-conductor and the surface state.[168] Consequently, photovoltages have been obtained even for catalysts with redox energy levels lying above the conduction band of the semi-conductor.[141] Such considerations do not apply for configuration c since the energy levels of the photosensitizer and the catalyst have to be adjusted to enable electron transfer from the former to the latter. But contrary to configuration a, excited electrons in the photosensitizer are not driven toward the catalyst by an internal electric field. It usually results in higher electron–hole recombination efficiency and it may explain the low current density typically reported with strategy c. A larger current density may be obtained by increasing the driving force between the photosensitizer and the catalyst, but at the expense of a reduced photovoltage.[167] In strategy b, a key factor is the energy difference between p- and n-type semiconductors which will define the maximum photovoltage similarly to a PV cell. Such a device, where the p–n junction is buried may be regarded as a photovoltaic cell in series with an electrochemical electrode.[169] Consequently, meaningful comparison could be made with other systems, for example when a (photo)cathode is coupled with a photoanode,[150,165,166,170] or when both the anode and the cathode are two sides of a multiple-junction cell[138] or either when the cathode includes both configurations b and c in series.[166,167]

In the cases of buried junctions, the interfacial layer could be conductive.[169] However, to enable the passage of light the use of such conductive layer is precluded and large band gap material with high electron conductivity are instead preferred. These layers also need to be stable under reduction and to allow for molecular functionalization. So far only TiO_2, which complies with these requirements, has been employed as a top-cathode layer. Nevertheless, this metal oxide is electrochemically active,[171,172] and FE for CO_2 reduction is significantly

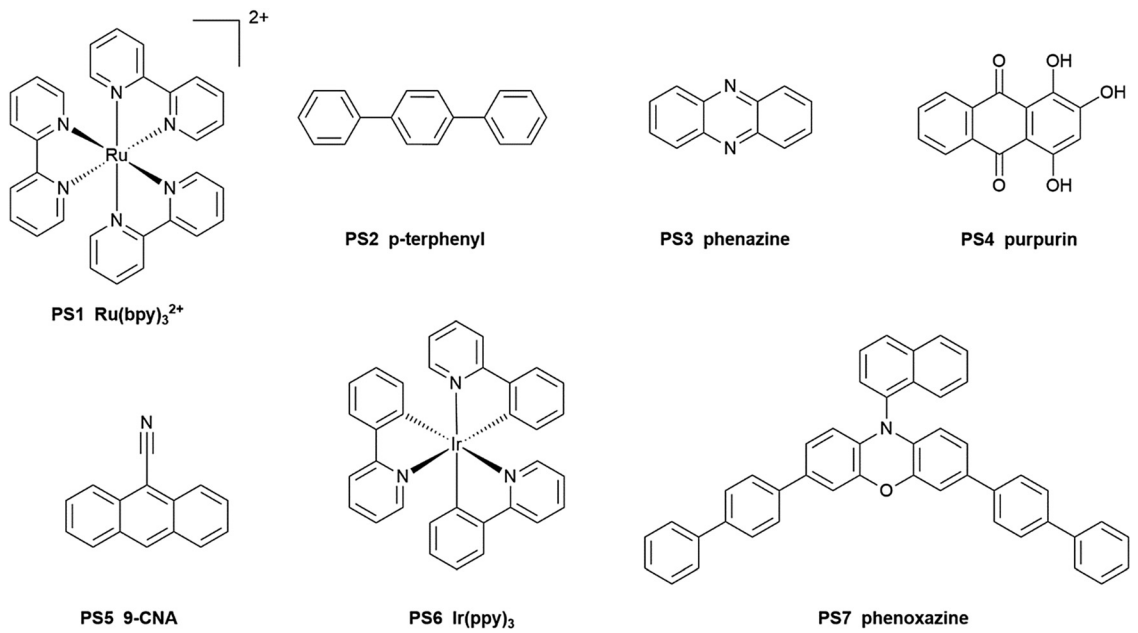

Chart 4 Typical molecular photosensitizers including metal-based (Ru, Ir) complexes and organic aromatic molecules.

below unity. Anchoring strategies also deserve special attention, especially regarding pH range stability.[6,173] Finally, a different strategy would be to cover the buried junction by a conductive and electrochemically inert material while back irradiating the photocathode.[169,174,175] Catalytic performances obtained with Co, Fe, and Ni aza macrocycle complexes are summarized in Table 4.

Ni, Co and Fe aza macrocycles have not been investigated under photoelectrochemical conditions as much as precious metal complexes, despite some early promising performances. CO_2 reduction products have been almost restricted to CO, in fewer cases to formate, while no example with more reduced compounds has yet been reported. Looking at the most recent investigations, it seems that strategies b–c are favored over a, and that aqueous electrolytes are systematically targeted despite CO_2 lower solubility. It should however be kept in mind that due to intrinsic limitations of photovoltaic devices under more concentrated sunlight, a current density of a few tens of mA cm^{-2} is likely to be an upper limit, so that a first priority should be put on stability of both the catalyst and the anchoring groups so as to get robust photocathodes. Fundamental challenges further include control of the proton environment at the catalytic sites and synchronization of the various steps of the process (charge separation and transport to the active sites, substrate and co-substrate diffusion, catalytic reaction). Finally, the future of photoelectrochemistry may not only rely on the performances of the catalyst, but will also depend on advances in photovoltaics and photoanodes.

3.3 Homogeneous molecular catalysts. A second approach consists in using fully homogeneous systems. Ni and Co cyclams (**Co10**, **Co11** and **Ni1**) were first used as catalysts for the visible-light driven CO_2 reduction by Tinnemans *et al.* in 1984. With $Ru(bpy)_3^{2+}$ (**PS1**) as a photosensitizer, CO was produced in an ascorbic acid containing aqueous solution with selectivity below 50% (Table 3, entries 1–4).[158,176] Ni^{II} cyclam (**Ni7**) was reported to be a moderately selective (57%) catalyst for CO under similar conditions, while its corresponding dimer (**$Ni_2$1**) showed 89% selectivity and a TON 6 times higher than the monomer (Table 3, entry 5).[176]

Co and Fe cyclams and polypyridines have shown interesting performances (Chart 1). This has led to mechanistic studies, notably with the identification of some reaction intermediates involved in the processes. In order to avoid the use of noble metal-based sensitizers, some light-absorbing aromatic organic molecules have also been used. The main catalytic product is CO with *p*-terphenyl (**PS2**, Chart 4 and Table 3, entries 6–13)[177,178] while it changes to formate with phenazine (**PS3**, Table 3, entry 14).[179] It was shown that phenazine is able to donate both electron and proton during catalysis. In that latter case, a Co–H hydride species, whose formation is enhanced by proton transfer from the sensitizer, was proposed to lead to formate upon CO_2 insertion. Note that in all these examples, catalytic activity is moderate with a low TON. Brunschwig, Fujita *et al.* have investigated several Co cyclams (**Co12–14**, **Co16**) to unveil possible intermediates under photocatalytic conditions.[180–182] Using a combination of transient absorption, Fourier-transform infrared spectroscopy (FTIR) and X-ray absorption near edge structure (XANES) analysis, a 5-coordinated CO_2 adduct intermediate $[Co^{III}L(CO_2^{2-})]^+$ (in which L stands for the cyclam type) was identified for the four studied cyclams. In this adduct, CO_2 is stabilized by the NH protons in the macrocycle ligand. A solvent molecule (CH_3CN in this case) can also coordinate the metal center to lead to a more stable six-coordinated intermediate $[(CH_3CN)Co^{III}L(CO_2^{2-})]^+$ by internal charge transfer from the metal center to the CO_2. The latter intermediate is then further reduced, with assistance of a proton or another CO_2 molecule, to afford CO.[54,183] Lau and Robert have reported two cobalt and iron complexes (**Co18**, **Fe22**) exhibiting different selectivity with CO and formate production respectively (Table 3, entries 15–17 and 18–20).[91,258] Such a difference was ascribed to slower C–O bond cleavage with the iron catalyst and concomitant higher basicity of the bound carbon atom, facilitating formate production at the expense of CO (no hydride was postulated on the reaction pathway). Recently a robust Fe-based quinquepyridine complex $[Fe(qnpy)(H_2O)_2]^{2+}$ (**Fe23**) that can reduce CO_2 to CO in aqueous acetonitrile solution was reported. Using $Ru(phen)_3Cl_2$ (phen = 1,10-phenanthroline) as the photosensitizer and BIH as the sacrificial reductant, CO was produced with a TON of 14 095 and a high selectivity of 98% under visible light irradiation (Table 3, entry 43).[184]

During the same period, Co porphyrin **Co1**[42] and its derivative **Co4**,[185] as well as the iron analogue **Fe11**[186] were found to be active CO_2 catalysts (Table 3, entries 21–23). Fe-porphyrin **Fe1** was first used for the photoreduction of CO_2 in 1997 (Table 3, entries 24 and 25).[187,188] In a DMF/TEA solution of **Fe1**, photoinduced ligand-to-metal charge transfer generated Fe^{II} from the initial Fe^{III} species. Fe^{II} was further converted to Fe^{I} upon light excitation and reductive quenching by TEA. Finally, the catalytically active species Fe^0 was proposed to be formed by disproportionation of two Fe^{I} species. Fe and Co phthalocyanines (**Fe14**, **Co8**, Table 3, entries 26–28)[189] and corroles (**Co22**, **Fe15**, **Fe16**, Table 3, entries 29–31)[190] were also investigated for photocatalytic reduction of CO_2. In the presence of *p*-terphenyl, TONs for CO of Fe and Co phthalocyanine complexes are comparable to those of porphyrin analogs, such as **Fe1** and **Co1**.[185]

Earth-abundant metal complexes were again put on the spotlight ten years later. A simple modified Fe tetraphenylporphyrin with OH groups in all *ortho*, *ortho′* positions of the four phenyl groups (**Fe2**, Table 3, entry 32) was investigated under photochemical conditions.[188] As demonstrated in electrochemistry,[110] the OH groups have a dual role, first providing an H-bonding pattern to stabilize the Fe–CO_2 adduct and then playing the role of proton relay to boost the C–O bond cleavage. In the absence of an external sensitizer, good selectivity was already obtained for CO (85%), significantly higher than with **Fe1**. Higher CO selectivity was further obtained, reaching 93% and 100%, upon using an organic sensitizer (**PS5**, 9-CNA) and a strongly reducing Ir complex (**PS6**, $Ir(ppy)_3^{3+}$) respectively (Table 3, entries 33 and 34).[191]

Self-sensitized CO_2 reduction was also investigated with **Fe4**, the porphyrin bearing four positively charged trimethylammonium groups at all para positions of each phenyl ring (Table 3, entry 35).[192] Both the catalyst efficiency and selectivity were increased as compared to **Fe2** under similar conditions.

Table 3 Photocatalytic CO_2 reduction using non-noble metal complexes

Entry	Catalyst	PS	SD	Solvent	Light source	Irrad. time	Product (TON)	Selectivity	Φ (%)	Ref.
1	**Co10** 0.08 mM	$[Ru(bpy)_3]^{2+}$ 0.5 mM	0.5/0.5 M H_2A/HA^-	H_2O (pH = 4)	Daylight lamp	18 h	CO (1.2)	<1% (CO)	—	158
2	**Co11** 0.08 mM	$[Ru(bpy)_3]^{2+}$ 0.5 mM	0.5/0.5 M H_2A/HA	H_2O (pH = 4)	Daylight lamp	18 h	CO (28.7)	71% (CO)	—	158
3	**Ni1** 2 mM	$[Ru(bpy)_3]^{2+}$ 0.5 mM	H_2A	H_2O (pH = 5)	Xe lamp 1000 W, λ = 440 nm	24 h	CO (0.1)	—	0.06% (CO) 0.003% ($HCOO^-$)	176
4	**Ni1** 0.1 mM	$[Ru(bpy)_3]^{2+}$ 0.5 mM	H_2A	H_2O (pH = 4)	Xe lamp 1000 W 340 < λ < 600 nm	8 h	CO (4.8)	12% (CO) 88% (H_2)	—	176
5	**$Ni_2$1** 0.25 mM	$[Ru(bpy)_3]^{2+}$ 0.5 mM	H_2A	H_2O (pH = 4)	Hg lamp 60 W, λ = 435 nm	1 h	CO (4.4)	89%	—	176
6	**Co12** 1.7 mM	*p*-Terphenyl 2 mM	TEOA	CH_3CN/CH_3OH (4 : 1 v : v)	Hg lamp 500 W high-pressure λ > 290 nm	1 h	CO (10.2) $HCOO^-$ (6.7)	—	15 (CO) 10 ($HCOO^-$) λ = 313 nm	177 and 178
7	**Co3** 1.7 mM	*p*-Terphenyl 2 mM	TEA	CH_3CN/CH_3OH (4 : 1 v : v)	Hg lamp 500 W high-pressure λ > 290 nm	1 h	CO (4.7) $HCOO^-$ (2.3)	60.5% (CO) 31.8% ($HCOO^-$)	—	177 and 178
8	**Co13** 1.7 mM	*p*-Terphenyl 2 mM	TEOA	CH_3CN/CH_3OH (4 : 1 v : v)	Hg lamp 500 W high-pressure λ > 290 nm	1 h	CO (5.3) $HCOO^-$ (3.5)	51.6% (CO) 34.4% ($HCOO^-$)	—	177 and 178
9	**Co14** 1.7 mM	*p*-Terphenyl 2 mM	TEOA	CH_3CN/CH_3OH (4 : 1 v : v)	Hg lamp 500 W high-pressure λ > 290 nm	1 h	CO (2.0) $HCOO^-$ (0.3)	52.4% (CO) 7.9% ($HCOO^-$)	—	177 and 178
10	**Co15** 1.7 mM	*p*-Terphenyl 2 mM	TEOA	CH_3CN/CH_3OH (4 : 1 v : v)	Hg lamp 500 W high-pressure λ > 290 nm	1 h	CO (4.9) $HCOO^-$ (2.5)	58.5% (CO) 30.4% ($HCOO^-$)	—	178
11	**Co11** 1.7 mM	*p*-Terphenyl 2 mM	TEOA	CH_3CN/CH_3OH (4 : 1 v : v)	Hg lamp 500 W high-pressure λ > 290 nm	1 h	CO (1.0)	44% (CO)	—	178
12	**Co16** 1.7 mM	*p*-Terphenyl 2 mM	TEOA	CH_3CN/CH_3OH (4 : 1 v : v)	Hg lamp 500 W high-pressure λ > 290 nm	1 h	CO (2.7) $HCOO^-$ (0.4)	30.3% (CO) 4.8% ($HCOO^-$)	—	178
13	**Co17** 1.7 mM	*p*-Terphenyl 2 mM	TEOA	CH_3CN/CH_3OH (4 : 1 v : v)	Hg lamp 500 W high-pressure λ > 290 nm	1 h	—	—	—	178
14	**Co12** 10 mM	Phenazine	TEA	CH_3CN/CH_3OH/ TEA (2 : 1 : 1, v : v : v)	Hg lamp 500 W high-pressure λ > 290 nm	1 h	CO (0.08) $HCOO^-$ (1.1)	92.2% ($HCOO^-$) 7.12% (CO)	—	179
15	**Co20** 0.005 mM	$[Ru(bpy)_3]^{2+}$ 0.3 mM	BIH	CH_3CN/0.5 M TEOA	LED λ = 460 nm	80 min	CO (2660)	98% (CO)	—	258
16	**Co20** 0.05 mM	$[Ru(bpy)_3]^{2+}$ 0.3 mM	BIH	CH_3CN/0.5 M TEOA	LED λ = 460 nm	80 min	CO (497) $HCOO^-$ (5) H_2 (3)	98% (CO)	2.8 (CO)	258
17	**Co20** 0.005 mM	Purpurin 2 mM	BIH	DMF	LED λ = 460 nm	11 h	CO (790) HCOOH (78) H_2 (11)	95% (CO)	0.8 (CO)	258
18	**Fe13** 0.005 mM	$[Ru(bpy)_3]^{2+}$ 0.2 mM	BIH	CH_3CN/TEOA (4 : 1 v : v)	LED λ = 460 nm	3 h	CO (3844) $HCOO^-$ (534) H_2 (118)	85% (CO)	1.45 (CO) first 45 min	258
19	**Fe13** 0.05 mM	$[Ru(bpy)_3]^{2+}$ 0.2 mM	BIH	CH_3CN/TEOA (4 : 1 v : v)	LED λ = 460 nm	3 h	CO (1879) $HCOO^-$ (48) H_2 (45)	97% (CO)	8.8 (CO)	258
20	**Fe13** 0.005 mM	Purpurin 0.02 mM	BIH	DMF	LED λ = 460 nm	12 h	CO (1365) HCOOH (115)	92% (CO)	1.1 (CO)	258
21	**Co1** 10 μM	—	TEA	CH_3CN	Xe lamp λ > 320 nm	20 h	$HCOO^-$/ CO (300)	—	—	42
22	**Co4** 0.05 mM	*p*-Terphenyl 3 mM	TEA	CH_3CN	Xe lamp λ > 300 nm	20 h	CO (62)	—	—	185
23	**Fe11** 0.034 mM	*p*-Terphenyl 3 mM	TEA	CH_3CN	Xe lamp 300 W, λ > 300 nm	20 h	CO (61.8)	—	—	186
24	**Fe1** 0.01 mM	—	TEA	DMF	Xe lamp 300 W	15 min	CO (70)	—	5	187
25	**Fe1** 0.01 mM	—	TEA	CH_3CN	VIS light (BG40-type optical filter)	10 h	CO (17)	8% (CO) in 1 h	—	188
26	**Fe14** 0.15 mM	—	TEA	CH_3CN	Xe lamp λ > 310 nm	6 h	CO (9)	—	—	189

Table 3 (*continued*)

Entry	Catalyst	PS	SD	Solvent	Light source	Irrad. time	Product (TON)	Selectivity	Φ (%)	Ref.
27	**Fe14** 0.15 mM	*p*-Terphenyl 3 mM	TEA	CH_3CN	Xe lamp $\lambda > 310$ nm	6 h	CO (90)	—	—	189
28	**Co8** 0.15 mM	*p*-Terphenyl 3 mM	TEA	CH_3CN	Xe lamp $\lambda > 310$ nm	6 h	CO (47.5)	—	—	189
29	**Co22** 0.042 mM	*p*-Terphenyl 3 mM	TEA	CH_3CN	Xe lamp $\lambda > 310$ nm	6 h	CO (86)	—	—	190
30	**Fe15** 0.048 mM	*p*-Terphenyl 3 mM	TEA	CH_3CN	Xe lamp $\lambda > 310$ nm	6 h	CO (43.8)	—	—	190
31	**Fe16** 0.045 mM	*p*-Terphenyl 3 mM	TEA	CH_3CN	Xe lamp $\lambda > 310$ nm	6 h	CO (51.1)	—	—	190
32	**Fe2** 0.01–0.05 mM	—	TEA	CH_3CN	VIS light BG40 filter	10 h	CO (28)	93% (CO) in 1 h	—	188
33	**Fe2** 2 μM	9-CNA 0.2 mM	TEA	CH_3CN	Xe lamp $\lambda > 420$ nm	45 h	CO (40–60)	100% (CO)	0.08 (CO)	191
34	**Fe2** 2 μM	*fac*-Ir(ppy)$_3$ 0.2 mM	TEA	CH_3CN	Xe lamp $\lambda > 420$ nm	55 h	CO (140)	93% (CO)	0.13 (CO)	191
35	**Fe4** 2 μM	—	BIH 20 mM	CH_3CN	Solar simulator $\lambda > 420$ nm	47 h	CO (63)	100% (CO)	—	192
36	**Fe4** 2 μM	Purpurin 2 mM	TEA	CH_3CN/H_2O (1 : 9 v : v), 0.1 M $NaHCO_3$	Solar simulator $\lambda > 420$ nm	47 h	CO (60), H2 (5)	95% (CO)	—	193
37	**Fe4** 2 μM	*fac*-Ir(ppy)$_3$ 0.2 mM	TEA	CH_3CN	Solar simulator $\lambda > 420$ nm	102 h	CO (367) CH_4 (79) H_2 (26)	17% (CO) 78% (CH_4) 5% (H_2)	—	231
38	**Fe4** 2 μM	*fac*-Ir(ppy)$_3$ 0.2 mM	TEA	CH_3CN/H_2O (3 : 7 v : v)	Solar simulator $\lambda > 420$ nm	47 h	CO (24) CH_4 (3) H_2 (5)	9% (CO) 75% (CH_4) 16% (H_2)	—	194
39	**Fe$_3$1** 3–6 μM	Ir(ppy)$_3$ 0.25 mM	TEOA	(*N*-Methyl-2-pyrrolidone) NMP	Hg lamp 2.5 W 400 < λ < 700 nm	5 h	CO (100)	50% (CO)	—	195
40	**Fe17** 5 μM	Ir(ppy)$_3$ 1.67 mM	TEOA	NMP/TEOA (5 : 1, v : v)	Hg lamp 2.5 W 400 < λ < 700 nm	1 h	CO (600)	50% (CO)	—	196
41	**Fe17** 1 μM	$[Cu(CH_3CN)_4]PF_6$ 5 μM	BIH	NMP/TEOA (5 : 1, v : v)	Hg lamp 1.5 W 400 < λ < 700 nm	5 h	CO (487)	99% (CO)	13	197
42	**Fe18** 0.05 mM	Cu–PS 0.25 mM	BIH	CH_3CN/TEOA (5 : 1 v : v)	Hg lamp λ = 435.8 nm	12 h	CO (273)	78% (CO)	6.7	198
43	**Fe23** 0.05 M	$Ru(phen)_3^{2+}$ 0.2 mM	BIH	CH_3CN/H_2O (1 : 1 v : v)	LED λ = 460 nm	68 h	CO (14 095)	98% (CO)	0.8 (in 24 h)	184
44	**Fe4** 10 μM	PS7 1 mM	TEA 0.1 M	DMF	Solar simulator $\lambda > 435$ nm	102 h	H_2 (23) CO (140) CH_4 (29)	12% (H_2) 73% (CO) 15% (CH_4)	—	232

Table 4 Summary of electrolysis performances involving Co, Fe, and Ni aza macrocycles at photoelectrodes

Catalyst	Concentration or loading	Electrode	Solvent	η (mV) overpotential	j (mA cm^{-2})	Time (h)	FE_{CO} (%)	Ref.
Ni2	180 mM	p-Si	$CH_3CN : H_2O$ (1 : 1; v : v)	−50	—	24	64	139
Ni1	0.52 mM	p-GaAs	H_2O	580	0.063	15	44	141
Ni1	6.75 mM	p-GaP	H_2O	380	≈0.250	15	85	143
Co6	—	p-CdTe	DMF : H_2O (95 : 5; v : v)	—	11.94	—	104	144
Ni15	—	p-CdTe	DMF : H_2O (95 : 5; v : v)	—	7.2	—	77	144
Fe14	—	p-CdTe	DMF : H_2O (95 : 5; v : v)	—	8	—	92	144
Fe1	0.2 mM	p-Si	CH_3CN : DMF (95 : 5; v : v)	210	3	6	92	154
Co24	1 mM	p-Si NWs	CH_3CN (1% H_2O)	520	1	5	69	155
Co25	45 nmol cm^{-2}	TiO_2/p-Si	$CH_3CN : H_2O$ (6 : 4; v : v)	−200	0.1	8	48	161

Fe4 could indeed achieve 100% selectivity using BIH as a sacrificial agent in CH_3CN. Moreover, the catalyst was able to perform CO_2 reduction in aqueous solutions (acetonitrile/water 1 : 9, v/v) with **PS4** as an organic photosensitizer, showing 95% selectivity (Table 3, entry 36).[193] Moreover, it has been found that **Fe4** can achieve CH_4 production in a CH_3CN solution containing up to 70% H_2O (Table 3, entry 38).[194]

Fe-carboxyl complexes are also active catalysts for CO_2 reduction to CO and formate. The commercially available $Fe_3(CO)_{12}$ (**Fe$_3$1**) was reported to reduce CO_2 in (*N*-methyl-2-pyrrolidone) NMP solvent, affording a 50% selectivity and TON *ca.* 100 for CO (Table 3, entry 39).[195] (Cyclopentadienone)iron-tricarbonyl ($Fe(cpd)(CO)_3$, **Fe17**) was reported by the same group and could accomplish CO_2 reduction with a TON of

600 in 1 hour (Table 3, entry 40).[196] Together with a Cu complex as a sensitizer and BIH as a sacrificial donor, the selectivity for CO could reach 99% with a high quantum yield of 13.3% (Table 3, entry 41).[197] Similarly, Ishitani *et al.* have reported an efficient photocatalytic system using a Fe complex as a catalyst in which the metal is chelated by two di-methyl 1,10-phenanthroline molecules ($Fe(dmp)_2(NCS)_2$, **Fe18**) and a Cu-based complex as PS that can convert CO_2 to CO under visible light with a TON of 273 and a quantum yield of 6.7% (Table 3, entry 42).[198]

Supramolecular assemblies (often called dyads, see Chart 5), formed by the covalent linkage of the catalyst and the photosensitizer units *via* bridging ligands, also showed interesting performances, by potentially facilitating energy/electron transfers between subunits. A first structure was reported in 1992 by Kimura *et al.* ($Ru(phen)_2$[phen-Ni(cyclam)]$(ClO_4)_4$, **RuNi1**). It included a $Ru(phen)_3^{2+}$ (phen = 1,10-phenanthroline) as a sensitizer unit and $[Ni(cyclam)]^{2+}$ as a catalyst but CO_2 reduction was not catalytic (TON < 1). Improved performance for CO production was obtained with a mixed system of $Ni(cyclam)^{2+}$ and $Ru(phen)_3^{2+}$ (Table 6, entry 4).[199] Aukauloo *et al.* reported the supramolecular assembly **RuNi2**, including a ruthenium trisbipyridyl-like unit covalently attached to a nickel cyclam *via* a triazole ring. **RuNi2** was able to convert CO_2 to CO in aqueous solution with ascorbate as a sacrificial donor under 450 nm illumination with a few TON (Table 6, entry 5).[200] Cobalt catalysts were also linked to a ruthenium photosensitizer for CO_2 reduction (**RuCo1** and **RuCo2**, Chart 5). After 29 hours of visible light irradiation in the mixed DMF : H_2O : triethanolamine (3 : 1 : 1) solution, the selectivity is improved (TON_{CO} = 3, $TON_{formate}$ = 31, TON_{H_2} = 1 for **RuCo1**, TON_{CO} = 5, $TON_{formate}$ = 34, TON_{H_2} = 1 for **RuCo2**, Table 6, entries 6 and 7). The yields for CO_2 were comparable with those obtained with $[Co\text{-tris(bpy)}]^{2+}$ simply mixed with $[Ru(bpy)_3]^{2+}$ (TON_{CO} = 9, $TON_{formate}$ = 28, TON_{H_2} = 16) (Table 6, entry 8), although the selectivity was slightly better.[201]

Performances could be significantly enhanced upon introducing conjugation in the linkage between the PS center and catalyst, and thus better electronic interactions between the

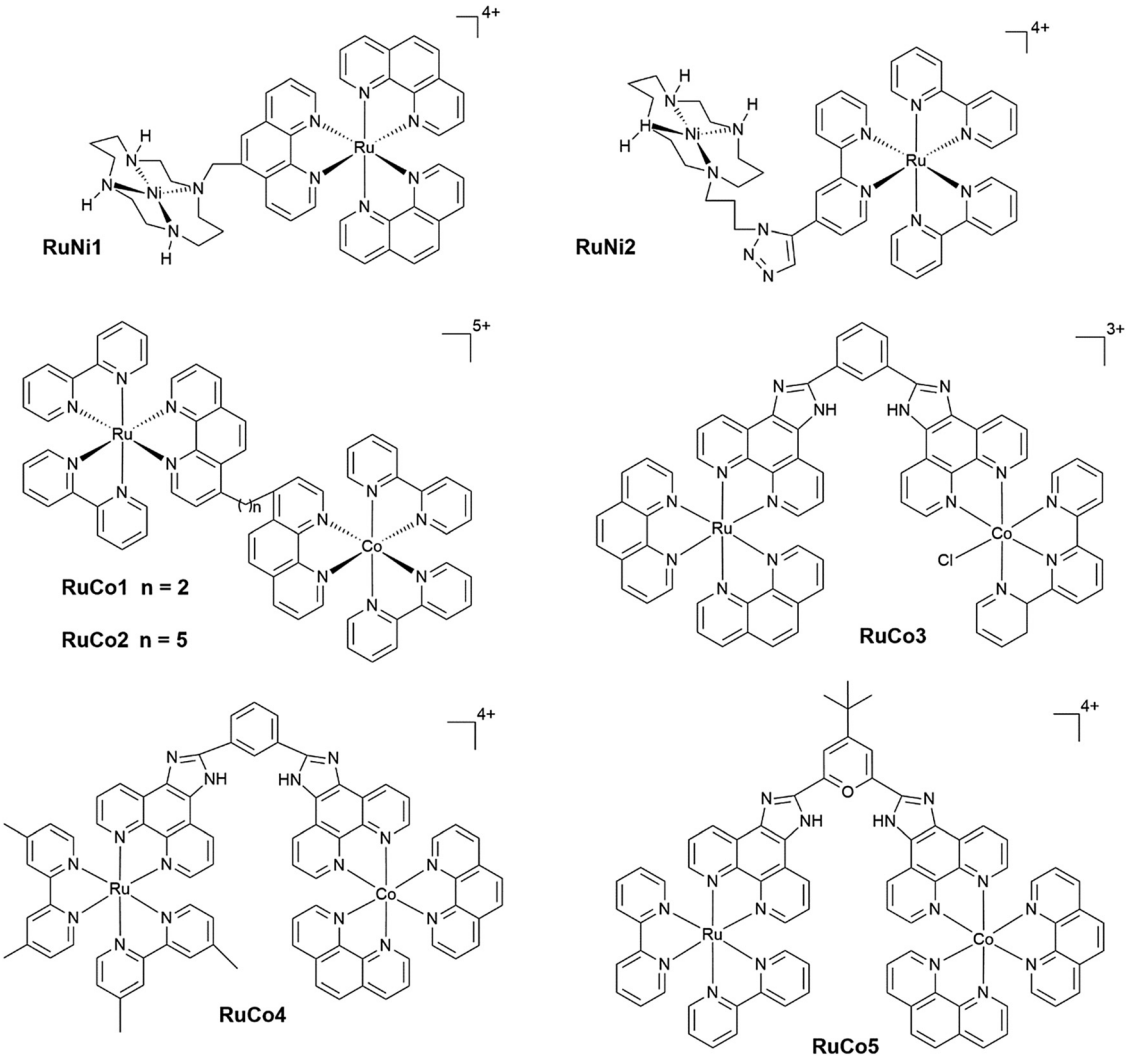

Chart 5 Molecular structures of sensitizer–catalyst molecular dyads.

subunits. Using this strategy, selectivity for CO_2 reduction and stability of the systems were improved. With the three catalysts **RuCo3**, **RuCo4**, **RuCo5**, TON values for CO production in the range of 50 were obtained with selectivity ranging from 67% to 87% in CH_3CN/TEOA (5 : 1 v : v) using BIH as a sacrificial donor under Xe lamp irradiation ($\lambda > 415$ nm, Table 6, entries 9–11).[202]

3.4 Supported molecular catalysts. A third, hybrid approach, consists in supporting catalysts at inorganic light-absorbing materials. Indeed, although many homogeneous light-stimulated catalytic systems have been investigated in detail with good catalytic performance for CO_2 reduction, the relatively poor durability is a limiting factor for practical applications.[203] Appending homogeneous photocatalysts at inorganic matrices has been developed to tackle some of these issues.[204] In this section, we discuss CO_2 light stimulated reduction with hybrid molecule–material heterogeneous systems. Molecular catalysts associated with electrodes are briefly presented in Section 1.4.

3.4.1 Inorganic bulk materials as scaffolds. Adsorbing or grafting molecules onto inorganic materials, such as silicon, zeolite and kaolin is the simplest approach. Hybrids consisting of Co^{III} cyclam (1,4,8,11-tetraaza-cyclotetradecane) complexes and silica SBA-15 *via* a refluxing and microwaving method have been prepared. By associating Co cyclam and SBA-15, higher catalytic activity (TON_{CO} = 160) and selectivity were obtained than free cyclam molecules (TON_{CO} = 142).[205] Further grafting of the Co-cyclam onto silica by a microwave-assisted process afforded a uniform distribution of the Co^{III} active sites in the silica mesopores, boosting the activity for CO production (TON_{CO} = 312) under similar conditions, and TON was increased over 500.[206] In a different strategy, a $[Mn(CO)_5Br]$ complex was attached onto bipyridyl-containing periodic mesoporous silica (bpy-PMO, Scheme 6), resulting in isolated Mn-carbonyl centers coordinated to the bipyridine functionalities of bpy-PMO. Employing $[Ru(bpy)_3]Cl_2$ as PS and BIH as SD, the hybrid can complete the photo-stimulated reduction of CO_2 with TONs of 484 and 239 for formate and CO respectively.[207] Such an approach may be extended to other earth-abundant metals.

Most metal complexes grafted on these inorganic porous matrices yet display lower activity than under homogeneous conditions due to limitations either in charge transfer steps or mass transport. Metal–organic frameworks (MOFs) have also attracted attention as a scaffold for developing high specific area hybrids able to host molecular catalysts. Significant progress has been made in constructing MOF-based systems for CO_2 reduction. A series of amine-functionalized Ti-, Fe-, and Zr-based MOFs showed good absorption in the visible domain and promising photocatalytic performance for CO_2 reduction.[208–210] A cobalt-based zeolitic imidazolate framework (Co-ZIF-9) led to a TON of 52.2 for CO in photoreduction of CO_2 employing TEOA as the sacrificial agent under visible light illumination.[211] Unfortunately, the weak coordination bonds in the framework commonly result in poor stability of the hybrid which may lead active species to leach out.[212] Overcoming these limitations may lead to new breakthrough in this rapidly emerging topic.

3.4.2 Particulate semi-conductors as supports. Semi-conductors including carbon-based materials (graphene, carbon nitride, carbon nanotube and their derivatives)[213–217] as well as inorganic metal sulfides (MoS_2, CdS, CdSe)[218,219] and metal oxides (TiO_2 and ZrO_2)[220–223] have been extensively used in constructing heterogeneous electro- and photocatalysts. In these catalytic systems, the semiconductor works as a photosensitizer, as co-catalyst and/or as an electronic channel.

Niu *et al.* have reported a thin film photocatalyst constructed by merging Co tetrahydroxyphenyl porphyrin (CoTHPP) and graphene. The hybrid film was suggested to reduce CO_2 to hydrocarbons under visible light, affording CH_4 and C_2H_2 through switching the electrons transfer direction from graphene–H_2O to graphene–CO_2, albeit no ^{13}C labelled experiments were shown to confirm the origin of the products.[224] By providing spatially and temporally separated centers for electrons and protons, the

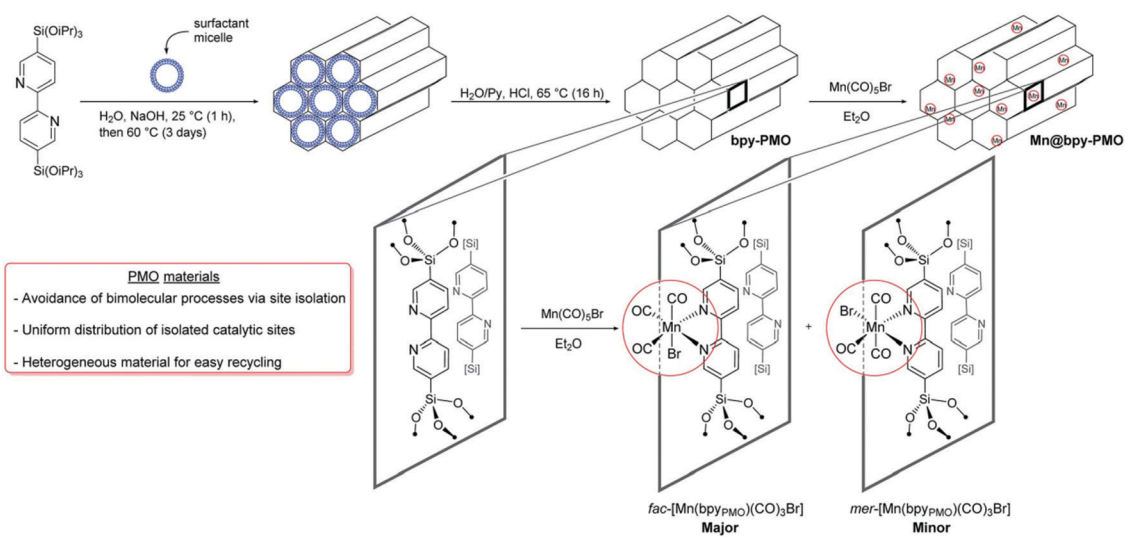

Scheme 6 Synthetic pathway to $[Mn(bpyPMO)(CO)_3Br]$. Reproduced from ref. 207 with permission from the Royal Society of Chemistry, copyright 2017.

iron tetra(4-carboxylphenyl) porphyrin chloride molecular catalyst (**Fe12**) assembled with a carbon nitride nanosheet reduced CO_2 into CO at a rate of 6.52 mmol g^{-1} in 6 h with a selectivity of 98%.[225] Mesoporous graphitic carbon nitride (mpg-C_3N_4) has also been employed as a redox photosensitizer in association with iron quaterpyridine (**Fe13**), thus forming a hybrid system fully made of abundant elements.[226] It was shown that under visible light irradiation ($\lambda \geq 400$ nm), in a mixed CH_3CN/triethanolamine (4 : 1, v : v) solvent, CO was obtained with 97% selectivity, reaching a TON of 155 after 17 h, and with an apparent quantum yield of *ca.* 4.2%. A polymeric cobalt phthalocyanine (**Co6**) catalyst (CoPPc) coupled with mesoporous carbon nitride was also developed.[216] Photocatalytic activity was observed to be highly dependent on the catalyst loading and also on irradiation conditions. In CH_3CN solution with TEOA as an electron donor, CO was obtained with TON_{CO} = 84 and a selectivity of 85% under full solar spectrum irradiation (>300 nm), whereas under visible light, TON_{CO} = 51 and selectivity decreased to 76% with identical catalyst loading. Recently, Co quaterpyridine (**Co20**) modified with an acid carboxylic group was covalently attached to the NH_2 pendent groups of a mesoporous C_3N_4 material through an amide linkage. It led to enhanced stability and selectivity for CO production, thanks to the robust connection and efficient charge transfer between the material and the catalyst.[227] In acetonitrile as a solvent with BIH as a sacrificial donor and phenol as a co-substrate, a 98% selectivity for CO was maintained over 4 days of irradiation with a TON of *ca.* 500.

In a similar approach, Reisner *et al.* also explored the association of molecular catalysts with semi-conducting materials. In a first example, they reported the immobilization of nickel terpyridines (**Ni14** and derivatives) previously employed as CO_2-to-CO electrocatalysts, adsorbed onto CdS quantum dots. These hybrids showed moderate photochemical activity under visible light in aqueous solutions for the reduction of CO_2 into CO with a selectivity of above 90% for the thiol derivative (terpyS).[218] They later reported the association of a phosphonic acid-functionalized Ni(cyclam) (**Ni1**) catalyst with ZnSe quantum dots.[228] The hybrid photocatalyst reduced CO_2 to CO (Ni-based TON_{CO} = 121, selectivity 8% after 20 h) in aqueous solution with ascorbic acid as the sacrificial agent. Interestingly, ZnSe surface modification with 2-(dimethylamino)ethanethiol (MEDA) resulted in the partial suppression of H_2 generation and thus enhanced CO production (Ni-based TON_{CO} = 283, selectivity 33%). Recently, Ni terpyridine (**Ni14**) was associated with halide perovskite nanocrystals ($CsPbBr_3$) and the light-driven CO_2 was studied in ethyl acetate as a solvent. Although no sacrificial donor was mentioned, CO was produced along with a small amount of methane, whose origin will likely be further investigated.[229] Weiss *et al.* employed $CuInS_2$/ZnS quantum dots in colloidal DMSO solution to photosensitize the catalytic conversion of CO_2 to CO with **Fe1** as a homogeneous catalyst under visible laser light (450 nm).[230] Efficient sensitization was ascribed to ultrafast (<200 fs) electron transfer between the quantum dot and **Fe1**, enabled by the formation of QD/catalyst complexes. The CO_2 reduction to CO was achieved with a selectivity for CO of 84% (16% for H_2) and a TON of *ca.* 50. Further studies led to combining the negatively charged $CuInS_2$/ZnS quantum dots with the positively charged **Fe4** thus creating a strong electrostatic assembly.[219] The photochemical reduction of CO_2 to CO was then achieved in water, under 450 nm irradiation, reaching a TON_{CO} of 450 after 30 h, with a selectivity of 99%.

These examples illustrate the remarkable potential of combining molecular catalysts to well defined semi-conductive nanomaterials and quantum dots. Controlling electronic interactions between the two sub-units and properly adjusting the catalyst choice may lead to high catalytic activity. Further development of complete Z-scheme systems, upon association of two sub-systems, one for CO_2 reduction and one for water oxidation, may soon lead to stimulating discoveries.

4. Bi-metallic systems with synergy between metals

If molecular catalysts mainly involve monometallic species, both natural and synthetic ones may also include two metals in close proximity, which may lead to a beneficial effect on CO2RR through synergy (cooperativity) between the metals. Ni–Fe carbon monoxide dehydrogenase (CODH) is a natural metalloenzyme that can reversibly convert CO_2 into CO.[237] CO_2 binds to both metal centers, with the C atom interacting with the Ni^I nucleophilic site and one of the O atoms bound to the Fe^{II} electrophilic site. Thus the two metals work synergistically to facilitate the cleavage of the C–O bond and achieve high selectivity. Many efforts have been made to mimic this sophisticated catalytic process. But regarding synthetic catalysts, only a few bimetallic centers have been shown to act in concert to reduce the CO_2 in molecular catalysts.

Solar-driven CO_2 reduction with dinuclear bimetallic complexes have attracted quite intensive research efforts. In 1996, Mochizulki *et al.* reported two dimerized Ni-cyclam complexes. Compared to monometallic macrocyclic complex **Ni7** (Table 6, entry 1),[176] the dimerized Ni-cyclam **$Ni_2$2** (Chart 6) shows enhanced efficiency and selectivity in CO_2 to CO conversion with a TON of 4.4 in aqueous solution at pH 4 (Table 6, entry 2). When the Ni-cyclam dimer **$Ni_2$1** (Chart 6) without methyl groups on the ligand was employed, the yield for CO was smaller than that for **$Ni_2$2**. Zhu *et al.* synthesized a dinuclear Co complex **Co21** (Chart 6) containing an oxygen atom at the *cis*-coordination site.[238] In CH_3CN/H_2O (5 : 1) solution with TEA as a sacrificial donor, **Co21** can achieve photocatalytic CO_2 reduction to both CO and formate under 450 nm irradiation, with TON values of 57 and 64 respectively (Table 6, entry 3). In that case however, the major product obtained was H_2 (TON 182). However, for all the above cases, geometry constraints likely prevent cooperativity effects between the metal atoms. One recent example related to photocatalytic reduction of CO_2 was obtained with a binuclear cobalt cryptate catalyst $[Co_2(OH)L](ClO_4)_3$ (L = $N[(CH_2)_2NHCH_2(m\text{-}C_6H_4)CH_2NH(CH_2)_2]_3N$, **$Co_2$2**, Chart 6). It affords CO with a TON of 16 896 and TOF of 0.47 s^{-1} under 450 nm LED light irradiation for 10 hours (Table 6, entry 12), while the corresponding monomer gave a TON_{CO} = 1600 with selectivity for CO of 85% in 10 hours.[239] Based on experimental data and DFT calculations, authors

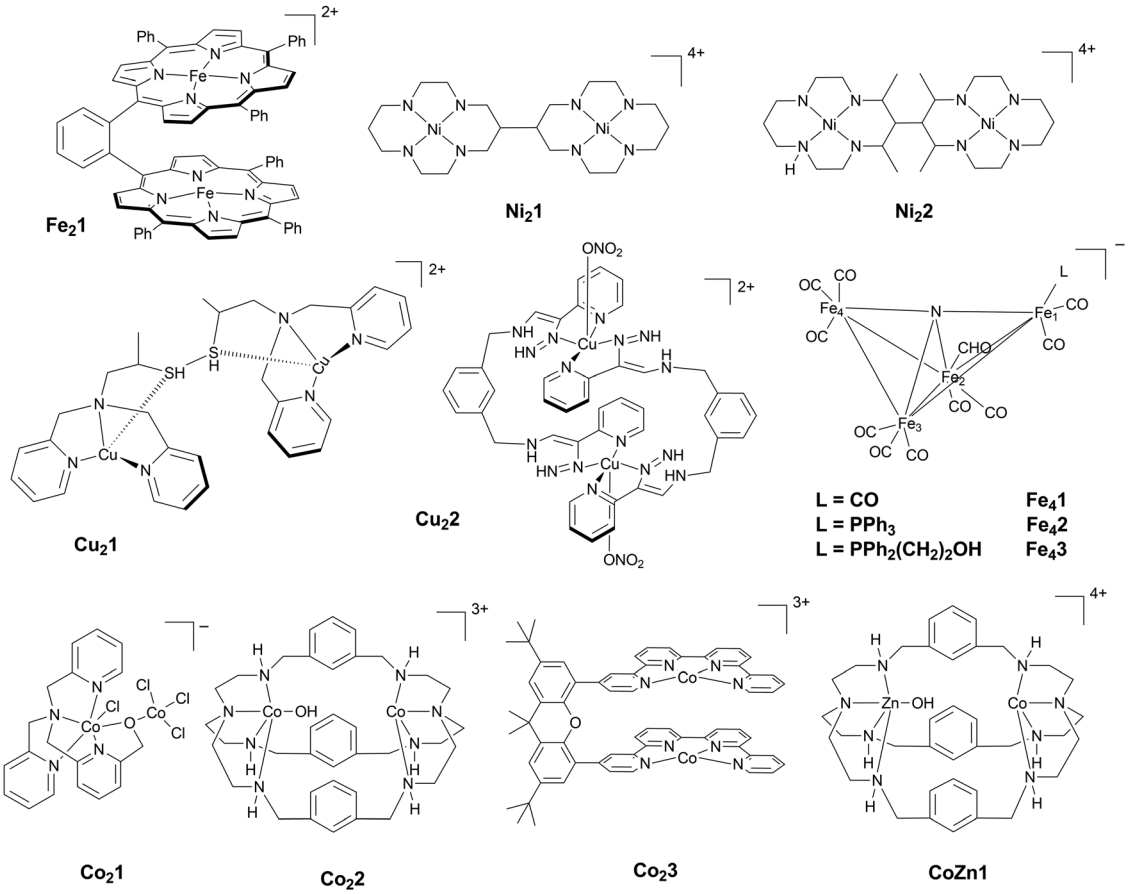

Chart 6 Molecular structures of various bi- and multi-metallic complexes.

concluded that during the photocatalytic process, the two cobalt atoms work synergistically, with the CO_2 molecule bound to the 2 Co atoms. After replacing one of the Co centers by Zn (**CoZn1**, Chart 6), the photocatalytic performance of the hetero bimetallic complex $[CoZn(OH)L](ClO_4)_3$ (**CoZn1**) was largely boosted to a TON of 65 000 and a TOF of 1.8 s^{-1} (Table 6, entry 13).[240] The improved catalytic efficiency can be ascribed to the enhanced dinuclear metal synergistic catalysis effect between Co^{II} and Zn^{II}. Zn^{II} plays the role of a Lewis acid center, helping C–O bond cleavage from an O=C–OH intermediate, thus significantly decreasing the activation barrier of the catalysis rate determining step.

Recently, a binuclear Co complex (**$Co_2$3**, Chart 6) bearing a bi-quaterpyridine ligand was shown to selectively reduce CO_2 to formate or CO under visible light.[40] Formate was produced selectively (maximum of 97%) in basic acetonitrile solution with a TON of up to 821 (Table 6, entry 14). Conversely, in the presence of a weak acid, CO_2 reduction affords CO with high selectivity (maximum of 99%) and a maximum TON of 829 (Table 6, entry 15). Spectro-electrochemistry (SEC) in the infrared region revealed an absorption band at 1635 cm^{-1} (Fig. 14), which was assigned to the formation of a stable adduct between CO_2 and the four-electron-reduced complex. Together with DFT calculations, these results indicate that CO_2 was sandwiched by the two cobalt atoms of the binuclear complex with the C atom from CO_2 binding to one Co atom, and one O atom interacting with the second Co atom. The catalytic process is controlled by the synergistic action of the 2 Co atoms, each playing a different, complementary role, and the selectivity can be oriented towards one or the other product by simply changing

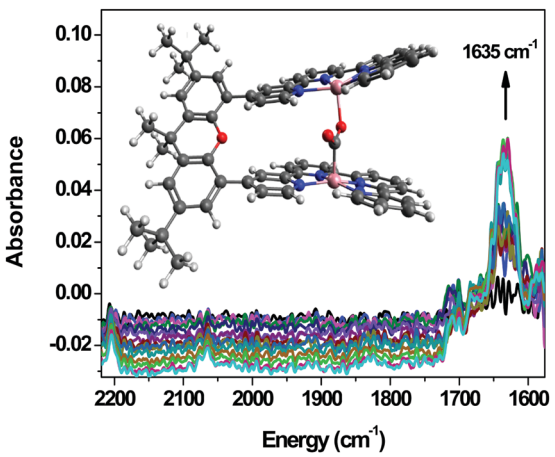

Fig. 14 Infrared spectro-electrochemistry data on a 1 mM solution of **$Co_2$3** in CH_3CN (0.1 M $^nBu_4NPF_6$, 0.5 M TEA) under CO_2 at potentials between −0.35 V and −0.85 V *vs.* Ag pseudo-reference. Inset: Calculated structure of the CO_2-reduced complex adduct identified at 1635 cm^{-1}. Adapted with permission from ref. 40. Copyright 2019, Springer Nature.

the acidity of the co-substrate to form different active intermediates. Upon protonation at the oxygen atom, CO is evolved while protonation at the C atom furnishes formate.

Going to electrochemical experiments, it was found that linking two **Ni1** monomers to form a $\mathbf{Ni_2}$**1** dimer can lead CO_2 to HCOOH conversion while the monomer complexes get CO. Potentiostatic polarization at −1.4 V *vs.* SCE in DMF containing 0.1 M H_2O led to the formation of formate with a good selectivity of 81% and FE of 68% after 5 hours (Table 5, entry 2).[101] In such a case however and due to geometry constraints there is likely no cooperation between metal sites, as noted previously in the case of light-driven processes. Such cooperation was triggered upon using copper-based catalysts. A remarkable example is given by binuclear copper complex $\mathbf{Cu_2}$**1** (Chart 6) possessing two tripodal tris(2-pyridylmethyl)amine ligands, able to reduce CO_2 into oxalate spontaneously. Upon CPE (7 h) at −0.03 V *vs.* NHE in CH_3CN containing $LiClO_4$ (to precipitate $Li_2C_2O_4$), oxalate was obtained with an FE of 96% and a TON of 6 (Table 5, entry 3).[234] The related complex $\mathbf{Cu_2}$**2** (Chart 6) gave similar results.[241] A Cu^ICu^I species was formed after reduction with sodium ascorbate in DMF, which further combined with two CO_2 molecules, resulting in $C_2O_4^{2-}$ generation (Table 5, entry 4). In these two cases, appropriate complex geometry and cooperativity between the two metal centers allowed for C–C bond formation.

Dinuclear Fe porphyrin molecule $\mathbf{Fe_2}$**1** with a Fe–Fe distance of 3.4–4.0 Å (Chart 6) was used to reduce CO_2 in DMF solution. It was shown that the CO_2 likely binds to the $Fe^{II}Fe^{II}$ species. Catalytic reduction is further triggered upon generating a Fe^IFe^0 species, at a potential *ca.* 100 mV more positive (∼−1.25 V *vs.* NHE in DMF) than for the monomeric **Fe1**. Upon adding 10% H_2O, the catalytic current was increased by a factor 6 as compared to the monomer catalyst under similar conditions. Ten hours of electrolysis at −1.55 V *vs.* Ag/AgCl yielded 88% FE for CO with H_2 as a by-product (Table 5, entry 1).[235] The conversion of CO_2 to formate has also been reported using an iron cluster $\mathbf{Fe_4}$**1**.[233] By using organic acids with different pK_a, the selectivity of the reaction to formate or hydrogen can be controlled, with strong acids favoring hydrogen generation. CV and IR-SEC allowed identifying $[Fe_4N(CO)_{12}]^{2-}$ as a catalytic species. Formate was produced in aqueous solution after electrolysis at −1.20 V *vs.* SCE with 98% selectivity, with a postulated bridging hydride between two Fe centers. This selectivity remained above 85% for pH between 5 and 13, and no CO was detected (Table 5, entry 5). Replacing one CO ligand with PPh_3 ($\mathbf{Fe_4}$**2**) led to lower selectivity with formate as the main product still (Table 5, entry 6). Finally, upon replacing one CO ligand with $PPh_2CH_2CH_2OH$ ($\mathbf{Fe_4}$**3**) almost no formate was obtained, with mainly H_2 as a product (Table 5, entry 7).[236,242]

Examples of synthetic homo or hetero bi(multi)-metallic molecular catalysts displaying increasing performances and/or specific reactivity, thanks to the synergistic effects exerted by the metal centers, remain scarce. It may however be an interesting pathway to precisely control the distance between the metals and the environment of each center so as to trigger new reactions, such as C–C bond coupling. Such a strategy is briefly described in the next section.

5. Beyond 2e⁻ reduction of CO_2

A growing number of articles have recently reported the reduction of CO_2 beyond two electrons using molecular electro- or photo-catalysts, starting directly from the gas or sometimes using CO or HCOOH as a reactant. Such stimulating studies may reveal completely new catalytic pathways. A first mandatory requirement is to track for the carbon source, which necessitates careful labeled studies. Looking at reports in this area indicates that many studies using metal-based complex catalysts for the (photo)electrochemical reduction of CO_2 to HCHO,[243] CH_3OH,[243–245] CH_4[131,132,246–249] or even C_2H_4[247,248] do not yet confirm their origin. It is an even more critical issue when molecular catalysts lead to stoichiometric or sub-stoichiometric processes.[244] Another hurdle lies in the fact that reporting on labeled experiments may lead to ambiguous conclusions regarding the origin of the catalysis products. An illustrative example is provided in Fig. 15. In this contribution, the authors have employed Co corroles deposited on carbon electrodes for the electrochemical reduction of CO_2 into CH_3OH in aqueous solution at pH 6.[250] They compared GC/MS data under $^{12}CO_2$ and $^{13}CO_2$ to assess the carbon source for the observed methanol. The fragmentation pattern for CH_3OH displayed *m*/*z* peaks shifted up by one unit under $^{13}CO_2$, as expected; however, the relative intensity of the various peaks drastically changed upon labeling the carbon dioxide, casting doubt on the conclusion that the methanol is issued from CO_2.

Table 5 Electrochemical CO_2 reduction using bi(multi)metallic complexes

Entry	Catalyst	Solvent	Electrode	Time	TON product	TOF product	Potential (V) overpotential η (V)	FE% product	Ref.
1	$\mathbf{Fe_2}$**1** 0.5 mM	DMF : H_2O (9 : 1)	GC	10 h	188 CO	—	−1.55 V *vs.* Ag/AgCl η = 0.66 V	88 CO	235
2	$\mathbf{Ni_2}$**1** 0.2 mM	DMF + 0.1 M H_2O	HME (Hg)	5 h	3.2 $HCOO^-$ 0.76 CO	—	−1.4 V *vs.* SCE	68 $HCOO^-$ 16 CO	101
3	$\mathbf{Cu_2}$**1** 0.5 mM	CH_3CN + $LiClO_4$	GC	7 h	6 $C_2O_4H_2$	—	0.03 V *vs.* NHE	96 $C_2O_4H_2$	234
4	$\mathbf{Cu_2}$**2** 0.3 mM	DMF + Na_2A	—	—	$C_2O_4^{2-}$	—	—	—	241
5	$\mathbf{Fe_4}$**1** 0.1 mM	H_2O (pH 7)	GC	50 min	28 $HCOO^-$	—	−1.20 V *vs.* SCE	98 $HCOO^-$	233
6	$\mathbf{Fe_4}$**2** 0.1 mM	CH_3CN : H_2O (95 : 5)	GC	50 min	5.4 $HCOO^-$ 3.3 H_2	—	−1.40 V *vs.* SCE	61 $HCOO^-$	236
7	$\mathbf{Fe_4}$**3** 0.1 mM	CH_3CN : H_2O (95 : 5)	GC	50 min	40 H_2	—	−1.40 V *vs.* SCE	<3 $HCOO^-$	236

Table 6 Photocatalytic CO_2 reduction using molecular dyads and bimetallic complexes

Entry	Cat.	PS	SD	Solvent	Light source	Irrad. time (h)	Product (TON)	Selectivity	Φ (%)	Ref.
1	**Ni7** 0.25 mM	$[Ru(bpy)_3]^{2+}$ 0.5 mM	H_2A	H_2O (pH = 4)	Hg lamp 460 W	1	CO (0.7)	—	—	176
2	**$Ni_2$2** 0.25 mM	$[Ru(bpy)_3]^{2+}$ 0.5 mM	H_2A	H_2O (pH = 4)	Hg lamp 460 W	1	CO (4.4)	94% CO	—	176
3	**Co21** 10 μM	*fac*-Ir(ppy)$_3$ 0.4 mM	TEA	CH_3CN/H_2O (5 : 1 v : v)	LED λ = 450 nm	60	CO (56.9) $HCOO^-$ (64.2) H_2 (181.6)	18.8% CO 21.2% $HCOO^-$ 60% H_2	—	238
4	**RuNi1** 0.5 mM	—	H_2A	H_2O (pH = 4)	Xe lamp 500 W $\lambda > 450$ nm	44	CO (<1)	72% CO	—	199
5	**RuNi2** 0.035 mM	—	H_2A	H_2O (pH = 6.5)	Xe lamp 500 W $\lambda > 450$ nm	60	CO (5.2) H_2 (2)	—	—	200
6	**RuCo1** 0.5 mM	—	TEOA	DMF : H_2O (3 : 1 v/v)	Xe lamp 500 W 400 < λ < 750 nm	29	CO (3) $HCOO^-$ (31) H_2 (1)	9.3% CO	—	201
7	**RuCo2** 0.5 mM	—	TEOA	DMF : H_2O (3 : 1 v : v)	Xe lamp 500 W 400 < λ < 750 nm	29	CO (5) $HCOO^-$ (34) H_2 (1)	12.7% CO	—	201
8	$[Co(bpy)_3]^{3+}$ 0.5 mM	$[Ru(bpy)_3]^{2+}$ 0.5 mM	TEOA	DMF : H_2O (3 : 1 v : v)	Xe lamp 500 W 400 < λ < 750 nm	29	CO (9) $HCOO^-$ (28) H_2 (16)	17% CO	—	201
9	**RuCo3** 0.1 mM	—	BIH	CH_3CN : TEOA (5 : 1 v : v)	Xe lamp 300 W $\lambda > 415$ nm	8	CO (51) H_2 (13)	79.6% CO	—	202
10	**RuCo4** 0.1 mM	—	BIH	CH_3CN : TEOA (5 : 1 v : v)	Xe lamp 300 W $\lambda > 415$ nm	8	CO (54) H_2 (8)	87.2% CO	—	202
11	**RuCo5** 0.1 mM	—	BIH	CH_3CN : TEOA (5 : 1 v : v)	Xe lamp 300 W $\lambda > 415$ nm	8	CO (70) H_2 (39)	64.3% CO	—	202
12	**$Co_2$2** 0.025 μM	$[Ru(phen)_3]^{2+}$ 0.4 mM	TEOA	CH_3CN : H_2O (4 : 1 v : v)	LED λ = 450 nm	10	CO (16 896)	98% CO	0.04% CO	239
13	**CoZn1** 0.025 μM	$[Ru(phen)_3]^{2+}$ 0.4 mM	TEOA	CH_3CN : H_2O (4 : 1 v : v)	LED λ = 450 nm	10	CO (65 000)	98% CO	0.15% CO	240
14	**$Co_2$3** 0.05 mM	$[Ru(phen)_3]^{2+}$ 0.2 mM	TEOA/ BIH	CH_3CN	LED λ = 460 nm	60	CO (221) $HCOO^-$ (821) H_2 (40)	20.4% CO 75.9% $HCOO^-$ 3.7% H_2	2.6% $HCOO^-$	40
15	**$Co_2$3** 0.05 mM	$[Ru(phen)_3]^{2+}$ 0.2 mM	PhOH/ BIH	CH_3CN	LED λ = 460 nm	1	CO (829) $HCOO^-$ (12) H_2 (22)	96% CO 1.5% $HCOO^-$ 2.5% H_2	—	40

Another example concerns the electrochemical reduction of CO_2 with cobalt protoporphyrin using on-line mass spectroscopy detection (OLEMS).[82] Labeled experiments are obscured by the presence of a mixture of products, solvent and electrolyte in the fragmentation pattern. Mass peak at *m*/*z* 17 could not be used to assess $^{13}CH_4$ formation from $^{13}CO_2$ as a reactant in water since the corresponding peak is dominated by the solvent signature. The authors instead used the peak at *m*/*z* 21 to track for the formation of $^{13}CD_4$ using $^{13}CO_2$ as a reactant in D_2O solvent. A blank experiment using $^{12}CO_2$ as a reactant for which no *m*/*z* = 21 signal would have been detected was however missing in the study, leaving the proof incomplete. In the following, we will focus our survey to cases where the source for products has been demonstrated without any ambiguity.

The first evidence of molecular electrochemical reduction of CO_2 beyond $2e^-$ was recently obtained using cobalt phthalocyanine **Co6** as a catalyst.[65] The complex was mixed with multi-walled carbon nanotubes and deposited as a thin film onto carbon paper. Upon electrochemical reduction of CO_2 and CO intermediate, in neutral or basic solutions, formaldehyde was formed and further reduced into methanol with a maximum 14% FE at pH 13 and a partial current density for methanol of 0.68 mA cm^{-2} (E = −0.64 V *vs.* RHE). The origin for methanol and the molecular nature of the catalysis were demonstrated by ^1H NMR and XANES analysis respectively. Interestingly in this catalytic process, no methane was formed. Shortly after this publication, highly dispersed **Co6** on MWCNTs has been shown to improve the catalytic activity of this catalyst for methanol, starting from CO_2,[251] with up to 44% FE at −0.94 V *vs.* RHE (pH 6.8). It should be noted that it was not proved in this work that methanol is formed from CO_2 reduction; however, similarity to the previous paper makes the case consistent. It may also be noted that reduction of CO_2 and CO into methanol involving molecular complexes, such Fe, Ni and Co porphyrins, has been reported by Ogura *et al.* in a series of papers published in the 1980s. However, these systems involve the use of Everitt's salt on a platinum electrode with the initial introduction of a primary alcohol and the molecular complex rather played the role of a co-catalyst.[252–254]

The eight-electron–eight-proton reduction of CO_2 to methane has rarely been achieved. Under photochemical conditions, some iron porphyrins (**Fe2** and **Fe4**, Table 3, entries 37, 38, 44) have been reported to convert CO_2 into CH_4 in acetonitrile or DMF solution containing an appropriate sensitizer and an amine as a sacrificial electron donor.[194,231,232] Both highly reducing Ir complex **PS6** and phenoxazine **PS7** were

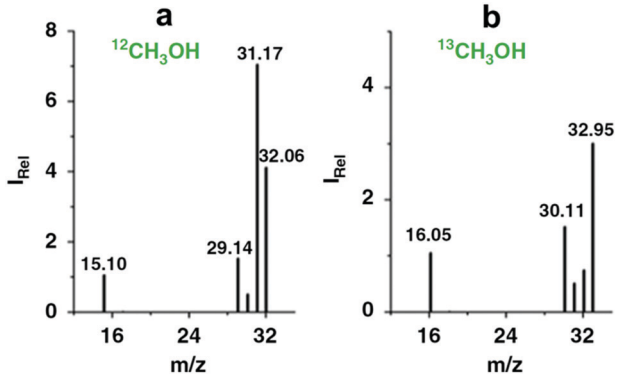

Fig. 15 GC/MS spectra and fragmentation pattern for the electrocatalyzed CO_2 conversion into CH_3OH. Graphs show the mass fragmentation pattern of CH_3OH (*m/z* 29 to 33) produced employing (a) $^{12}CO_2$ or (b) $^{13}CO_2$ as a reactant substrate. Reproduced with permission from ref. 250.

employed as sensitizers with visible light above 420 nm and 435 nm respectively. A TON of *ca.* 80 was typically obtained using CO_2 as a reactant with a selectivity for CH_4 around 17%. CO has been identified as a key intermediate in this process and could even be used as a starting reactant, leading to a maximum value of 160 for methane with a selectivity in the range of 82–85% (H_2 being the sole by-product) and an apparent quantum yield of up to 0.47%. A full mechanistic picture is still missing, although the bottleneck for the process is likely the reduction of the $Fe^{II}CO$ species formed upon reduction of CO_2 to CO.

Another approach to get such a highly reduced product is to use metal complexes as pre-catalysts for *in situ* electrodeposition of highly active material catalysts. For example, starting from **Fe13**, Fe nanoparticles (NPs) can be formed upon electrolysis in CH_3CN at a glassy carbon electrode in the presence of TEOA. These Fe NPs are able to achieve up to 2.6% FE for methane, being more active than particles electrodeposited from an iron salt or an iron based electrode.[255] In this study,

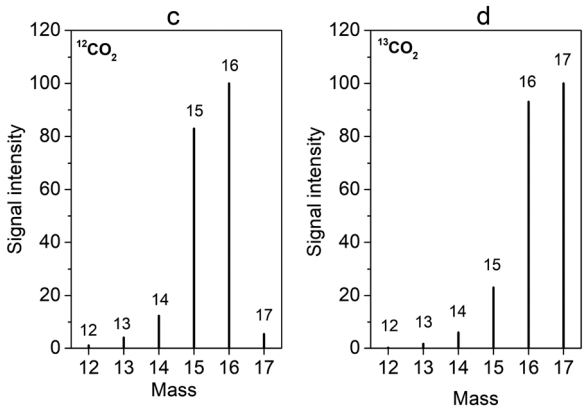

Fig. 16 Mass spectra labeling experiment demonstrating the carbon source for CH_4 production during CO_2 electrolysis, using **Fe13** as a molecular precursor catalyst. Reproduced with permission from ref. 255. Copyright 2019, Wiley.

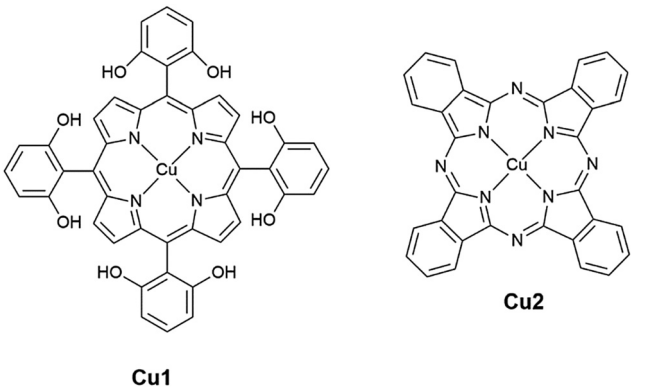

Chart 7 Copper-based molecular complexes as pre-catalysts for CO_2 reduction.

proper proof for the carbon source was brought about by the observation of an *m/z* 17 peak in GC/MS for methane when $^{13}CO_2$ was used as the reactant, along with correct fragmentation pattern and retention time as shown in Fig. 16.

The same phenomena were observed for copper based porphyrin and phthalocyanine **Cu1** and **Cu2** catalysts (Chart 7) that decompose into Cu NPs upon electrolysis in water (0.5 M $KHCO_3$) when deposited as thin films on carbon paper electrode or carbon electrodes. The nano-catalysts have higher activity for CH_4 and C_2H_4 than a bare Cu surface, with partial current density in the range of *ca.* 8.5 and 13 mA cm^{-2} respectively, at a potential close to −1 V *vs.* RHE.[256,257] These spectacular cases call for extreme vigilance not only about the carbon source but also about the actual state of the catalyst. For **Cu1**, catalysis was indeed originally claimed to be a molecular process.[256] In all these above reported examples (**Fe13**, **Cu1**, **Cu2**) the ligand might have an effect on NPs shaping upon decomposition.

Overall, these molecular pre-catalysts certainly deserve to be vigorously investigated since it may lead to unexpected catalytic properties and high activity.

The next challenge will be to design molecular catalysts able to create C–C bonds so as to produce highly reduced compounds such as alkenes and alcohols. It probably comes with no surprise that all examples investigated so far for multi-electron multi-proton ($n > 2$) CO_2 reduction, involving monometallic complexes under homogeneous conditions or deposited in thin films, have not led to dimerization or coupling of partially reduced substrates (*e.g.* CO, HCOOH) bound at the two closely spaced metal centers. Such coupling has indeed been shown to be a key step in heterogeneous catalysis, for example at copper materials. The development of multimetallic molecular complexes able to bind several CO_2 molecules at a time in a controlled environment may open interesting perspectives toward this challenge.

Concluding remarks

Multi-facet mechanistic and spectroscopic studies have allowed making progress in the understanding of catalytic processes involved during CO_2 reduction with molecular complexes.

Much remains to be done, both in electrochemical and light-driven catalysis. Further progress will certainly emerge from advanced mechanistic and *in situ*/*in operando* spectroscopic studies allowing not only deciphering the elementary steps of the processes but also clear identification of the degradation pathway(s). It will then open a path toward rational tuning of the next generation of catalysts. Nevertheless, Co, Fe and Ni coordinated by azamacrocycles and polypyridine ligands have led to high reactivity towards electrochemical and visible-light driven CO_2 reduction to CO and formate, both in organic solvents and in water. Robust catalysts, once immobilized onto conductive supports, have shown remarkable stability, extending over a day. The achievement of high current densities in electrochemical cells has opened a door to the design of devices at the industrial scale. Progress has also been made recently with hybrid materials in which molecular catalysts are connected to semi-conductive particles or bulk electrodes. Studies of such materials are certainly an area that could strongly benefit from the synergistic combination of homogeneous and heterogeneous catalysis. Finally, the ability of molecular catalysts to drive the multi-electron multi-proton reduction of CO_2 beyond CO and formate, even if still limited to a few examples, opens new exciting perspectives for the synthesis of more complex molecules, with the creation of carbon–carbon bonds. Development of such processes using well defined metal complexes will lead to a breakthrough in CO_2 reduction chemistry.

Abbreviations

P	Oxidized form of the catalyst (inactive)
Q	Reduced form of the catalyst (active)
A	Substrate
B	Product
i	Catalytic current
i_0	Peak current in the absence of substrate
$i_{plateau}$	Scan rate independent catalytic plateau current
F	Faraday constant
S	Electrode geometric surface area
C_A^0	Substrate concentration in the bulk solution
C_P^0	Catalyst concentration in the bulk solution
D_P	Catalyst diffusion coefficient
D_A	Substrate diffusion coefficient in solution
D_S	Substrate diffusion coefficient in a film
d_f	Catalytic film thickness
κ_A	Substrate partition coefficient in a film
v	Scan rate
R	Gas constant
T	Temperature
E	Applied potential
$E^0_{P/Q}$	Standard potential of the P/Q redox couple
k_s	Standard electron transfer rate constant
k_{cat}	(Pseudo first order) rate constant of the catalytic process
η	Overpotential
TOF	Turnover frequency
TON	Turnover number
NHE	Normal hydrogen electrode
RHE	Reversible hydrogen electrode
SCE	Standard calomel electrode
GC	Glassy carbon (electrode)
GDE	Gas diffusion electrode
CPE	Controlled potential electrolysis
CV	Cyclic voltammetry/cyclic voltammogram
QD	Quantum dot
MWCNT	Multiwalled carbon nanotube
EA	Electron acceptor
SD	Sacrificial electron donor
PS	Photosensitizer

Conflicts of interest

The authors declare no conflicts of interest.

Acknowledgements

This work was financially supported by Université de Paris, CNRS, Air Liquide, SATT Erganeo and the French National Agency for Research (ANR-16-CE05-0010-01). M. W. and B. M. thank the China Scholarship Council for their PhD fellowship (CSC student number 201606220034 and 201707040042, respectively) and partial financial support to M. R. from the Institut Universitaire de France (IUF) is also gratefully acknowledged.

References

1 S. Meshitsuka, M. Ichikawa and K. Tamaru, *J. Chem. Soc., Chem. Commun.*, 1974, 158–159.
2 J.-M. Savéant, *Chem. Rev.*, 2008, **108**, 2348–2378.
3 E. E. Benson, C. P. Kubiak, A. J. Sathrum and J. M. Smieja, *Chem. Soc. Rev.*, 2009, **38**, 89–99.
4 C. Costentin, M. Robert and J. M. Savéant, *Chem. Soc. Rev.*, 2013, **42**, 2423–2436.
5 R. Francke, B. Schille and M. Roemelt, *Chem. Rev.*, 2018, **118**, 4631–4701.
6 K. E. Dalle, J. Warnan, J. J. Leung, B. Reuillard, I. S. Karmel and E. Reisner, *Chem. Rev.*, 2019, **119**, 2752–2875.
7 C. Jiang, A. W. Nichols and C. W. Machan, *Dalton Trans.*, 2019, **48**, 9454–9468.
8 C. Costentin, S. Drouet, M. Robert and J. M. Savéant, *J. Am. Chem. Soc.*, 2012, **134**, 11235–11242.
9 B. M. L. Dioos, I. F. J. Vankelecom and P. A. Jacobs, *Adv. Synth. Catal.*, 2006, **348**, 1413–1446.
10 D. M. Chisholm and J. Scott McIndoe, *Dalton Trans.*, 2008, 3933–3945.
11 X.-M. Hu, S. U. Pedersen and K. Daasbjerg, *Curr. Opin. Electrochem.*, 2019, **15**, 148–154.
12 L. Sun, V. Reddu, A. C. Fisher and X. Wang, *Energy Environ. Sci.*, 2020, **13**, 374–403.
13 J.-P. Jones, G. K. S. Prakash and G. A. Olah, *Isr. J. Chem.*, 2014, **54**, 1451–1466.

14 C. Costentin, M. Robert and J.-M. Savéant, *Curr. Opin. Electrochem.*, 2017, **2**, 26–31.
15 J.-M. Savéant, *Elements of Molecular and Biomolecular Electrochemistry*, John Wiley & Sons, 2006, pp. 78–181.
16 C. Costentin and J.-M. Savéant, *ChemElectroChem*, 2014, **1**, 1226–1236.
17 I. Azcarate, C. Costentin, M. Robert and J.-M. Savéant, *J. Phys. Chem. C*, 2016, **120**, 28951–28960.
18 C. Cometto, L. Chen, P.-K. Lo, Z. Guo, K.-C. Lau, E. Anxolabéhère-Mallart, C. Fave, T.-C. Lau and M. Robert, *ACS Catal.*, 2018, **8**, 3411–3417.
19 C. Cometto, L. Chen, E. Anxolabéhère-Mallart, C. Fave, T.-C. Lau and M. Robert, *Organometallics*, 2019, **38**, 1280–1285.
20 C. Costentin, S. Drouet, G. Passard, M. Robert and J. M. Savéant, *J. Am. Chem. Soc.*, 2013, **135**, 9023–9031.
21 N. Elgrishi, M. B. Chambers and M. Fontecave, *Chem. Sci.*, 2015, **6**, 2522–2531.
22 C. Costentin, S. Drouet, M. Robert and J.-M. Savéant, *Science*, 2012, **338**, 90–94.
23 C. Costentin, D. G. Nocera and C. N. Brodsky, *Proc. Natl. Acad. Sci. U. S. A.*, 2017, **114**, 11303–11308.
24 M. Wang, L. Chen, T. C. Lau and M. Robert, *Angew. Chem., Int. Ed.*, 2018, **57**, 7769–7773.
25 A. Maurin and M. Robert, *J. Am. Chem. Soc.*, 2016, **138**, 2492–2495.
26 C. Costentin and J.-M. Savéant, *ChemElectroChem*, 2015, **2**, 1774–1784.
27 C. P. Andrieux, C. Costentin, C. Di Giovanni, J.-M. Savéant and C. Tard, *J. Phys. Chem. C*, 2016, **120**, 21263–21271.
28 C. Costentin and J.-M. Savéant, *J. Phys. Chem. C*, 2015, **119**, 12174–12182.
29 J.-M. Savéant, *ChemElectroChem*, 2016, **3**, 1967–1977.
30 W. Kaim and A. Klein, *Spectroelectrochemistry*, The Royal Society of Chemistry, 2008.
31 A. W. B. Aylmer-Kelly, P. R. C. A. Bewick and A. M. Tuxford, *Faraday Discuss. Chem. Soc.*, 1973, **56**, 96–107.
32 K. Chandrasekaran and J. O. M. Bockris, *Surf. Sci.*, 1987, **185**, 495–514.
33 J. Desilvestro and S. Pons, *J. Electroanal. Chem.*, 1989, **267**, 207–220.
34 E. Anxolabéhère, G. Chottard and D. Lexa, *New J. Chem.*, 1994, **18**, 889–899.
35 C. Romelt, J. Song, M. Tarrago, J. A. Rees, M. van Gastel, T. Weyhermuller, S. DeBeer, E. Bill, F. Neese and S. Ye, *Inorg. Chem.*, 2017, **56**, 4746–4751.
36 C. Romelt, S. Ye, E. Bill, T. Weyhermuller, M. van Gastel and F. Neese, *Inorg. Chem.*, 2018, **57**, 2141–2148.
37 C. Costentin, J. M. Savéant and C. Tard, *Proc. Natl. Acad. Sci. U. S. A.*, 2018, **115**, 9104–9109.
38 B. Mondal, A. Rana, P. Sen and A. Dey, *J. Am. Chem. Soc.*, 2015, **137**, 11214–11217.
39 A. W. Nichols, S. Chatterjee, M. Sabat and C. W. Machan, *Inorg. Chem.*, 2018, **57**, 2111–2121.
40 Z. Guo, G. Chen, C. Cometto, B. Ma, H. Zhao, T. Groizard, L. Chen, H. Fan, W.-L. Man, S.-M. Yiu, K.-C. Lau, T.-C. Lau and M. Robert, *Nat. Catal.*, 2019, **2**, 801–808.
41 S. Fernandez, F. Franco, C. Casadevall, V. Martin-Diaconescu, J. M. Luis and J. Lloret-Fillol, *J. Am. Chem. Soc.*, 2020, **142**, 120–133.
42 D. Behar, T. Dhanasekaran, P. Neta, C. M. Hosten, D. Ejeh, P. Hambright and E. Fujita, *J. Phys. Chem. A*, 1998, **102**, 2870–2877.
43 H. Sheng and H. Frei, *J. Am. Chem. Soc.*, 2016, **138**, 9959–9967.
44 N. Kornienko, Y. Zhao, C. S. Kley, C. Zhu, D. Kim, S. Lin, C. J. Chang, O. M. Yaghi and P. Yang, *J. Am. Chem. Soc.*, 2015, **137**, 14129–14135.
45 I. S. Zavarine and C. P. Kubiak, *J. Electroanal. Chem.*, 2001, **495**, 106–109.
46 M. Krejčik, M. Daněk and F. Hartl, *J. Electroanal. Chem.*, 1991, **317**, 179–187.
47 C. Cometto, Doctoral thesis, Université Paris Diderot, 2018.
48 C. Gueutin and D. Lexa, *Electroanalysis*, 1996, **8**, 1029–1033.
49 C. W. Machan, M. D. Sampson, S. A. Chabolla, T. Dang and C. P. Kubiak, *Organometallics*, 2014, **33**, 4550–4559.
50 J. D. Froehlich and C. P. Kubiak, *J. Am. Chem. Soc.*, 2015, **137**, 3565–3573.
51 L. E. Lieske, A. L. Rheingold and C. W. Machan, *Sustainable Energy Fuels*, 2018, **2**, 1269–1277.
52 S. L. Behnke, A. C. Manesis and H. S. Shafaat, *Dalton Trans.*, 2018, **47**, 15206–15216.
53 M. Wang, L. Árnadóttir, Z. J. Xu and Z. Feng, *Nano-Micro Lett.*, 2019, 11.
54 E. Fujita, L. R. Furenlid and M. W. Renner, *J. Am. Chem. Soc.*, 1997, **119**, 4549–4550.
55 I. T. Bae and D. A. Scherson, *J. Phys. Chem. B*, 1998, **102**, 2519–2522.
56 L. R. Furenlid, M. W. Renner and E. Fujita, *Physica B*, 1995, **208–209**, 739–742.
57 S.-K. Lee, S. D. George, W. E. Antholine, B. Hedman, K. O. Hodgson and E. I. Solomon, *J. Am. Chem. Soc.*, 2002, **124**, 6180–6193.
58 M. W. Kanan, J. Yano, Y. Surendranath, M. Dincă, V. K. Yachandra and D. G. Nocera, *J. Am. Chem. Soc.*, 2010, **132**, 13692–13701.
59 P. S. Miedema, M. M. van Schooneveld, R. Bogerd, T. C. R. Rocha, M. Hävecker, A. Knop-Gericke and F. M. F. de Groot, *J. Phys. Chem. C*, 2011, **115**, 25422–25428.
60 E. M. Erickson, M. S. Thorum, R. Vasic, N. S. Marinkovic, A. I. Frenkel, A. A. Gewirth and R. G. Nuzzo, *J. Am. Chem. Soc.*, 2012, **134**, 197–200.
61 Y. Gorlin, B. Lassalle-Kaiser, J. D. Benck, S. Gul, S. M. Webb, V. K. Yachandra, J. Yano and T. F. Jaramillo, *J. Am. Chem. Soc.*, 2013, **135**, 8525–8534.
62 E. E. Benson, M. D. Sampson, K. A. Grice, J. M. Smieja, J. D. Froehlich, D. Friebel, J. A. Keith, E. A. Carter, A. Nilsson and C. P. Kubiak, *Angew. Chem., Int. Ed.*, 2013, **52**, 4841–4844.
63 D. Karapinar, A. Zitolo, T. N. Huan, S. Zanna, D. Taverna, L. H. Galvao Tizei, D. Giaume, P. Marcus, V. Mougel and M. Fontecave, *ChemSusChem*, 2020, **13**, 173–179.

64 N. Han, Y. Wang, L. Ma, J. Wen, J. Li, H. Zheng, K. Nie, X. Wang, F. Zhao, Y. Li, J. Fan, J. Zhong, T. Wu, D. J. Miller, J. Lu, S.-T. Lee and Y. Li, *Chem*, 2017, **3**, 652–664.
65 E. Boutin, M. Wang, J. C. Lin, M. Mesnage, D. Mendoza, B. Lassalle-Kaiser, C. Hahn, T. Jaramillo and M. Robert, *Angew. Chem., Int. Ed.*, 2019, **58**, 16172–16176.
66 D. Gianolo, *X-Ray Absorption and X-Ray Emission Spectroscopy*, Wiley, 2016, ch. 5, pp. 99–124, DOI: 10.1002/9781118844243.ch5.
67 T. Masuda, *Top. Catal.*, 2018, **61**, 2103–2113.
68 B. Lassalle-Kaiser, S. Gul, J. Kern, V. K. Yachandra and J. Yano, *J. Electron Spectrosc. Relat. Phenom.*, 2017, **221**, 18–27.
69 Y. Gorlin, B. Lassalle-Kaiser, J. D. Benck, S. Gul, S. M. Webb, V. K. Yachandra, J. Yano and T. F. Jaramillo, *J. Am. Chem. Soc.*, 2013, **135**, 8525–8534.
70 K. Cheaib, B. Maurice, T. Mateo, Z. Halime and B. Lassalle-Kaiser, *J. Synchrotron Radiat.*, 2019, **26**, 1980–1985.
71 S. P. Best, A. Levina, C. Glover, B. Johannessen, P. Kappen and P. A. Lay, *J. Synchrotron Radiat.*, 2016, **23**, 743–750.
72 O. Wolter and J. Heitbaum, *Ber. Bunsenges. Phys. Chem.*, 1984, **88**, 2–6.
73 P. Dubé and G. M. Brisard, *J. Electroanal. Chem.*, 2005, **582**, 230–240.
74 E. L. Clark, M. R. Singh, Y. Kwon and A. T. Bell, *Anal. Chem.*, 2015, **87**, 8013–8020.
75 E. L. Clark and A. T. Bell, *J. Am. Chem. Soc.*, 2018, **140**, 7012–7020.
76 Y. Lai, R. J. R. Jones, Y. Wang, L. Zhou and J. M. Gregoire, *ACS Comb. Sci.*, 2019, **21**, 692–704.
77 R. Kortlever, C. Balemans, Y. Kwon and M. T. M. Koper, *Catal. Today*, 2015, **244**, 58–62.
78 A. H. Wonders, T. H. M. Housmans, V. Rosca and M. T. M. Koper, *J. Appl. Electrochem.*, 2006, **36**, 1215–1221.
79 K. J. P. Schouten, Y. Kwon, C. J. M. van der Ham, Z. Qin and M. T. M. Koper, *Chem. Sci.*, 2011, **2**, 1902–1909.
80 R. Kortlever, K. H. Tan, Y. Kwon and M. T. M. Koper, *J. Solid State Electrochem.*, 2013, **17**, 1843–1849.
81 R. Kas, R. Kortlever, A. Milbrat, M. T. Koper, G. Mul and J. Baltrusaitis, *Phys. Chem. Chem. Phys.*, 2014, **16**, 12194–12201.
82 J. Shen, R. Kortlever, R. Kas, Y. Y. Birdja, O. Diaz-Morales, Y. Kwon, I. Ledezma-Yanez, K. J. P. Schouten, G. Mul and M. T. M. Koper, *Nat. Commun.*, 2015, **6**, 8177.
83 H. Baltruschat, *J. Am. Soc. Mass Spectrom.*, 2004, **15**, 1693–1706.
84 T. Hartung and H. Baltruschat, *Langmuir*, 1990, **6**, 953–957.
85 Y. Gao, H. Tsuji, H. Hattori and H. Kita, *J. Electroanal. Chem.*, 1994, **372**, 195–200.
86 K. Jambunathan, S. Jayaraman and A. C. Hillier, *Langmuir*, 2004, **20**, 1856–1863.
87 Y. Hirata, K. Suga and M. Fujihira, *Chem. Lett.*, 1990, 1155–1158.
88 H. Kazuya, T. Katsuhiro, S. Hideo and T. Shinobu, *Chem. Lett.*, 1977, 1137–1140.
89 H. Kazuya, T. Katsuhiro, S. Hideo and T. Shinobu, *Chem. Lett.*, 1979, 305–308.
90 B. J. Fisher and R. Eisenberg, *J. Am. Chem. Soc.*, 1980, **102**, 7361–7363.
91 L. Chen, Z. Guo, X.-G. Wei, C. Gallenkamp, J. Bonin, E. Anxolabéhère-Mallart, K.-C. Lau, T.-C. Lau and M. Robert, *J. Am. Chem. Soc.*, 2015, **137**, 10918–10921.
92 K.-W. Fung and T. C. W. Mak, *J. Chem. Soc., Dalton Trans.*, 1988, 2153–2159.
93 D. C. Lacy, C. C. L. McCrory and J. C. Peters, *Inorg. Chem.*, 2014, **53**, 4980–4988.
94 M. Zhang, M. El-Roz, H. Frei, J. L. Mendoza-Cortes, M. Head-Gordon, D. C. Lacy and J. C. Peters, *J. Phys. Chem. C*, 2015, **119**, 4645–4654.
95 A. Chapovetsky, T. H. Do, R. Haiges, M. K. Takase and S. C. Marinescu, *J. Am. Chem. Soc.*, 2016, **138**, 5765–5768.
96 A. Chapovetsky, M. Welborn, J. M. Luna, R. Haiges, T. F. Miller and S. C. Marinescu, *ACS Cent. Sci.*, 2018, **4**, 397–404.
97 N. Elgrishi, M. B. Chambers, V. Artero and M. Fontecave, *Phys. Chem. Chem. Phys.*, 2014, **16**, 13635–13644.
98 J. Schneider, H. Jia, K. Kobiro, D. E. Cabelli, J. T. Muckerman and E. Fujita, *Energy Environ. Sci.*, 2012, **5**, 9502–9510.
99 M. Beley, J.-P. Collin, R. Ruppert and J.-P. Sauvage, *J. Chem. Soc., Chem. Commun.*, 1984, 1315–1316.
100 M. Beley, J.-P. Collin, R. Ruppert and J.-P. Sauvage, *J. Am. Chem. Soc.*, 1986, **108**, 7461–7467.
101 J. P. Collin, A. Jouaiti and J. P. Sauvage, *Inorg. Chem.*, 1988, **27**, 1986–1990.
102 G. B. Balazs and F. C. Anson, *J. Electroanal. Chem.*, 1992, **322**, 325–335.
103 K. Bujno, R. Bilewicz, L. Siegfries and T. A. Kaden, *J. Electroanal. Chem.*, 1998, **445**, 47–53.
104 S. Sakaki, *J. Am. Chem. Soc.*, 1992, **114**, 2055–2062.
105 J. D. Froehlich and C. P. Kubiak, *Inorg. Chem.*, 2012, **51**, 3932–3934.
106 Y. Wu, B. Rudshteyn, A. Zhanaidarova, J. D. Froehlich, W. Ding, C. P. Kubiak and V. S. Batista, *ACS Catal.*, 2017, **7**, 5282–5288.
107 I. Bhugun, D. Lexa and J.-M. Savéant, *J. Am. Chem. Soc.*, 1994, **116**, 5015–5016.
108 I. Bhugun, D. Lexa and J.-M. Savéant, *J. Phys. Chem.*, 1996, **100**, 19981–19985.
109 C. Costentin, M. Robert, J. M. Saveant and A. Tatin, *Proc. Natl. Acad. Sci. U. S. A.*, 2015, **112**, 6882–6886.
110 C. Costentin, G. Passard, M. Robert and J. M. Saveant, *J. Am. Chem. Soc.*, 2014, **136**, 11821–11829.
111 I. Azcarate, C. Costentin, M. Robert and J. M. Saveant, *J. Am. Chem. Soc.*, 2016, **138**, 16639–16644.
112 C. G. Margarit, N. G. Asimow, C. Costentin and D. G. Nocera, *ACS Energy Lett.*, 2020, **5**, 72–78.
113 M. N. Mahmood, D. Massheder and C. J. Harty, *J. Appl. Electrochem.*, 1987, **17**, 1223–1227.
114 N. Furuya and K. Matsui, *J. Electroanal. Chem.*, 1989, **271**, 181–190.
115 M. Wang, K. Torbensen, D. Salvatore, S. Ren, D. Joulie, F. Dumoulin, D. Mendoza, B. Lassalle-Kaiser, U. Isci, C. P. Berlinguette and M. Robert, *Nat. Commun.*, 2019, **10**, 3602.

116 X. Zhang, Z. Wu, X. Zhang, L. Li, Y. Li, H. Xu, X. Li, X. Yu, Z. Zhang, Y. Liang and H. Wang, *Nat. Commun.*, 2017, **8**, 14675.
117 X. Li, W. Bi, M. Chen, Y. Sun, H. Ju, W. Yan, J. Zhu, X. Wu, W. Chu, C. Wu and Y. Xie, *J. Am. Chem. Soc.*, 2017, **139**, 14889–14892.
118 S. Ren, D. Joulié, D. Salvatore, K. Torbensen, M. Wang, M. Robert and C. Berlinguette, *Science*, 2019, **365**, 367–369.
119 K. Torbensen, C. Han, B. Boudy, N. von Wolff, C. Bertail, W. Braun and M. Robert, *Chem. – Eur. J.*, 2020, **26**, 3034–3038.
120 A. Tatin, C. m. Comminges, B. Kokoh, C. Costentin, M. Robert and J.-M. Savéant, *Proc. Natl. Acad. Sci. U. S. A.*, 2016, **113**, 5526–5529.
121 M. Zhu, J. Chen, L. Huang, R. Ye, J. Xu and Y. F. Han, *Angew. Chem., Int. Ed.*, 2019, **58**, 6595–6599.
122 H. Wang, D. Y. C. Leung and J. Xuan, *Appl. Energy*, 2013, **102**, 1057–1062.
123 M. Bevilacqua, J. Filippi, A. Lavacchi, A. Marchionni, H. A. Miller, W. Oberhauser, E. Vesselli and F. Vizza, *Energy Technol.*, 2014, **2**, 522–525.
124 I. Merino-Garcia, E. Alvarez-Guerra, J. Albo and A. Irabien, *Chem. Eng. J.*, 2016, **305**, 104–120.
125 D. A. Salvatore, D. M. Weekes, J. He, K. E. Dettelbach, Y. C. Li, T. E. Mallouk and C. P. Berlinguette, *ACS Energy Lett.*, 2018, **3**, 149–154.
126 T. Burdyny and W. A. Smith, *Energy Environ. Sci.*, 2019, **12**, 1442–1453.
127 R. B. Kutz, Q. Chen, H. Yang, S. D. Sajjad, Z. Liu and I. R. Masel, *Energy Technol.*, 2017, **5**, 929–936.
128 C.-T. Dinh, F. P. García de Arquer, D. Sinton and E. H. Sargent, *ACS Energy Lett.*, 2018, **3**, 2835–2840.
129 S. Verma, Y. Hamasaki, C. Kim, W. Huang, S. Lu, H.-R. M. Jhong, A. A. Gewirth, T. Fujigaya, N. Nakashima and P. J. A. Kenis, *ACS Energy Lett.*, 2018, **3**, 193–198.
130 H. Yang, Q. Lin, C. Zhang, X. Yu, Z. Cheng, G. Li, Q. Hu, X. Ren, Q. Zhang, J. Liu and C. He, *Nat. Commun.*, 2020, **11**, 593.
131 N. Furuya and S. Koide, *Electrochim. Acta*, 1991, **36**, 1309–1313.
132 N. Sonoyama, M. Kirii and T. Sakata, *Electrochem. Commun.*, 1999, **1**, 213–216.
133 X. Lu, Y. Wu, X. Yuan, L. Huang, Z. Wu, J. Xuan, Y. Wang and H. Wang, *ACS Energy Lett.*, 2018, **3**, 2527–2532.
134 C. Jiang, A. W. Nichols, J. F. Walzer and C. W. Machan, *Inorg. Chem.*, 2020, **59**, 1883–1892.
135 S. Ringe, E. L. Clark, J. Resasco, A. Walton, B. Seger, A. T. Bell and K. Chan, *Energy Environ. Sci.*, 2019, **12**, 3001–3014.
136 X. Chen, S. Shen, L. Guo and S. S. Mao, *Chem. Rev.*, 2010, **110**, 6503–6570.
137 M. Schreier, P. Gao, M. T. Mayer, J. Luo, T. Moehl, M. K. Nazeeruddin, S. D. Tilley and M. Gratzel, *Energy Environ. Sci.*, 2015, **8**, 855–861.
138 T. Arai, S. Sato and T. Morikawa, *Energy Environ. Sci.*, 2015, **8**, 1998–2002.
139 M. G. Bradley, T. Tysak, D. J. Graves and N. A. Viachiopoulos, *J. Chem. Soc., Chem. Commun.*, 1983, 349–350.
140 Y. Matsubara, *ACS Energy Lett.*, 2017, **2**, 1886–1891.
141 M. Beley, J.-P. Collin, J.-P. Sauvage, J.-P. Petit and P. Chartier, *J. Electroanal. Chem. Interfacial Electrochem.*, 1986, **206**, 333–339.
142 J. P. Petit, P. Chartier, M. Beley and J. P. Sauvage, *New J. Chem.*, 1987, **11**, 751.
143 J.-P. Petit, P. Chartier, M. Beley and J.-P. Deville, *J. Electroanal. Chem.*, 1989, **269**, 267–281.
144 J. O. M. Bockris and J. C. Wass, *Mater. Chem. Phys.*, 1989, **22**, 249–280.
145 C. R. Cabrera and H. D. Abruña, *J. Electroanal. Chem. Interfacial Electrochem.*, 1986, **209**, 101–107.
146 J. P. Collin and J. P. Sauvage, *Coord. Chem. Rev.*, 1989, **93**, 245–268.
147 B. Kumar, J. M. Smieja and C. P. Kubiak, *J. Phys. Chem. C*, 2010, **114**, 14220–14223.
148 T. Arai, S. Sato, K. Uemura, T. Morikawa, T. Kajino and T. Motohiro, *Chem. Commun.*, 2010, **46**, 6944–6946.
149 T. Arai, S. Tajima, S. Sato, K. Uemura, T. Morikawa and T. Kajino, *Chem. Commun.*, 2011, **47**, 12664–12666.
150 S. Sato, T. Arai, T. Morikawa, K. Uemura, T. M. Suzuki, H. Tanaka and T. Kajino, *J. Am. Chem. Soc.*, 2011, **133**, 15240–15243.
151 B. Kumar, J. M. Smieja, A. F. Sasayama and C. P. Kubiak, *Chem. Commun.*, 2012, **48**, 272–274.
152 T. Arai, S. Sato, T. Kajino and T. Morikawa, *Energy Environ. Sci.*, 2013, **6**, 1274–1282.
153 E. Torralba-Peñalver, Y. Luo, J.-D. Compain, S. Chardon-Noblat and B. Fabre, *ACS Catal.*, 2015, **5**, 6138–6147.
154 K. Alenezi, S. K. Ibrahim, P. Li and C. J. Pickett, *Chem. – Eur. J.*, 2013, **19**, 13522–13527.
155 D. He, T. Jin, W. Li, S. Pantovich, D. Wang and G. Li, *Chem. – Eur. J.*, 2016, **22**, 13064–13067.
156 H. Gerischer, *J. Electroanal. Chem.*, 1977, **82**, 133–143.
157 B. Kumar, M. Llorente, J. Froehlich, T. Dang, A. Sathrum and C. P. Kubiak, *Annu. Rev. Phys. Chem.*, 2012, **63**, 541–569.
158 A. H. A. Tinnemans, T. P. M. Koster, D. H. M. W. Thewissen and A. Mackor, *Recl. Trav. Chim. Pays-Bas*, 1984, **103**, 288–295.
159 M. Schreier, J. Luo, P. Gao, T. Moehl, M. T. Mayer and M. Grätzel, *J. Am. Chem. Soc.*, 2016, **136**, 1938–1946.
160 K. Sekizawa, S. Sato, T. Arai and T. Morikawa, *ACS Catal.*, 2018, **8**, 1405–1416.
161 J. J. Leung, J. Warnan, K. H. Ly, N. Heidary, D. H. Nam, M. F. Kuehnel and E. Reisner, *Nat. Catal.*, 2019, **2**, 354–365.
162 Y. Kou, S. Nakatani, G. Sunagawa, Y. Tachikawa, D. Masui, T. Shimada, S. Takagi, D. A. Tryk, Y. Nabetani, H. Tachibana and H. Inoue, *J. Catal.*, 2014, **310**, 57–66.
163 T.-T. Li, B. Shan and T. J. Meyer, *ACS Energy Lett.*, 2019, **4**, 629–636.
164 G. Sahara, R. Abe, M. Higashi, T. Morikawa, K. Maeda, Y. Ueda and O. Ishitani, *Chem. Commun.*, 2015, **51**, 10722–10725.
165 G. Sahara, H. Kumagai, K. Maeda, N. Kaeffer, V. Artero, M. Higashi, R. Abe and O. Ishitani, *J. Am. Chem. Soc.*, 2016, **138**, 14152–14158.

166 H. Kumagai, G. Sahara, K. Maeda, M. Higashi, R. Abe and O. Ishitani, *Chem. Sci.*, 2017, **8**, 4242–4249.
167 B. Shan, S. Vanka, T.-T. Li, L. Troian-Gautier, M. K. Brennaman, Z. Mi and T. J. Meyer, *Nat. Energy*, 2019, **4**, 290–299.
168 A. J. Bard, A. B. Bocarsly, F. R. F. Fan, E. G. Walton and M. S. Wrighton, *J. Am. Chem. Soc.*, 1980, **102**, 3671–3677.
169 J. J. H. Pijpers, M. T. Winkler, Y. Surendranath, T. Buonassisi and D. G. Nocera, *Proc. Natl. Acad. Sci. U. S. A.*, 2011, **108**, 10056–10061.
170 T. E. Rosser, C. D. Windle and E. Reisner, *Angew. Chem., Int. Ed.*, 2016, **55**, 7388–7392.
171 Y.-S. Kim, S. Kriegel, K. D. Harris, C. Costentin, B. Limoges and V. Balland, *J. Phys. Chem. C*, 2017, **121**, 10325–10335.
172 N. E. Mendieta-Reyes, W. Cheuquepán, A. Rodes and R. Gómez, *ACS Catal.*, 2020, **10**, 103–113.
173 K. L. Materna, R. H. Crabtree and G. W. Brudvig, *Chem. Soc. Rev.*, 2017, **46**, 6099–6110.
174 D. Bae, T. Pedersen, B. Seger, M. Malizia, A. Kuznetsov, O. Hansen, I. Chorkendorff and P. C. K. Vesborg, *Energy Environ. Sci.*, 2015, **8**, 650–660.
175 M.-K. Son, L. Steier, M. Schreier, M. T. Mayer, J. Luo and M. Gratzel, *Energy Environ. Sci.*, 2017, **10**, 912–918.
176 K. Mochizuki, S. Manaka, I. Takeda and T. Kondo, *Inorg. Chem.*, 1996, **35**, 5132–5136.
177 M. Shinjiro, Y. Kiichi, P. Chyongjin and Y. Shozo, *Chem. Lett.*, 1991, 2099–2100.
178 S. Matsuoka, K. Yamamoto, T. Ogata, M. Kusaba, N. Nakashima, E. Fujita and S. Yanagida, *J. Am. Chem. Soc.*, 1993, **115**, 601–609.
179 T. Ogata, Y. Yamamoto, Y. Wada, K. Murakoshi, M. Kusaba, N. Nakashima, A. Ishida, S. Takamuku and S. Yanagida, *J. Phys. Chem.*, 1995, **99**, 11916–11922.
180 E. Fujita, D. J. Szalda, C. Creutz and N. Sutin, *J. Am. Chem. Soc.*, 1988, **110**, 4870–4871.
181 E. Fujita, C. Creutz, N. Sutin and B. S. Brunschwig, *Inorg. Chem.*, 1993, **32**, 2657–2662.
182 T. Ogata, S. Yanagida, B. S. Brunschwig and E. Fujita, *J. Am. Chem. Soc.*, 1995, **117**, 6708–6716.
183 T. Ogata, S. Yanagida, B. S. Brunschwig and E. Fujita, *Energy Convers. Manage.*, 1995, **36**, 669–672.
184 Y. Qin, L. Chen, G. Chen, Z. Guo, L. Wang, H. Fan, M. Robert and T.-C. Lau, *Chem. Commun.*, 2020, **56**, 6249–6252.
185 T. Dhanasekaran, J. Grodkowski, P. Neta, P. Hambright and E. Fujita, *J. Phys. Chem. A*, 1999, **103**, 7742–7748.
186 J. Grodkowski and P. Neta, *J. Phys. Chem. A*, 2000, **104**, 4475–4479.
187 J. Grodkowski, D. Behar, P. Neta and P. Hambright, *J. Phys. Chem. A*, 1997, **101**, 248–254.
188 J. Bonin, M. Chaussemier, M. Robert and M. Routier, *ChemCatChem*, 2014, **6**, 3200–3207.
189 J. Grodkowski, T. Dhanasekaran, P. Neta, P. Hambright, B. S. Brunschwig, K. Shinozaki and E. Fujita, *J. Phys. Chem. A*, 2000, **104**, 11332–11339.
190 J. Grodkowski, P. Neta, E. Fujita, A. Mahammed, L. Simkhovich and Z. Gross, *J. Phys. Chem. A*, 2002, **106**, 4772–4778.
191 J. Bonin, M. Robert and M. Routier, *J. Am. Chem. Soc.*, 2014, **136**, 16768–16771.
192 H. Rao, J. Bonin and M. Robert, *Chem. Commun.*, 2017, **53**, 2830–2833.
193 H. Rao, J. Bonin and M. Robert, *ChemSusChem*, 2017, **10**, 4447–4450.
194 H. Rao, J. Bonin and M. Robert, *J. Phys. Chem. C*, 2018, **122**, 13834–13839.
195 P. G. Alsabeh, A. Rosas-Hernández, E. Barsch, H. Junge, R. Ludwig and M. Beller, *Catal. Sci. Technol.*, 2016, **6**, 3623–3630.
196 A. Rosas-Hernandez, P. G. Alsabeh, E. Barsch, H. Junge, R. Ludwig and M. Beller, *Chem. Commun.*, 2016, **52**, 8393–8396.
197 A. Rosas-Hernández, C. Steinlechner, H. Junge and M. Beller, *Green Chem.*, 2017, **19**, 2356–2360.
198 H. Takeda, K. Ohashi, A. Sekine and O. Ishitani, *J. Am. Chem. Soc.*, 2016, **138**, 4354–4357.
199 E. Kimura, X. Bu, M. Shionoya, S. Wada and S. Maruyama, *Inorg. Chem.*, 1992, **31**, 4542–4546.
200 C. Herrero, A. Quaranta, S. El Ghachtouli, B. Vauzeilles, W. Leibl and A. Aukauloo, *Phys. Chem. Chem. Phys.*, 2014, **16**, 12067–12072.
201 K. Nobuko, H. Yuichiro, H. Takuji, S. Hideki and K. Kazuyuki, *Bull. Chem. Soc. Jpn.*, 1999, **72**, 725–731.
202 X. Wang, V. Goudy, G. Genesio, J. Maynadié, D. Meyer and M. Fontecave, *Chem. Commun.*, 2017, **53**, 5040–5043.
203 A. D. Handoko, K. Li and J. Tang, *Curr. Opin. Chem. Eng.*, 2013, **2**, 200–206.
204 B. Zhang and L. Sun, *Chem. Soc. Rev.*, 2019, **48**, 2216–2264.
205 T. Jin, C. Liu and G. Li, *J. Coord. Chem.*, 2016, **69**, 1748–1758.
206 T. Fenton, S. Gillingham, T. Jin and G. Li, *Dalton Trans.*, 2017, **46**, 10721–10726.
207 X. Wang, I. Thiel, A. Fedorov, C. Copéret, V. Mougel and M. Fontecave, *Chem. Sci.*, 2017, **8**, 8204–8213.
208 Y. Fu, D. Sun, Y. Chen, R. Huang, Z. Ding, X. Fu and Z. Li, *Angew. Chem., Int. Ed.*, 2012, **51**, 3364–3367.
209 D. Sun, Y. Fu, W. Liu, L. Ye, D. Wang, L. Yang, X. Fu and Z. Li, *Chem. – Eur. J.*, 2013, **19**, 14279–14285.
210 D. Wang, R. Huang, W. Liu, D. Sun and Z. Li, *ACS Catal.*, 2014, **4**, 4254–4260.
211 S. Wang, W. Yao, J. Lin, Z. Ding and X. Wang, *Angew. Chem., Int. Ed.*, 2014, **53**, 1034–1038.
212 C. Wang, Z. Xie, K. E. deKrafft and W. Lin, *J. Am. Chem. Soc.*, 2011, **133**, 13445–13454.
213 T. Atoguchi, A. Aramata, A. Kazusaka and M. Enyo, *J. Chem. Soc., Chem. Commun.*, 1991, 156–157.
214 W. W. Kramer and C. C. L. McCrory, *Chem. Sci.*, 2016, **7**, 2506–2515.
215 N. Morlanés, K. Takanabe and V. Rodionov, *ACS Catal.*, 2016, **6**, 3092–3095.
216 S. Roy and E. Reisner, *Angew. Chem., Int. Ed.*, 2019, **58**, 12180–12184.
217 M. Zhu, J. Chen, R. Guo, J. Xu, X. Fang and Y.-F. Han, *Appl. Catal., B*, 2019, **251**, 112–118.

218 M. F. Kuehnel, K. L. Orchard, K. E. Dalle and E. Reisner, *J. Am. Chem. Soc.*, 2017, **139**, 7217–7223.
219 S. Lian, M. S. Kodaimati and E. A. Weiss, *ACS Nano*, 2018, **12**, 568–575.
220 T. Jin, C. Liu and G. Li, *Chem. Commun.*, 2014, **50**, 6221–6224.
221 C. D. Windle, E. Pastor, A. Reynal, A. C. Whitwood, Y. Vaynzof, J. R. Durrant, R. N. Perutz and E. Reisner, *Chem. – Eur. J.*, 2015, **21**, 3746–3754.
222 C. Liu, T. Jin, M. E. Louis, S. A. Pantovich, S. L. Skraba-Joiner, T. Rajh and G. Li, *J. Mol. Catal. A: Chem.*, 2016, **423**, 293–299.
223 G. Neri, M. Forster, J. J. Walsh, C. M. Robertson, T. J. Whittles, P. Farras and A. J. Cowan, *Chem. Commun.*, 2016, **52**, 14200–14203.
224 T. Wu, L. Zou, D. Han, F. Li, Q. Zhang and L. Niu, *Green Chem.*, 2014, **16**, 2142–2146.
225 L. Lin, C. Hou, X. Zhang, Y. Wang, Y. Chen and T. He, *Appl. Catal., B*, 2018, **221**, 312–319.
226 C. Cometto, R. Kuriki, L. Chen, K. Maeda, T.-C. Lau, O. Ishitani and M. Robert, *J. Am. Chem. Soc.*, 2018, **140**, 7437–7440.
227 B. Ma, G. Chen, C. Fave, L. Chen, R. Kuriki, K. Maeda, O. Ishitani, T.-C. Lau, J. Bonin and M. Robert, *J. Am. Chem. Soc.*, 2020, **142**, 6188–6195.
228 M. F. Kuehnel, C. D. Sahm, G. Neri, J. R. Lee, K. L. Orchard, A. J. Cowan and E. Reisner, *Chem. Sci.*, 2018, **9**, 2501–2509.
229 Z. Chen, Y. Hu, J. Wang, Q. Shen, Y. Zhang, C. Ding, Y. Bai, G. Jiang, Z. Li and N. Gaponik, *Chem. Mater.*, 2020, **32**, 1517–1525.
230 S. Lian, M. S. Kodaimati, D. S. Dolzhnikov, R. Calzada and E. A. Weiss, *J. Am. Chem. Soc.*, 2017, **139**, 8931–8938.
231 H. Rao, L. C. Schmidt, J. Bonin and M. Robert, *Nature*, 2017, **548**, 74–77.
232 H. Rao, C.-H. Lim, J. Bonin, G. M. Miyake and M. Robert, *J. Am. Chem. Soc.*, 2018, **140**, 17830–17834.
233 M. D. Rail and L. A. Berben, *J. Am. Chem. Soc.*, 2011, **133**, 18577–18579.
234 R. Angamuthu, P. Byers, M. Lutz, A. L. Spek and E. Bouwman, *Science*, 2010, **327**, 313.
235 E. A. Mohamed, Z. N. Zahran and Y. Naruta, *Chem. Commun.*, 2015, **51**, 16900–16903.
236 A. Taheri, E. J. Thompson, J. C. Fettinger and L. A. Berben, *ACS Catal.*, 2015, **5**, 7140–7151.
237 H. Dobbek, V. Svetlitchnyi, L. Gremer, R. Huber and O. Meyer, *Science*, 2001, **293**, 1281–1285.
238 C.-Y. Zhu, Y.-Q. Zhang, R.-Z. Liao, W. Xia, J.-C. Hu, J. Wu, H. Liu and F. Wang, *Dalton Trans.*, 2018, **47**, 13142–13150.
239 T. Ouyang, H.-H. Huang, J.-W. Wang, D.-C. Zhong and T.-B. Lu, *Angew. Chem., Int. Ed.*, 2017, **56**, 738–743.
240 T. Ouyang, H.-J. Wang, H.-H. Huang, J.-W. Wang, S. Guo, W.-J. Liu, D.-C. Zhong and T.-B. Lu, *Angew. Chem., Int. Ed.*, 2018, **57**, 16480–16485.
241 U. R. Pokharel, F. R. Fronczek and A. W. Maverick, *Nat. Commun.*, 2014, **5**, 5883.
242 N. D. Loewen, E. J. Thompson, M. Kagan, C. L. Banales, T. W. Myers, J. C. Fettinger and L. A. Berben, *Chem. Sci.*, 2016, **7**, 2728–2735.
243 K. Kusuda, R. Ishihara, H. Yamaguchi and I. Izumi, *Electrochim. Acta*, 1986, **31**, 657–663.
244 M. Abdinejad, A. Seifitokaldani, C. Dao, E. H. Sargent, X.-a. Zhang and H. B. Kraatz, *ACS Appl. Energy Mater.*, 2019, **2**, 1330–1335.
245 S. Kapusta and N. Hackerman, *J. Electrochem. Soc.*, 1984, **131**, 1511–1514.
246 N. Furuya and K. Matsui, *J. Electroanal. Chem. Interfacial Electrochem.*, 1989, **271**, 181–191.
247 T. V. Magdesieva, T. Yamamoto, D. A. Tryk and A. Fujishima, *J. Electrochem. Soc.*, 2002, **149**, D89–D95.
248 V. S. Thoi, N. Kornienko, C. G. Margarit, P. Yang and C. J. Chang, *J. Am. Chem. Soc.*, 2013, **135**, 14413–14424.
249 J. D. Cope, N. P. Liyanage, P. J. Kelley, J. A. Denny, E. J. Valente, C. E. Webster, J. H. Delcamp and T. K. Hollis, *Chem. Commun.*, 2017, **53**, 9442–9445.
250 S. Gonglach, S. Paul, M. Haas, F. Pillwein, S. S. Sreejith, S. Barman, R. De, S. Müllegger, P. Gerschel, U.-P. Apfel, H. Coskun, A. Aljabour, P. Stadler, W. Schöfberger and S. Roy, *Nat. Commun.*, 2019, **10**, 3864.
251 Y. Wu, Z. Jiang, X. Lu, Y. Liang and H. Wang, *Nature*, 2019, **575**, 639–642.
252 K. Ogura and S. Yamasaki, *J. Chem. Soc., Faraday Trans. 1*, 1985, **81**, 267–271.
253 K. Ogura and K. Takamagari, *J. Chem. Soc., Dalton Trans.*, 1986, 1519–1523.
254 K. Ogura and I. Yoshida, *J. Mol. Catal.*, 1988, **47**, 51–57.
255 C. Cometto, L. Chen, D. Mendoza, B. Lassalle-Kaiser, T.-C. Lau and M. Robert, *ChemSusChem*, 2019, **12**, 4500–4505.
256 Z. Weng, J. Jiang, Y. Wu, Z. Wu, X. Guo, K. L. Materna, W. Liu, V. S. Batista, G. W. Brudvig and H. Wang, *J. Am. Chem. Soc.*, 2016, **138**, 8076–8079.
257 Z. Weng, Y. Wu, M. Wang, J. Jiang, K. Yang, S. Huo, X.-F. Wang, Q. Ma, G. W. Brudvig, V. S. Batista, Y. Liang, Z. Feng and H. Wang, *Nat. Commun.*, 2018, **9**, 415.
258 Z. Guo, S. Cheng, C. Cometto, E. Anxolabéhère-Mallart, S.-M. Ng, C.-C. Ko, G. Liu, L. Chen, M. Robert and T.-C. Lau, *J. Am. Chem. Soc.*, 2016, **138**, 9413–9416.